Meissner effect in superconducting microtraps

Dissertation

zur Erlangung des Grades eines Doktors
der Naturwissenschaften
der Fakultät für Mathematik und Physik
der Eberhard-Karls-Universität zu Tübingen
vorgelegt von

Daniel Cano

aus Palencia

2009

Tag der mündlichen Prüfung:	30. April 2009
Dekan:	Prof. Dr. Wolfgang Knapp
1. Berichterstatter:	Prof. Dr. József Fortágh
2. Berichterstatter:	Prof. Dr. Dieter Koelle
3. Berichterstatter:	Prof. Dr. Halina Rubinsztein-Dunlop

Contents

Chapter 1

Introduction

Quantum gases are excellent model systems that help physicists to gain insight into many-body quantum phenomena. The study of quantum gases has rapidly evolved in the last years thanks to the advances in the experimental techniques for trapping and manipulating ultracold atoms and molecules. Control over the internal and external states of atoms and molecules is achieved using laser light, radio-frequency radiation or static electric and magnetic fields.

Bose-Einstein condensates have been the subjects of fascinating experimental research since their first realization in 1995 [And95, Bra95, Dav95]. Some of the greatest achievements include the interference of macroscopic matter waves [And957], the creation of vortices [Mat99, Abo01] and solitons [Bur99, Den00, Kha02, Str02], the transition from superfluid to Mott insulator [Gre02] or the observation of a fermion-like, Tonks-Girardeau gas of bosons [Par04, Kin05]. Experiments with degenerate Fermi gases have also been very successful since their first realization in 1999 [DeM99]. The most important highlight of experiments with Fermi gases is the study of the BCS-BEC crossover [Bar04, Bou04, Chi04, Kin04, Reg04, Zwi04] by magnetically tuning the particle-particle interaction near Feshbach resonances [Ino98].

One area that has been particularly exciting is the storage and manipulation of atomic quantum gases by means of miniaturized elements. These elements are typically integrated on a flat solid substrate that is commonly called atom chip [Fol02, For07]. The main motivation for the development of atom chips is the high spatial resolution of the generated potentials. The potentials can be shaped with at least the same resolution as the size of the field-generating elements. The state-of-the-art fabrication technologies of metals, semiconductors, superconductors and optical waveguides allow the realization of potentials of almost arbitrary geometries. Potentials for ultracold gases have been realized using different field-generating elements, such as miniaturized current-carrying wires [For98, Gun05, For07], permanent magnets [Sab99, Hal06], charged electrodes [Den98, Kru03], arrays of microlenses [Dum02], transparent surfaces with evanescent light waves [Cor02, Ham03] or aligned mirrors for standing laser waves [Wan05].

The usage of microfabricated wires with applied electric currents is probably the most versatile method for generating potentials in atom chips. In this way, the magnetic fields can be easily ramped up and down and the potential geometry can be continuously transformed. By means of these potentials, ultracold quantum gases are routinely trapped and manipulated. Microfabricated wires with applied electric currents have been used to create a variety of potentials with different geometries, such as guides [For98, Den99, Mul99], atomic beam splitters [Cas00], dynamical double-well potentials [Shi05, Est05], periodic lattices [Drn99, Lau99, Gun07] and conveyor belts [Rei99, Han01].

A key role on atom chips is played by the atom-surface interactions, like undesirable spin-decoherence mechanisms [Jon03, Har03, Lin04] and attractive Casimir-Polder forces [Obr07, Har05]. Spin-decoherence mechanisms limit the lifetime of magnetically trapped atoms near the chip surface. One of the most adverse spin-decoherence mechanisms is the near-field noise radiation arising from thermally induced currents in the conductive surfaces of the atom chip. Cooling the atom chip can reduce those thermal currents and thus increase the lifetime. An important increase in lifetime of several orders of magnitude is expected when the conductive surfaces of the atom chip cross the transition to the superconducting state [Sch05, Ska06, Hoh07]. Increased atomic coherence times at very short distances from superconducting surfaces will permit the manipulation of atomic wave functions even on the submicron scale. Besides, it is likely that atom chips with superconducting microstructures will have important applications such as novel hybrid quantum systems combining superconductors and coherent atom clouds. They include atomic hyperfine transitions coupled to local microwave sources made of Josephson junctions, or even quantum computation with superconducting devices that are coherently coupled to polar molecules [Rab06] or Rydberg atoms [Sor04]. These exciting proposals outline new perspectives on experimental research at the interface between atomic and solid-state physics.

The main goal of this thesis is to investigate the impact of the Meissner effect on magnetic microtraps for ultracold atoms near superconducting microstructures. This task has been accomplished both theoretically and experimentally. The results of this study have been also published in References [Can08a] and [Can08b]. The Meissner effect [Lon50, Ket99] distorts the magnetic fields near superconducting surfaces, thus altering the parameters of magnetic microtraps. Understanding how the Meissner effect alters the magnetic potentials is essential for the proper evaluation of the prospects of this new field of research.

The thesis starts with the development of a novel numerical method for calculating magnetic fields in atom chips with superconducting microstructures (Chapter 2). This numerical method overcomes the geometrical limitations of other calculation techniques and can solve superconducting microstructures of arbitrary geometry. The numerical method has been used to calculate the parameters of magnetic microtraps in computer-simulated chips containing thin-film wires. Simulations were carried out for both the

superconducting and the normal-conducting state, and the differences between the two cases were analyzed. Computer simulations demonstrate that the Meissner effect shortens the distance between the magnetic microtrap and the superconducting surface, reduces the magnetic-field gradients and dramatically lowers the trap depth.

Results from computer simulations have been contrasted with experimental measurements. Experimental measurements have been carried out in a new apparatus that is thoroughly described in the third chapter of this thesis. The experimental apparatus generates a magnetic microtrap for ultracold ^{87}Rb clouds near a superconducting niobium wire of circular cross section. Its design and construction have met the challenge of integrating the techniques for producing atomic quantum gases with the techniques for cooling solid bodies to cryogenic temperatures.

The characterization of the realized microtrap and the experimental results are shown in the fourth chapter of this thesis. By monitoring the position of the atom cloud, one can observe how the Meissner effect influences the magnetic microtrap. Experimental measurements of the atomic cloud near the superconducting wire are in good agreement with analytical formulas for a perfectly diamagnetic cylinder, and follow a similar tendency as the computer simulations with superconducting thin films. Some months before the completion of this apparatus, two other research groups could experimentally demonstrate the feasibility of superconducting microtraps [Nir06, Rou08] and the trapping of atoms nearby a persistent current loop [Muk07]. However, in none of those experiments the distance between the atoms and the superconducting surface was short enough to accurately evaluate the impact of the Meissner effect. The results on the Meissner effect presented in this thesis will have important implications for experiments with quantum gases near superconducting surfaces.

Chapter 2

Computer simulations of superconducting atom chips

The design of superconducting microstructures for trapping and manipulating ultracold atoms requires numerical methods to simulate the Meissner effect. In this chapter we develop a numerical method that can be applied to superconducting microstructures of arbitrary geometries. The numerical method relies on the London theory. This chapter also shows the computer simulations of a magnetic microtrap generated by a superconducting atom chip. The impact of the Meissner effect on the magnetic microtrap is evaluated.

2.1 The London theory

The London theory [Lon50] provides a simple but useful description of the electrodynamics of superconductors. The London theory can be deduced by restricting the Maxwell equations to a perfectly conducting metal in which the moving electrons are not scattered by impurities, defects or thermal vibrations. The total energy is the sum of the magnetic energy of the electric currents and the kinetic energy associated with the mass of the moving electrons. The thermal energy, which is dominant in normal conductors with resistance, is absent from the perfectly conducting metal. The main consequence of superconductivity is that electric currents flow within a thin surface layer, the thickness of which is characterized by the London penetration depth λ_L:

$$\lambda_L = \sqrt{\frac{m_e}{n_e e^2 \mu_0}}, \tag{2.1}$$

where m_e is the mass of the electron, n_e is the density of electrons, e is the elementary electric charge and μ_0 is the magnetic constant.

The equations for the current density and the magnetic field,

$$\nabla \times (\nabla \times \boldsymbol{J}) + \frac{1}{\lambda_L^2} \boldsymbol{J} = 0, \tag{2.2}$$

$$\nabla \times (\nabla \times \boldsymbol{B}) + \frac{1}{\lambda_L^2}\boldsymbol{B} = 0, \tag{2.3}$$

lead to spatially inhomogeneous fields that decay exponentially from the surface to the interior of the superconductor. The solution of these two equations, which is unique, minimizes the free energy.

The London theory is local, that is to say, it relates the current density and the magnetic field at each point:

$$\nabla \times \boldsymbol{J} = -\frac{n_e e^2}{m_e}\boldsymbol{B}. \tag{2.4}$$

On the other hand, superconductivity is a non-local phenomenon originated by the coherent condensation of electron pairs into a macroscopic quantum state, the characteristic distance of which is the coherence length ξ. The coherence length represents a measure of the intrinsic non-local nature of the superconducting state. The local London model is accurate if the coherence length is shorter than λ_L, which is the case of Type-II superconductors[1] [Tin75]. For Type-I superconductors, in which the coherence length is longer than λ_L, the London theory is not valid, and the decay function of the fields within the superconductor is not exactly exponential. Non-local effects in Type-I superconductors strongly affect the field distributions. Nevertheless, it has been demonstrated that Equations 2.2 and 2.3 are still a good approximation for Type-I superconductors when substituting λ_L by an effective penetration depth λ_E, which is calculated as [Ket99]:

$$\lambda_E = (0.62\lambda_L^2\xi)^{1/3}. \tag{2.5}$$

In this thesis, the London theory will be used to calculate magnetic fields near superconducting thin films. The letter λ will denote the penetration depth in general, which corresponds to either λ_E or λ_L, depending on whether the superconductor is Type I or Type II.

2.2 Numerical method for calculating superconducting current densities

Current distributions in superconducting thin films are calculated in the frame of the London theory. Despite its fundamental nature, exact solutions of the London theory exist only for trivial cases such as a single sphere or a single cylinder in a homogeneous magnetic field [Lon50]. Numerical methods are therefore necessary to calculate current density distributions in thin-film microstructures. Brandt and Mikitik [Bra00] reported on how to obtain numerical solutions of the London theory for straight wires with rectangular cross

[1] Equations 2.2 and 2.3 are strictly valid only for Type-II superconductors in absence of vortices. However, by introducing some modifications in the London theory, this can also model spatial magnetic field profiles of vortex lattices in Type-II superconductors [Ket99]. Calculations presented in this chapter are carried out for the vortex-free superconducting state. A detailed description of vortex lattices would require more complex equations and is not the goal of the present thesis.

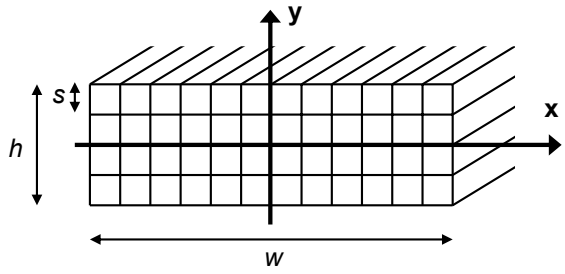

Figure 2.1: Sketch of the division used to calculate current distributions in arrays of parallel thin-film wires. A cross section of a wire is shown. Every wire is divided up into a large number of longitudinal strips with squared cross section of side s. The current density within each strip is assumed homogeneous.

section in a perpendicular homogeneous magnetic field and/or with applied electric current. More general geometries can be solved using commercial programs which, however, have severe limitations. For example, most of them provide accurate solutions only if the thickness h of the thin film is similar to the penetration depth λ [Kap06]. The numerical method presented in this thesis overcomes this limitation and provides accurate solutions of the London theory by finding the current distribution that minimizes the free energy. A similar minimization method [Par03] has been used to obtain magnetization curves of arrays of superconducting strips in homogeneous magnetic fields. The numerical method presented in this thesis can solve more general geometries in arbitrary inhomogeneous magnetic fields, including most of the geometries that are typically present in atom chips.

The numerical method for calculating current distributions in superconducting thin films will be explained through the analysis of two particular cases. The first of these describes the behavior of an array of parallel straight thin-film wires with applied electric currents. The second case describes the behavior of arbitrarily-shaped thin films in an inhomogeneous magnetic field.

2.2.1 Parallel thin-film wires with applied currents

The numerical method explained in this section can be used to calculate current distributions in arrays of parallel straight thin-film wires on a chip. In order to simplify the explanation, let us consider that the number of wires is two. The electric currents applied to the wires are denoted by I_1 and I_2, respectively.

Current distributions in the wires are calculated with an energy-minimization procedure. As explained in the previous section, finding the solution of Equation 2.2 is equivalent to minimizing the energy. For this purpose, every thin-film wire is divided up into a large number of thin longitudinal strips with squared cross section of side s (see Figure 2.1). The total number of thin strips is $N = N_1 + N_2$, where N_1 and N_2 are the numbers of thin strips contained in each wire. The current density is assumed homogeneous within each thin strip, although it may vary from strip to strip. The free energy of this system is

the sum of the magnetostatic energy of the currents and the kinetic energy of the electrons [Ket99], and can be written in the form

$$F(I_1, I_2, ..., I_N) = \frac{1}{2}\sum_{n=1}^{N}\sum_{m=1}^{N} I_n M_{nm} I_m, \tag{2.6}$$

where I_n is the electric current along the strip n, and M_{nm} is the mutual inductance between the strips n and m. The matrix elements M_{nm} are calculated from [Gro46, Mer69],

$$\begin{aligned} M_{nm} &= \frac{\mu_0}{4\pi}\int_n \mathtt{d}^3\boldsymbol{r}_n \int_m \mathtt{d}^3\boldsymbol{r}_m \frac{J_n}{I_n}\frac{J_m}{I_m}\frac{1}{|\boldsymbol{r}_n - \boldsymbol{r}_m|} + \\ &+ \delta_{nm}\mu_0\lambda^2 \int_n \mathtt{d}^3\boldsymbol{r}_n \frac{J_n^2}{I_n^2}\,, \end{aligned} \tag{2.7}$$

where δ_{nm} is the Kronecker delta, J_n is the current density, and $\boldsymbol{r}_n$ denotes the position of point within the strip n. The first and second terms represent the magnetic and the kinetic inductances, respectively. Since the current is assumed to be homogeneously distributed within each strip, the current density is $J_n = I_n/s^2$. Then, the magnetic term can be approximated by classical formulas tabulated in Reference [Gro46], and the integral of the kinetic term has a trivial solution. The matrix elements become

$$M_{nm} \simeq \begin{cases} \frac{\mu_0}{2\pi} l\left(\ln\frac{2l}{d} - 1\right) & \texttt{if } n \neq m\,, \\ \\ \frac{\mu_0}{2\pi} l\left(\ln\frac{l}{s} + \frac{1}{2}\right) + \mu_0\frac{\lambda^2 l}{s^2} & \texttt{if } n = m\,, \end{cases} \tag{2.8}$$

where l is the length of the wires and d is the distance between the centers of the considered strips.

The superconducting current density is obtained by finding the set of values $\{I_n\}_{n=1,...,N}$ that minimize the function $F(I_1, ..., I_N)$. This is accomplished with the method of the Lagrangian multipliers, and imposing that the total current flowing in each wire is fixed. The constraints are represented by the functions $\varphi_1(I_1, ..., I_N)$ and $\varphi_2(I_1, ..., I_N)$, which are defined by

$$\varphi_1(I_1, ..., I_N) = \sum_{n=1}^{N_1} I_n - I_1 = 0\,; \qquad \varphi_2(I_1, ..., I_N) = \sum_{n=N_1+1}^{N} I_n - I_2 = 0. \tag{2.9}$$

The current density that minimizes the free energy $F(I_1, ..., I_N)$ is obtained from the following equations [Arf95]:

$$\frac{\partial F(I_1, ..., I_N)}{\partial I_m} + \Lambda_1\frac{\partial\varphi_1(I_1, ..., I_N)}{\partial I_m} + \Lambda_2\frac{\partial\varphi_2(I_1, ..., I_N)}{\partial I_m} = 0\,, \qquad m = 1, \ldots, N\,, \tag{2.10}$$

where Λ_1 and Λ_2 are the Lagrangian multipliers. Thus

$$\begin{aligned} &\sum_{n=1}^{N} M_{nm} I_n + \Lambda_1 = 0\,, \qquad m = 1, \ldots, N_1\,, \\ &\sum_{n=1}^{N} M_{nm} I_n + \Lambda_2 = 0\,, \qquad m = N_1 + 1, \ldots, N\,. \end{aligned} \tag{2.11}$$

The solution of this system of linear equations is a set of values $\{I_n\}_{n=1,\dots,N}$ that represent the current distribution in the superconducting wires.

For long wires ($l > 10w$) the calculated current distribution does not depend on l. This limit is valid in all the examples shown in this thesis, where all wires are assumed infinitely long. Low values of s improve the accuracy of the solution at the expense of long computation time. All values lower than $\lambda/2$ produce practically the same numerical results, and therefore, $s = \lambda/2$ is in general a good choice for calculations.

Calculating the mutual inductance M_{nm} between two strips is not incompatible with the general definition of mutual inductance for two closed circuits. One can imagine that every wire is part of a closed circuit that includes the current drivers and the wires between the chip and the drivers. The mutual inductance between two strips can be defined as the contribution of the two strips to the total mutual inductance between the closed circuits of which they form part.

After obtaining the current distribution $\{I_n\}_{n=1,\dots,N}$, the total mutual inductance between the two wires can be easily calculated as

$$M_{wires} = \frac{1}{I_1 I_2} \sum_{n=1}^{N_1} \sum_{m=N_1+1}^{N} I_n M_{nm} I_m. \tag{2.12}$$

And the self-inductances are

$$L_{wire\ 1} = \frac{1}{I_1^2} \sum_{n=1}^{N_1} \sum_{m=1}^{N_1} I_n M_{nm} I_m\,, \qquad L_{wire\ 2} = \frac{1}{I_2^2} \sum_{n=N_1+1}^{N} \sum_{m=N_1+1}^{N} I_n M_{nm} I_m. \tag{2.13}$$

2.2.2 Thin films in inhomogeneous magnetic field

Screening currents arise in superconductors in the presence of external magnetic fields as a consequence of the Meissner effect. Screening currents can be calculated using the method described in this section. This numerical method requires to decompose the screening currents in small current elements $\{I_n\}_{n=1,\dots,N}$. In a magnetostatic situation, the screening currents are closed, and therefore, a decomposition based on small magnetic dipoles or small closed current elements is the most convenient.

The geometry of the closed current elements I_n described in this paragraph is suitable to evaluate the energy and the flux including the kinetic term[2]. The superconducting thin-film wire is divided up into small cubes of side s. The current is assumed to be homogeneous within every small cube, although both the intensity and the direction of the current might vary from cube to cube. Closed current elements I_n similar to magnetic dipoles are built by grouping the cubes in sets of four, in the way illustrated in Figure

[2]The energy and flux can be properly evaluated from the closed current elements $\{I_n\}_{n=1,\dots,N}$ when these occupy the whole volume of the superconducting body and when the overlapping between neighbor current elements is total, in the sense that a homogeneous distribution of closed current elements generate null electric current at any internal point that is not on the surface of the superconducting body.

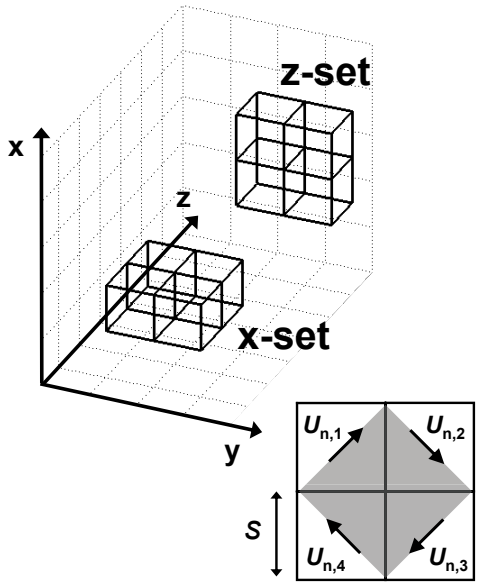

Figure 2.2: Sketch of the sets of cubes in which superconducting thin films are divided to calculate the screening currents. The lower part illustrates how the current I_n is distributed within the set n. The direction of the current, which is different in every cube, is represented by four unit vectors $\boldsymbol{U}_{n,1}$, $\boldsymbol{U}_{n,2}$ $\boldsymbol{U}_{n,3}$ and $\boldsymbol{U}_{n,4}$. The effective surface of the set is symbolized by a gray square of side $\sqrt{2}s$.

2.2. The centers of the four cubes lie in the same plane. Sets of four cubes can be built in planes parallel to the x axis (x-sets), to the y axis (y-sets) or to the z axis (z-sets). In this manner, any cube that is not on the wire surface belongs to twelve different sets: four x-sets, four y-sets and four z-sets. Sets are sorted with numbers. Every set has associated a current I_n, n being the number of the set. The current element I_n is distributed within the set n in a way that is similar to a magnetic dipole, as shown in Figure 2.2. The current I_n changes its direction by 90 degrees as it passes from a cube to the next cube of the set. The direction of I_n in each cube is described by the unit vectors $\boldsymbol{U}_{n,1}$, $\boldsymbol{U}_{n,2}$, $\boldsymbol{U}_{n,3}$ and $\boldsymbol{U}_{n,4}$.

The mutual inductance M_{nm} between two sets n and m is obtained by summing the contributions of the mutual inductances between the separate cubes of both sets. Assuming one set n made up of the cubes n_1, n_2, n_3 and n_4 and another set m made up of the cubes m_1, m_2, m_3 and m_4, the total mutual inductance between the two sets is

$$M_{nm} = \sum_{a=1}^{4}\sum_{b=1}^{4} \hat{M}_{n_a m_b} \left(\boldsymbol{U}_{n,a} \cdot \boldsymbol{U}_{m,b}\right), \tag{2.14}$$

where

$$\begin{aligned} \hat{M}_{n_a m_b} &= \frac{\mu_0}{4\pi} \int_{n_a} \mathtt{d}^3\boldsymbol{r}_{n,a} \int_{m_b} \mathtt{d}^3\boldsymbol{r}_{m,b} \frac{J_n}{I_n}\frac{J_m}{I_m}\frac{1}{|\boldsymbol{r}_{n,a}-\boldsymbol{r}_{m,b}|} + \\ &+ \delta_{n_a m_b}\,\mu_0\lambda^2 \int_{n_a} \mathtt{d}^3\boldsymbol{r}_{n,a}\frac{J_n^2}{I_n^2} \end{aligned} \tag{2.15}$$

is the contribution of the cubes n_a and m_b to M_{nm}. The scalar product $\boldsymbol{U}_{n,a}\cdot\boldsymbol{U}_{m,b}$ accounts for the fact that this contribution depends on the angle between the current directions. Here, $\boldsymbol{r}_{n,a}$ denotes the position of point within the cube n_a, and J_n is the current density in the set n. The integrals are carried out over the volumes of the corresponding cubes. Since the current is homogeneously distributed within every cube, the current density of a set can be expressed as $J_n = I_n/s^2$. Then, the integral of the kinetic term has a trivial solution. The double integral of the magnetic term was calculated numerically[3]. The matrix elements become

$$\hat{M}_{n_a m_b} \simeq \begin{cases} \frac{\mu_0}{4\pi} 1.88 s + \frac{\mu_0 \lambda^2}{s}\,, & d = 0\,, \\ \frac{\mu_0}{4\pi} 0.98 s\,, & d = s\,, \\ \frac{\mu_0}{4\pi}\frac{s^2}{d}\,, & d > s\,, \end{cases} \tag{2.16}$$

where d is the distance between cube centers.

For the reasons mentioned above, the mutual inductance between two cubes is a senseless physical idea unless each cube is regarded as part of a close circuit. To understand the meaning of $\hat{M}_{nm}$, the screening current tubes can be regarded as a collection of closed circuits with a certain inductance matrix. In this way the mutual inductance between two cubes can be understood as the contribution made by the cubes to the total mutual inductance between the two current tubes in which the cubes are included. This idea also applies to the self-inductance.

Every set of cubes is also characterized by the effective surface $\boldsymbol{S}_n$, which is represented in Figure 2.2 by the gray area. The effective surface is defined so that the product $M_{nm}I_m$ is the flux produced by I_m through $\boldsymbol{S}_n$. The modulus of $\boldsymbol{S}_n$ is $2s^2$, and its direction is determined by the right-hand rule from the direction of the current I_n. Following the notation of Figure 2.2, the effective surface can be expressed by $\boldsymbol{S}_n = 2s^2\boldsymbol{U}_{n,1}\times\boldsymbol{U}_{n,2}$.

The solution of the London theory for this system is the current distribution that cancels the flux -including both the magnetic and the kinetic terms- in the interior of the superconducting wires. It is possible to demonstrate [Lon50] that this condition is equivalent to the free-energy minimization performed in the previous section. The equations to be solved are formulated so that the flux through every set of cubes is null:

$$\sum_{m=1}^{N} M_{nm} I_m + \boldsymbol{S}_n \cdot \boldsymbol{B}_n = 0\,, \qquad n = 1, \ldots, N\,. \tag{2.17}$$

Here, N is the total number of sets, M_{nm} symbolizes the elements of the inductance matrix, $\boldsymbol{B}_n$ is the external magnetic field at the position of the set n, and $\boldsymbol{S}_n$ is the effective surface of the set n. The first term in this equation represents the total flux $\Phi_{S,n}$ induced by the screening currents onto the set n. The second term is the magnetic flux $\Phi_{0,n}$ of the inhomogeneous external field onto the set n.

[3]It has been numerically solved in *Mathematica* using the function *NIntegrate*

In typical cases, the matrix M_{nm} would have a large size, and therefore it could not be inverted using any of the mathematic programmes that are generally available. As an alternative, an iterative method can be used to solve Eq. (2.17). In the fist step, a homogeneous screening current distribution is assumed: $I_m^{(1)} = -\boldsymbol{S}_m \cdot \boldsymbol{B}_m / M_{mm}$; $m = 1, \ldots, N$. This distribution will not satisfy Eq. (2.17), and the flux $\Phi_{S,n}^{(1)} = \sum_{m=1}^{N} M_{nm} I_m^{(1)}$ created by the assumed screening currents onto each set n will not cancel the flux of the inhomogeneous external field, $\Phi_{0,n}$. In the second step, the current distribution is calculated by $I_n^{(2)} = I_n^{(1)} - \xi_n^{(1)}(\Phi_{0,n} + \Phi_{S,n}^{(1)})/M_{nn}$, which will generate a flux that will be more similar to the desired solution. The process continues until the convergence condition is satisfied: $|\Phi_{0,n} + \Phi_{S,n}^{(e)}| < 10^{-4}\Phi_{0,n}$, after e iterations. The number ξ is a convergence factor that has no physical meaning. Its value is chosen by trial and error. The best choice depends on the geometry of the superconducting body. If ξ is too high, the method is not convergent; but if ξ is too low, the convergence is very slow. ξ can vary from set to set and also from step to step. The particular values of ξ used for our calculations will not be shown here since the results do not depend on them and since there are many other possibilities.

Once the closed current elements $\{I_n\}_{n=1,\ldots,N}$ have been obtained, the total current in every single cube is calculated by summing the contributions of the sets of which the cube forms part. From the total currents in the single cubes, the magnetic field outside the superconducting body can be calculated. The method presented in this section can be used to calculate screening currents in superconducting thin-films induced by arbitrary inhomogeneous magnetic fields.

2.3 The principle of magnetic trapping

Neutral atoms can be trapped and manipulated by means of their interaction with magnetic fields [For07]. The magnetic potential is calculated as

$$V_{mag}(\boldsymbol{r}) = -g_F \mu_B m_F B(\boldsymbol{r}), \tag{2.18}$$

where g_F is the Landé factor of the atomic hyperfine state, μ_B is the Bohr magneton, m_F is the magnetic quantum number, and $B(\boldsymbol{r})$ is the modulus of the magnetic field. If the magnetic moment of the atom points in the direction opposite to the magnetic field ($V_{mag}(\boldsymbol{r}) < 0$), the atom is repelled from regions with high magnetic field, and a minimum of $B(\boldsymbol{r})$ corresponds to a potential minimum. Then, the atom is said to be in a low-field-seeking state. Conversely, if the magnetic moment points in the same direction as the magnetic field ($V_{mag}(\boldsymbol{r}) > 0$), the atom is in a strong-field-seeking state. Since maxima of the magnetic-field modulus are forbidden[4], purely magnetic traps can only be realized if the atoms are in low-field-seeking states.

[4]This is a direct consequence of $\boldsymbol{\nabla} \cdot \boldsymbol{B} = \boldsymbol{0}$

The conservative potential of Equation 2.18 describes the atom dynamics only if the adiabatic approximation can be applied. The adiabatic approximation assumes that the Larmor precession, $\omega_L = \mu_B B/\hbar$, is much faster than the apparent change of direction of the magnetic field in the rest frame of the moving atom. Then, the magnetic moment follows the direction of the field adiabatically and m_F is a constant of motion.

2.4 Magnetic guide in a superconducting chip

A quadrupole magnetic guide can be realized with the chip geometry represented in Figures 2.3 and 2.4. Three parallel thin-film wires on the chip surface generate a two-dimensional confining field $\boldsymbol{B}_{2D}$ (magnetic guide). The currents applied to the wires are denoted by I_1, I_2 and I_3. The current I_2 in the central wire is opposite in direction to the currents I_1 and I_3 in the two outer wires. The magnetic guide forms at the position (x_0, y_0), where the magnetic field of the central current I_2 is canceled by the bias field generated by I_1 and I_3. The field $\boldsymbol{B}_{2D}$ forms a two-dimensional quadrupole field around (x_0, y_0). Its modulus increases linearly in the radial directions:

$$|\boldsymbol{B}_{2D}| = a\sqrt{(x - x_0)^2 + (y - y_0)^2}. \tag{2.19}$$

Here, a is the gradient of the magnetic guide in the radial directions. If the magnetic trap is in the plane $x = 0$, and thus $I_1 = I_3$, the quadrupole field can be expressed as

$$\boldsymbol{B}_{2D} = \begin{pmatrix} a(y - y_0) \\ a(x - x_0) \\ 0 \end{pmatrix} . \tag{2.20}$$

In the following, the impact of the Meissner effect on the guide parameters is evaluated. To accomplish this task, magnetic fields and guide parameters are computed for both the superconducting and the normal-conducting state, and the differences between them are analyzed. The symbols describing the guide parameters will have an additional subindex, SC or NC, when they are referred to the superconducting or the normal-conducting state, respectively. For simplicity, the three wires are assumed to be identical in size. The width of the wires and the separation between them are $w = 5$ μm and $v = 5$ μm, respectively. The penetration depth λ in the superconducting wires is 100 nm, which is a typical value for metallic superconductors. The thickness h of the thin-film wires will be varied in the examples shown in this section in order to assess its effect on the guide parameters.

The first guide parameter to be analyzed is the position (x_0, y_0). The magnetic guide can be positioned within a large area above the chip surface by changing the ratios

$$\alpha = \frac{I_2}{I_1 + I_3} , \qquad \beta = \frac{I_1}{I_3} . \tag{2.21}$$

Figure 2.5 illustrates the trajectories corresponding to constant α (dashed lines) and to constant β (solid lines) for the superconducting and the normal conducting chip. Differ-

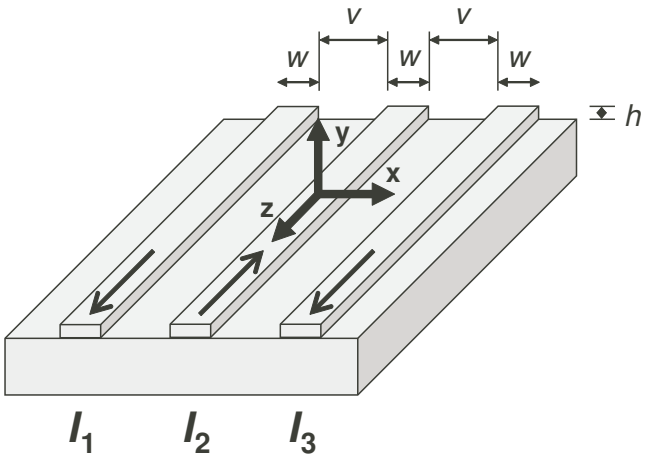

Figure 2.3: Representation of a typical atom-chip geometry that provides two-dimensional magnetic confinement [Gun05]. This theoretical example is used in this thesis to study the properties of magnetic guides near superconducting thin films. Three parallel wires on the chip surface generate a two-dimensional quadrupole field $\boldsymbol{B}_{2D}$ that provides radial confinement. The width of the thin-film wires and the separation between them are denoted by w and v, respectively.

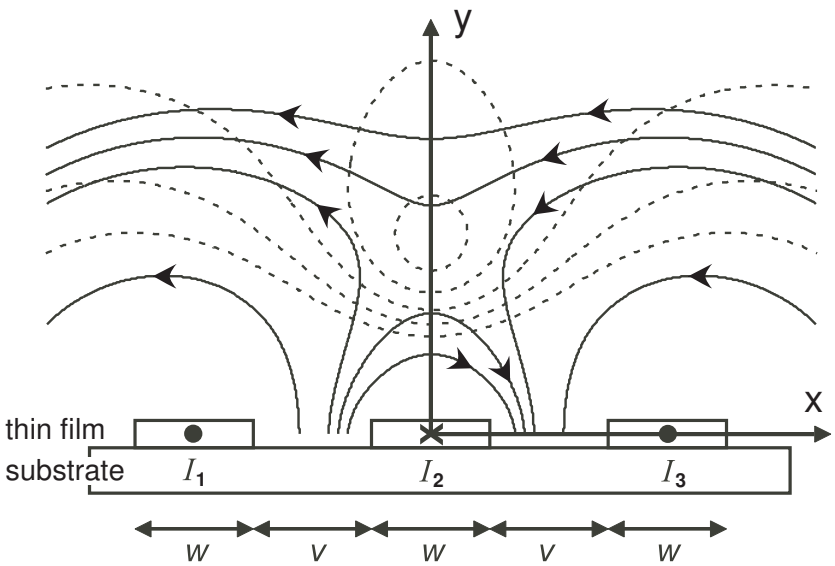

Figure 2.4: Cross section of the atom chip represented in Figure 2.3. The current I_2 in the central wire is opposite in direction to the currents I_1 and I_3 in the two outer wires. The magnetic guide forms at the positions where the magnetic field of the central current I_2 is canceled by the bias field generated by I_1 and I_3. Lines with arrows represent the magnetic-field lines. Dashed lines represent the isopotential curves.

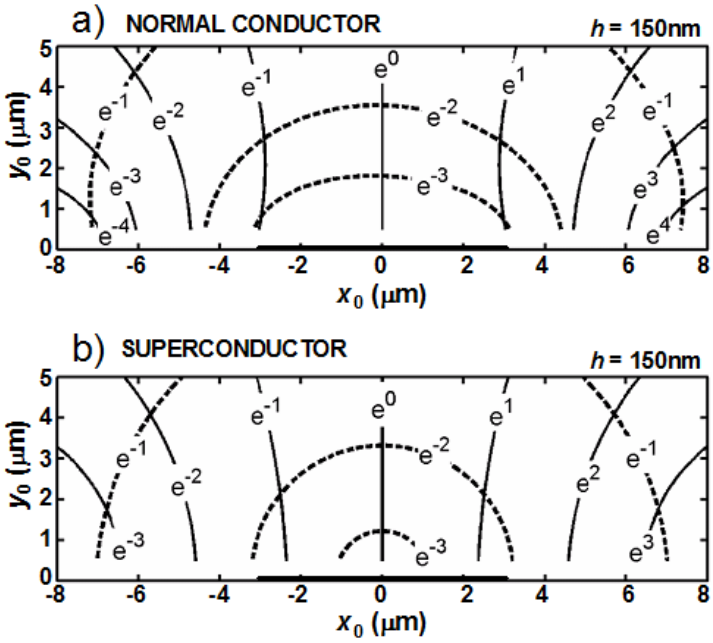

Figure 2.5: Position (x_0, y_0) of the magnetic guide in the x, y-plane as a function of the ratios α and β for the superconducting and the normal conducting chip. Solid lines are trajectories generated by varying α while keeping β constant. Dashed lines are trajectories generated by varying β while keeping α constant. The values of α and β are written on the corresponding trajectory. The width and the thickness of the thin-film wires, and the separation between them are $w = 5$ μm, $h = 150$ nm and $v = 5$ μm, respectively. The penetration depth is 100 nm in the superconducting wires.

ences between the two cases are noticeable when the distance between the magnetic trap and the chip surface is smaller than the width of the wires.

In principle, both the position and the radial gradient of the magnetic guide depend on the applied currents I_1, I_2 and I_3. Once the ratios α and β have been chosen to position the magnetic guide, the radial gradient can be varied by changing the value of $I_S = I_1 + I_2 + I_3$. Figure 2.6(a) shows for constant $I_S = 1$ A the radial gradient a_{NC} in the normal conducting chip as a function of the position of the magnetic guide. The radial gradient for other values of I_S can be obtained by linear scaling. For the superconducting case, the gradient a_{SC} was calculated in the same way, keeping I_S at a constant value of 1 A. Figure 2.6(b) shows the ratio a_{SC}/a_{NC}. Superconducting wires produce considerably lower radial gradients than normal conducting wires.

Changes in the trapping field caused by the Meissner effect become more pronounced when the superconducting wires are thicker or when the penetration depth is smaller. Either thinner wires or longer penetration depths imply more homogeneity in the superconducting current densities, which results in magnetic fields which are more similar to those produced by normal conductors. Figure 2.7 shows the current-density distribution

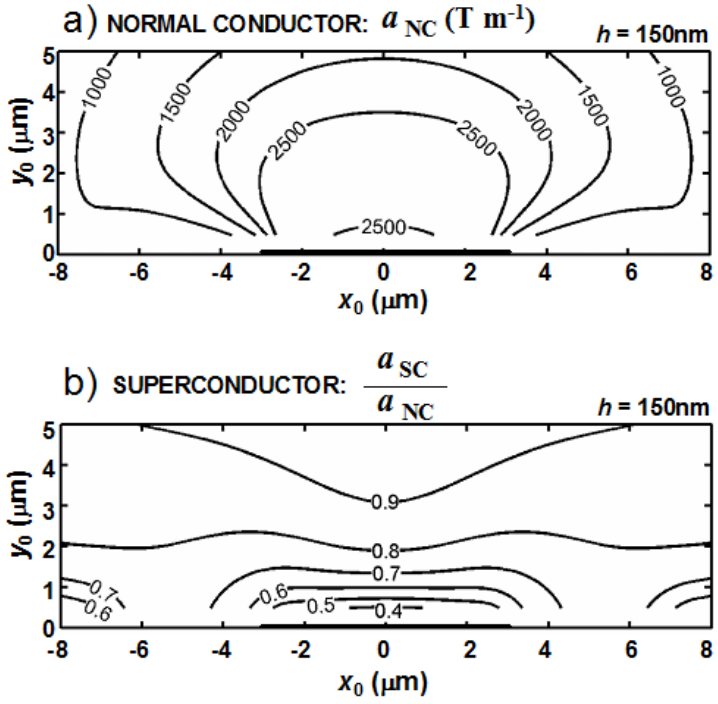

Figure 2.6: Radial gradient obtained for different positions of the magnetic guide (x_0, y_0) keeping the sum of the currents $I_S = I_1 + I_2 + I_3$ at a constant value of 1 A. a) Radial gradient a_{NC} in the normal conducting chip. b) Ratios of the gradient a_{SC} in the superconducting chip to the gradient a_{NC} in the normal conducting chip. The width and the thickness of the thin-film wires, and the separation between them are $w = 5$ μm, $h = 150$ nm and $v = 5$ μm, respectively. The penetration depth is 100 nm in the superconducting wires.

$J_2(x, y)$ along the central wire for two different thicknesses. Three regimes can be distinguished. If $h \gg \lambda$, the current density decays exponentially from the surface and shows a sharp peak in each corner. If $h \sim \lambda$, the current density becomes homogeneous along the y-axis, having two maxima at $x = w/2$ and $x = -w/2$. For extremely thin wires, the kinetic energy gets so high that the current density becomes almost homogeneous, allowing the magnetic flux to penetrate the film.

In the case of normal conducting wires, the magnetic-trap parameters were independent of the thickness h. This is illustrated by comparing the numerical results obtained for different values of h. The variations in the x, y-position and in the radial gradient produced by varying h between 50 μm and 800 μm were respectively less than 0.01 μm and less than 0.1% at any position within the area represented in Figures 2.5 and 2.6. On the contrary, our numerical calculations demonstrate that the magnetic-trap parameters depend considerably upon the value of the thickness h when the chip is superconducting. For example, while for $h = 150$ nm the radial gradient in the superconducting chip is 0.4 times the radial gradient in the normal conducting chip at 0.5 μm from the chip surface above the central wire (see Figure 2.6), this reduction factor is 0.6 for $h = 50$ nm and

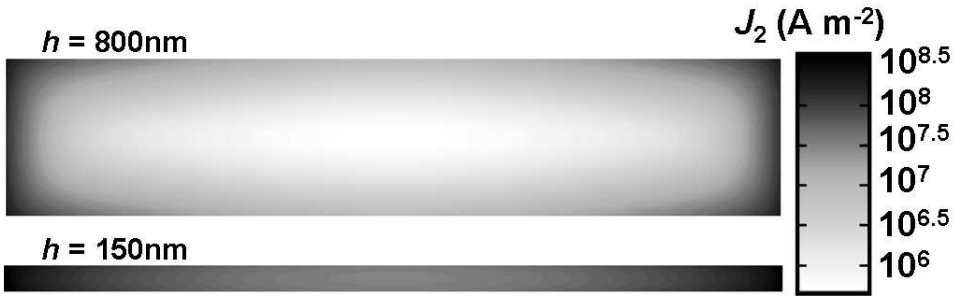

Figure 2.7: Current density J_2 in the central wire for two different values of the thickness h. The cross section of the wire is shown. The width of the wires and the separation between them are $w = 5$ μm and $v = 5$ μm, respectively. $\lambda = 100$ nm. The applied currents are $I_2 = 65$ μA, and $I_1 = I_3 = 467$ μA ($\alpha = 0.07$; $\beta = 1$).

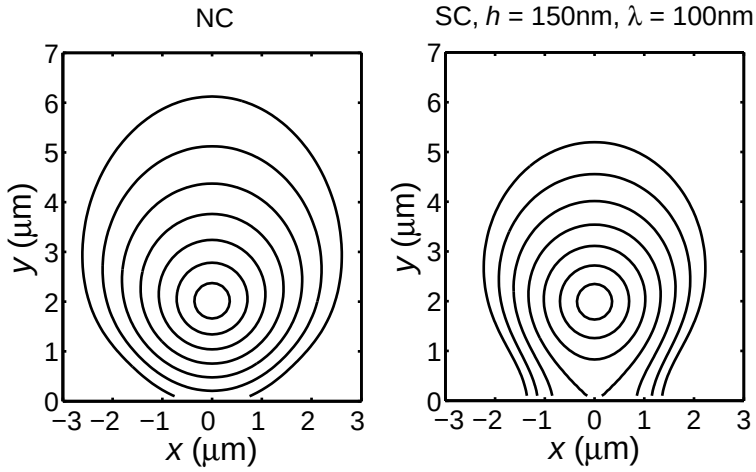

Figure 2.8: Contour maps of the magnetic-field modulus $|\boldsymbol{B}_{2D}|$ calculated for the superconducting and the normal-conducting chips. In each of them, the ratios α and β have been selected to position the magnetic guide at ($x_0 = 0$, $y_0 = 2$ μm) (In the superconducting chip, $\alpha = 0.070$ and $\beta = 1$. In the normal-conducting chip, $\alpha = 0.057$ and $\beta = 1$). I_S has been chosen so that the gradient a is the same in both cases (In the superconducting chip, I_S is 1.23 times higher than in the normal chip). In both cases the width of the wires and the separation between them are $w = 5$ μm and $v = 5$ μm, respectively. The penetration depth in the superconducting case is 100 nm. The contours are spaced by 10^{-3} times the value that I_S takes in the normal conducting chip, being the field and the current expressed in tesla and in ampere, respectively.

0.3 for $h = 500$ nm at the same position. Therefore, the thickness of the thin-film wires becomes relevant in the superconducting state.

The Meissner effect also reduces the depth of the magnetic guide. Figure 2.8 shows the equipotential contours for a superconducting and normal-conducting chip. In each of them, the ratios α and β have been properly selected to position the magnetic guide at ($x_0 = 0$, $y_0 = 2$ μm), and the total current I_T have chosen so that the gradient is the same in both cases. Even if I_S in the superconducting chip is higher, the depth of the guide is reduced by around 50% towards the superconductor.

2.5 Homogeneous offset field to reduce Majorana losses

A major drawback of the magnetic guide described in the previous section is the high rate of Majorana losses [Suk97]. Majorana losses are caused by transitions from trapped to untrapped atomic states near the center of the magnetic guide, where m_F is not conserved because the magnetic field vanishes. This can be prevented by externally applying a homogeneous offset field $\boldsymbol{B}_{0,ext} = (0, 0, b_{0,ext})$ along the longitudinal direction. The homogeneous offset field is not distorted by the Meissner effect because the longitudinal demagnetizing factor of a straight wire quickly tends to zero as its length increases to infinity [Jos65].

The offset field $\boldsymbol{B}_{0,ext}$ changes the radial potential from linear to parabolic. The modulus of the magnetic field around the trap center becomes

$$\begin{aligned} |\boldsymbol{B}_{2D}| &\simeq \sqrt{a^2\left[(x-x_0)^2+(y-y_0)^2\right]+b_{0,ext}^2} = b_{0,ext}\sqrt{1+\left(\frac{a}{b_{0,ext}}\right)^2\left[(x-x_0)^2+(y-y_0)^2\right]} \\ &\simeq b_{0,ext}+\frac{a^2}{2b_{0,ext}}\left[(x-x_0)^2+(y-y_0)^2\right]. \end{aligned} \tag{2.22}$$

As opposed to what happens with quadrupole potentials, the position of the harmonic guide is shifted by gravity. If gravity is in any of the radial directions of the magnetic guide, the shift in position can be calculated as [For07]

$$\Delta = \frac{g\ m\ b_{0,ext}}{g_F\ \mu_B\ m_F\ a^2}, \tag{2.23}$$

where g is the gravity acceleration, m is the atom mass, g_F is the Landé factor of the atomic hyperfine state, μ_B is the Bohr magneton and m_F is the magnetic quantum number.

2.6 Longitudinal confinement in a superconducting chip

Longitudinal confinement is achieved by means of the inhomogeneous offset field $\boldsymbol{B}_0$ generated by two straight offset wires located underneath the chip surface, as shown in Figure 2.9. The offset wires are driven with identical currents I_0. They are perpendicular to the

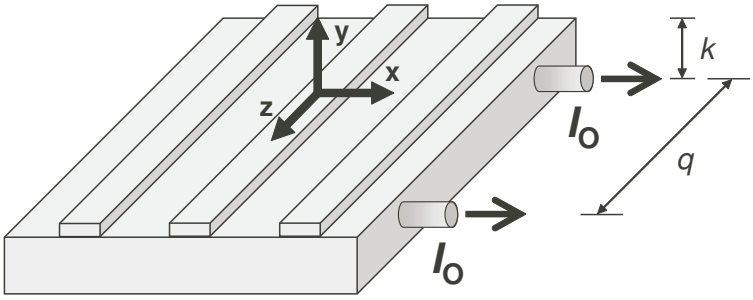

Figure 2.9: Representation of a typical atom-chip geometry that provides three-dimensional magnetic confinement. This theoretical example can be used to study the properties of magnetic micro traps near superconducting thin films. Three thin-film wires on the chip surface provide radial confinement. Underneath the chip surface there are two offset wires in the perpendicular direction to supply longitudinal confinement. The offset wires are located at $z = q/2$ and $z = -q/2$.

thin-film wires generating the magnetic guide. The distance between the offset wires and the chip surface is $k = 5$ μm. For simplicity, the offset wires are assumed to be infinitely thin. This approximation is valid if the width of the offset wires is much smaller than k, in which case neither the screening currents in the thin-film wires nor the magnetic fields near the chip surface depends on the current distribution in the offset wires. The analysis presented in this section is restricted to magnetic traps located in the plane $x = 0$. The penetration depth λ in the superconducting wires is 100 nm for all the examples shown in this section. Both the thickness h of the thin-film wires and the distance q between the two offset wires will be varied in the examples in order to assess their effect on the microtrap parameters.

The offset field $\boldsymbol{B}_0$ is superimposed onto the two-dimensional confining field $\boldsymbol{B}_{2D}$, in such a way that a magnetic trap forms between the two offset wires around the point $(x_0, y_0, 0)$. Near the center of the trap,

$$\boldsymbol{B}_0 \simeq \begin{pmatrix} 0 \\ a_0 z \\ b_0 + a_0(y - y_0) + \frac{1}{2} b_z z^2 \end{pmatrix}, \tag{2.24}$$

where a_0 and b_z are the fist- and second partial derivatives of $\boldsymbol{B}_0$ with respect to the corresponding directions, evaluated at $(x_0, y_0, 0)$. The trap forms only if $b_z > 0$; thus for distances $y_0 + k$ smaller than about 0.6 q. The y-component of $\boldsymbol{B}_0$ causes a small rotation of the longitudinal axis of the magnetic guide. This rotation occurs about the y-axis [Gun05], with angle $\psi = a/a_0$.

The magnetic trap is characterized by the radial and longitudinal oscillation frequencies

$$\omega_r = \sqrt{\frac{g_F \mu_B m_F}{m(b_0 + b_{0,ext})}} a\,, \qquad \omega_l = \sqrt{\frac{g_F \mu_B m_F}{m} b_z}\,. \tag{2.25}$$

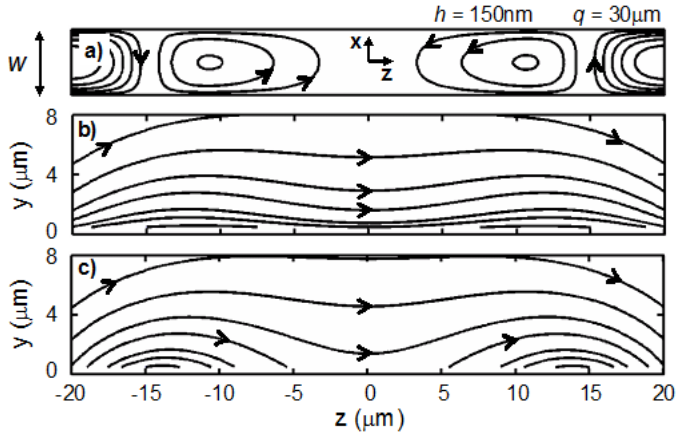

Figure 2.10: Results obtained for the magnetic field $\boldsymbol{B}_0$ when the offset wires are driven with equal currents $I_0 = 1$ mA and no current is applied to the thin-film wires. a) stream lines of the induced screening currents integrated along the y-direction in the central wire. The plotted current density is 20 μA/line. b) Field lines in the plane $x = 0$ above the superconducting chip. c) Field lines in the plane $x = 0$ above the normal conducting chip. The field lines indicate the direction of the field but the density of lines does not show the intensity of the field. One can appreciate the expulsion of the magnetic field from the interior of the superconducting wires. Calculations are performed for the following geometrical parameters: $w = 5$ μm, $v = 5$ μm, $h = 150$ nm, $k = 5$ μm and $q = 30$ μm. The penetration depth in the superconducting wires is 100 nm.

The center of the trap

$$\left(x_0, y_0 - \frac{a_0(b_0 + b_{0,ext})}{a_0^2 + a^2}, 0\right) \tag{2.26}$$

is slightly displaced from the position $(x_0, y_0, 0)$ of the magnetic guide.

Figure 2.10 shows the screening currents in the central thin-film wire as well as the magnetic-field lines of the offset field $\boldsymbol{B}_0$ for the superconducting and the normal conducting chip. Figure 2.11 represents the longitudinal component of the magnetic field calculated along the z-direction at $(x_0, y_0) = (0, 2\ \mu\text{m})$ for three different cases: normal conductor, superconductor with $h = 150$ nm, and superconductor with $h = 350$ nm. As with the results obtained for $\boldsymbol{B}_{2D}$, differences between the superconducting and the normal-conducting states become larger with increasing h. The screening currents in the superconducting quadrupole wires reduce the z-component of the magnetic field $\boldsymbol{B}_0$ at the positions $z = -q/2$ and $z = q/2$. This effect entails a decrease of the trap depth along the longitudinal direction. This reduction is of about 15% at 2 μm from the surface, and becomes higher than 25% at distances of 1 μm or shorter. Further than 10 μm, the reduction is lower than 5%.

The parameters b_0, a_0 and b_z that describe the inhomogeneous offset field $\boldsymbol{B}_0$ were numerically calculated for the superconducting chip (SC) and the normal conducting chip (NC) as a function of q and y_0. Figure 2.12(a) shows the ratio $b_{0,SC}/b_{0,NC}$. The horizontal

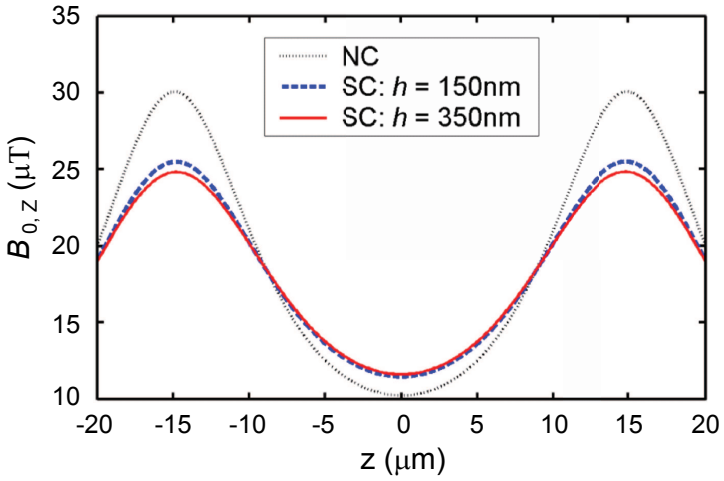

Figure 2.11: Longitudinal component of the magnetic field along the z-direction at $(x_0, y_0) = (0, 2\ \mu\text{m})$. Three different cases are represented: normal conductor, superconductor with $h = 150$ nm, and superconductor with $h = 350$ nm. $I_0 = 1$ mA. $\lambda = 100$ nm. The other geometrical parameters are the same as in Figure 2.10.

axis represents the distance q between the two offset wires, and the vertical axis represents the position of the magnetic trap y_0. As observed in this figure, the Meissner effect in the superconducting wires increases slightly the value of b_0. This increase becomes more significant as the distance between the two offset wires q gets longer, and the magnetic trap gets closer to the surface. Figure 2.12(b) shows the ratio $b_{z,SC}/b_{z,NC}$. The longitudinal oscillation frequency of the micro trap is related to b_z by means of Equation 2.25. The longitudinal frequency is dramatically reduced by the Meissner effect when the offset wires are close to each other. For high values of q the effect is the opposite, and the longitudinal frequencies are slightly higher in the superconducting chip.

Figure 2.13 compares the value of a_0 between the superconducting and the normal conducting chips. The parameter a_0 is related with the angle of rotation ψ of the microtrap as explained above. The calculated values of a_0 are significantly lower in the superconducting microstructure than in the normal conducting microstructure.

2.7 Magnetic microtrap on a superconducting atom chip

Here we apply the numerical results presented in the last two sections to a typical example of a magnetic micro trap. Figure 2.14 shows the isopotential curves of a magnetic trap generated by the atom chip depicted in Figure 2.9 in the superconducting and in the normal conducting state. The applied currents are the same in both cases. The relevant trap parameters are summarized in Table 2.1. The micro trap forms closer to the surface in the superconducting chip than in the normal conducting chip. In the present example, the Meissner effect produces an important reduction in the radial oscillation frequencies

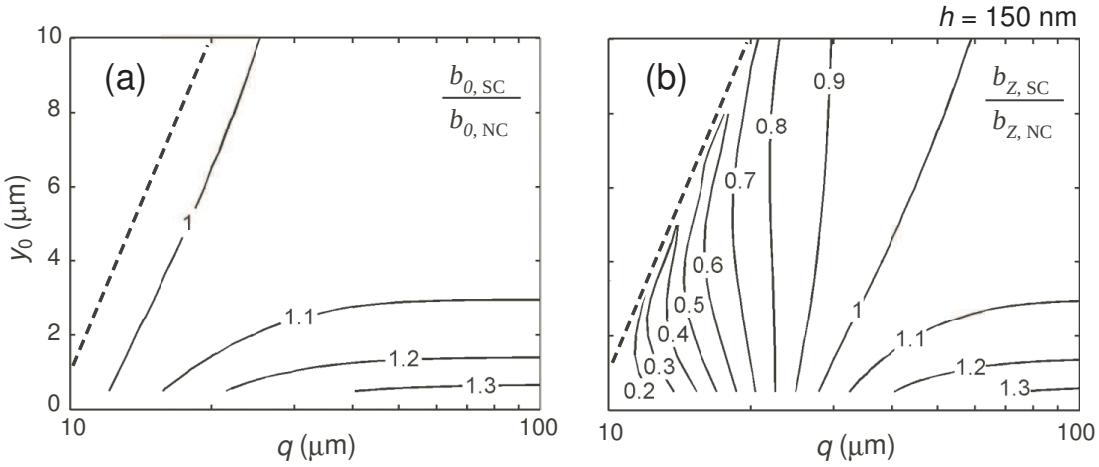

Figure 2.12: This figure compares the trap parameters b_0 and b_z between the superconducting and the normal conducting chip. a) Ratio $b_{0,SC}/b_{0,NC}$. b) Ratio $b_{z,SC}/b_{z,NC}$. The horizontal axis, in logarithmic scale, represents the distance q between the two offset wires, and the vertical axis, in linear scale, represents the position of the magnetic trap y_0. Data are represented in the plane $x = 0$. $\lambda = 100$ nm. The other geometrical parameters are: $w = 5$ μm, $v = 5$ μm, $h = 150$ nm, $k = 5$ μm. The region in which no trap forms is left of the dashed line.

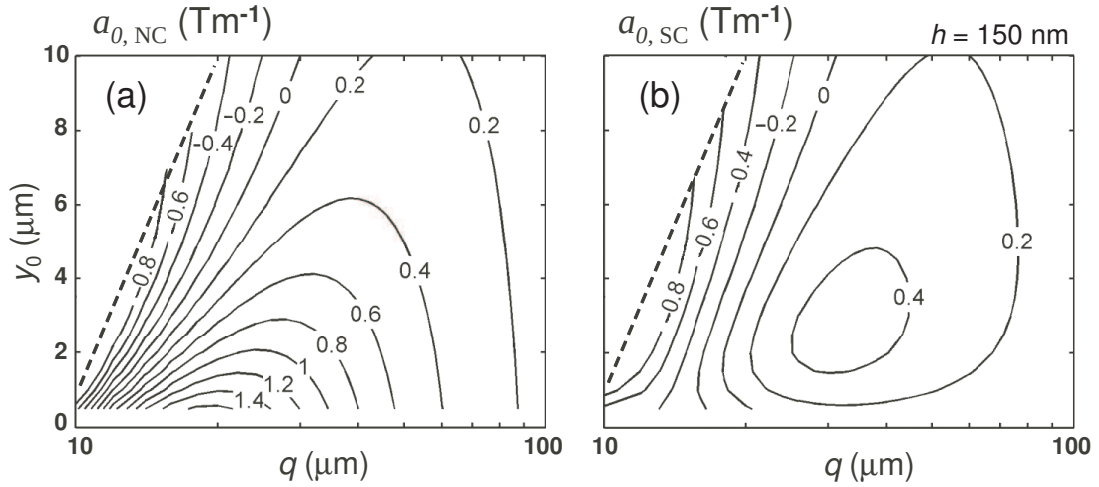

Figure 2.13: Trap parameter a_0 in the normal conducting chip (a) and in the superconducting chip (b). $I_0 = 1$ mA. The horizontal axis, in logarithmic scale, represents the distance q between the two offset wires, and the vertical axis, in linear scale, represents the position of the magnetic trap y_0. Data are represented in the plane x=0. $\lambda = 100$ nm. The other geometrical parameters are: $w = 5$ μm, $v = 5$ μm, $h = 150$ nm, $k = 5$ μm. The region in which no trap forms is left of the dashed line.

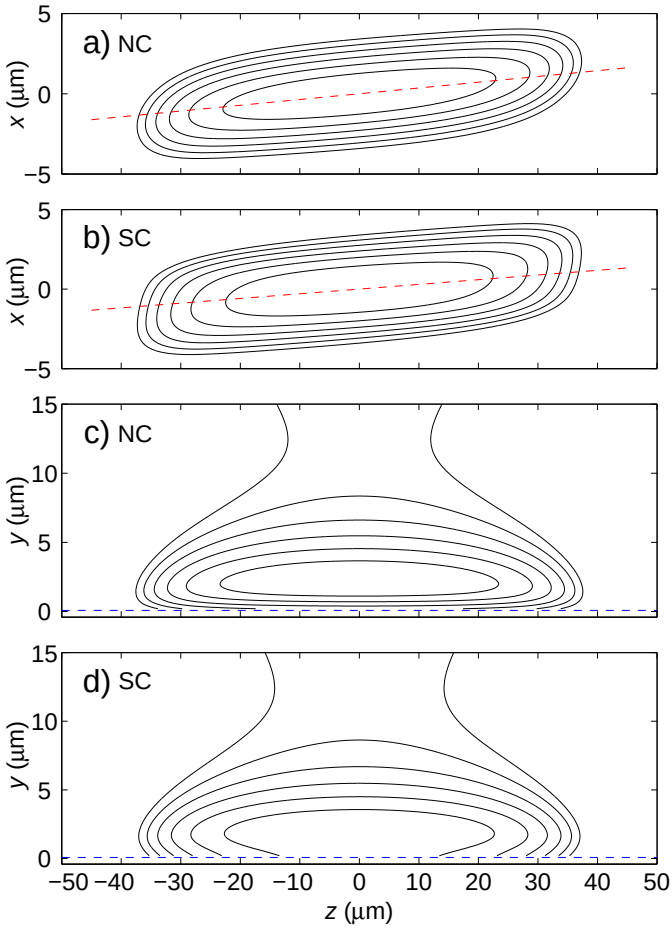

Figure 2.14: Isopotential curves of a magnetic trap generated by the atom chip shown in Figures 2.3 and 2.9 in the superconducting (SC) and in the normal conducting (NC) state. The applied currents are the same in both cases: $I_2 = 0.2$ mA, $I_1 = I_3 = 1.4$ mA ($\alpha = 1$, $\beta = 0.0714$ and $I_S = 3$ mA) and $I_0 = 2$ mA. A homogeneous offset field $b_{0,ext} = 25$ μT is externally applied to stabilize the micro trap against Majorana losses. Following the notation of Figures 2.3 and 2.9, the geometry of the microstructure is described by $w = 5$ μm, $v = 5$ μm, $h = 150$ nm, $q = 100$ μm and $k = 5$ μm. The penetration depth is 100 nm in the superconducting wires. The two upper graphs show the isopotential curves in the plane $y = y_0$. The dashed lines in the two upper graphs represent the longitudinal axis of the micro trap, which is rotated about the y-axis as explained before. The two lower graphs show the isopotential curves in the plane perpendicular to the chip surface along the longitudinal axis. The dashed lines in the two lower graphs represent the chip surface. The parameters of this microtrap are represented in Table 2.1. The magnetic field changes by 4 μT per contour.

	SC	NC
a (Tm^{-1})	6.9	8.4
a_0 (Tm^{-1})	99	151
b_0 (μT)	2.5	2.3
b_z (mTm^{-2})	6	56
y_0 (μm)	2.0	2.3
w_l (s^{-1})	$2\pi \cdot 95$	$2\pi \cdot 92$
w_r (s^{-1})	$2\pi \cdot 1650$	$2\pi \cdot 2020$
ψ	1.7°	2.1°

Table 2.1: Parameters of the micro trap shown in Figure 2.14 for the superconducting (SC) and the normal conducting (NC) states. The parameters are explained in the text. The oscillation frequencies, w_r and w_l, have been calculated for ^{87}Rb.

as well as a slight increase of the longitudinal oscillation frequencies.

The most remarkable feature of the superconducting chip is a significant decrease of the trap depth towards the surface, which is a consequence of the reduction of a shown in Figure 2.6. The trap depth is reduced by about 80% in the superconducting chip.

In conclusion, differences between superconducting and normal conducting chips become relevant when the distance between the microtrap and the superconducting surface is smaller than the width of the wires. The most dramatic consequence of the Meissner effect is a significant reduction of the trap depth. Although the results on the Meissner effect shown in this chapter have been obtained for the specific example of Figures 2.3 and 2.9, these conclusions can be generalized to any atom chip made with superconducting thin films.

2.8 Magnetic microtraps generated by superconducting loops

Magnetic traps can be generated by means of persistent currents in superconducting loops. Figure 2.15 shows a theoretical example of microstructure consisting of ten concentric loops with a trapping geometry in the upper side. All the loops are on the same plane. The width and the thickness of the wires are 2 μm and 150 nm, respectively. The separation between every two neighbour wires is 2 μm. The penetration depth is assumed to be 100 nm. The magnetic trap is generated over the trapping geometry by persistent currents flowing in the loops. These persistent currents are created by applying a homogeneous external field $\boldsymbol{B}_L$ along the normal direction of the surface during the onset of superconductivity. In this way, a certain amount of magnetic flux is frozen in every loop. The homogeneous external field is switched off after reaching the superconducting state. The trap forms over the trapping geometry in absence of any external current or field.

The currents in the loops are calculated from the inductance matrix $\pounds$ of the system.

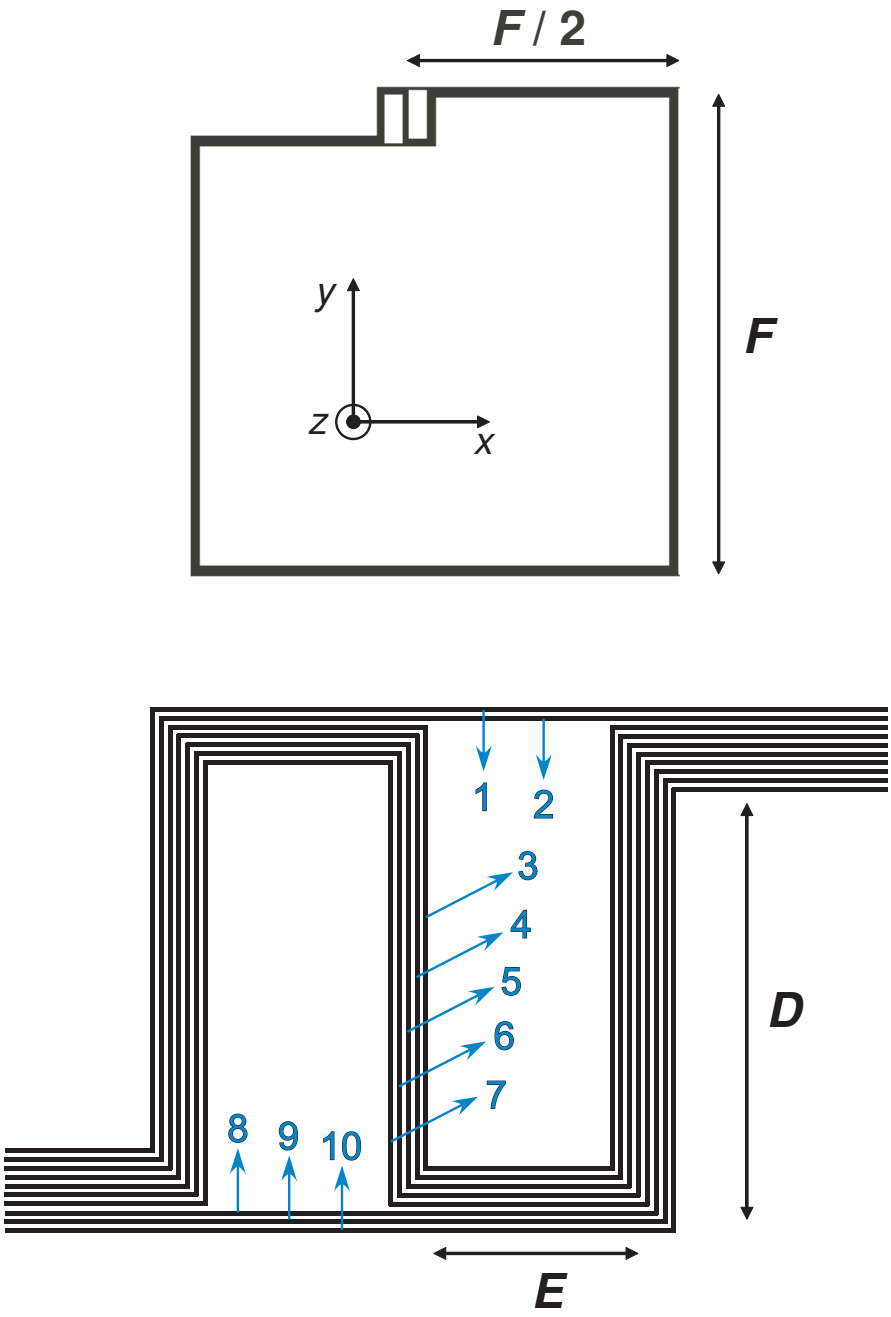

Figure 2.15: Theoretical design of a superconducting microstructure consisting of ten superconducting closed circuits. Upper part: the whole structure. Lower part: Trapping geometry. The width and the thickness of the wires are 2 μm and 150 nm respectively. The separation between every two neighbor wires is 2 μm. An Ioffe trap forms over the trapping geometry. The longest side of the outer loop is $F = 2$ mm. The parameters of the trapping geometry are $D = 200$ μm and $E = 100$ μm.

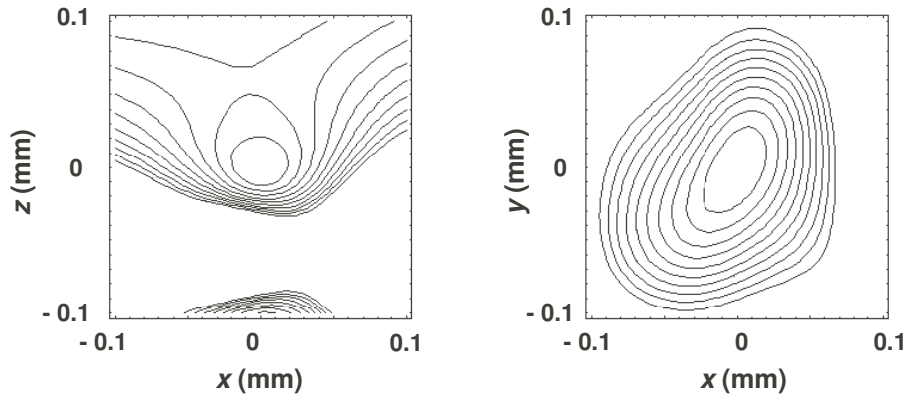

Figure 2.16: Isopotential lines of the magnetic microtrap generated by the microstructure of Figure 2.15. The plains containing the trap center are represented. The contour lines mark the field strength at multiples of 10^{-5} T, counting from the value of the magnetic-field modulus at the center of the microtrap.

The equation to be solved is: $|\boldsymbol{B}_L|\boldsymbol{A} = \pounds \boldsymbol{I}$. Here, $\boldsymbol{A}$ is a vector the components of which are the areas of the loops, and $\boldsymbol{I}$ is the vector the components of which are the electric currents flowing in the loops. The self-inductance of a loop can be approximated by the sum of the self-inductances of the straight sections that form the loop plus the sum of the mutual inductances of all the pairs of straight sections contained in the loop. The self-inductances of the straight sections are calculated with Equation 2.13. This assumption neglects any effect in the corners, which is a good approximation given the dimensions of the system. Likewise, the mutual inductance between two loops can be calculated as the sum of the mutual inductances of all the pairs of elements between the two loops. For the geometry of the present example, in which the length of the loop is much higher than its width, the mutual inductance of each pair of straight sections is sensibly the same as that of two filaments, which can be calculated using classic analytical formulas [Gro46].

The obtained solution is: $\boldsymbol{I} = |\boldsymbol{B}_L|\ (108, 61, 39, 37, 34, 34, 33, 42, 46, 84)$, where $\boldsymbol{I}$ and $|\boldsymbol{B}_L|$ are expressed in ampere and tesla, respectively. The order of the components of $\boldsymbol{I}$ is the same as the wire numbers in Figure 2.15. The outer loop, which corresponds to the first position of the vector $\boldsymbol{I}$, carries the highest current. Therefore, the magnetic field $|\boldsymbol{B}_L|$ has to be chosen so that the outer loop does not exceed the critical current density. With a magnetic field of $|\boldsymbol{B}_L| = 0.23$ mT the trap depth is 25 μT and the oscillation frequencies for ^{87}Rb are $2\pi \cdot (320, 222, 389)$ s^{-1}. The magnetic field at the center of the trap is 97 μT, which is enough to prevent the thermal ultracold atoms from spin-flip loses. The trap forms at 60 μm from the surface. The magnetic trap is represented in Figure 2.16. This magnetic trap could be loaded by using optical tweezers, following a similar procedure as explained in the next chapter.

Chapter 3

Experimental apparatus for superconducting atom chips

The purpose of the apparatus is to realize experiments with ultracold atomic gases in magnetic microtraps near superconducting microstructures. Ultracold rubidium clouds are produced and manipulated in a ultra-high-vacuum chamber, the interior of which is shown in Figure 3.1. Its main parts are a room-temperature trap setup and a superconducting microstructure generating a magnetic microtrap (superconducting microtrap). The room-temperature trap setup accomplishes the initial phases of the experiment. It consists of three pairs of coils and two straight vertical wires that provide the magnetic fields for collecting, trapping and cooling the atoms. After cooling in the room-temperature trap setup, the atomic cloud is transported to the magnetic microtrap by means of optical tweezers. The superconducting microstructure is attached to the cold surface of the Helium flow cryostat.

In this chapter, the technical design and the operation of the experimental system is described. As an overview, Figure 3.2 represents a typical experimental cycle, which has been optimized to increase the final atom number in the magnetic microtrap. The experiment cycle starts with compressing and cooling a cloud of ^{87}Rb atoms in a magneto-optical trap (MOT). After polarization-gradient cooling, the atoms are loaded into the quadrupole magnetic trap generated by the MOT coils. Then, the atoms are magnetically transferred into an Ioffe trap, in which radio-frequency evaporative cooling is accomplished. After evaporative cooling, the ultracold atom cloud is transported to the superconducting microtrap by means of optical tweezers. Finally, the atoms are loaded into the superconducting microtrap, and the experiments are carried out.

3.1 Ultra high vacuum

Ultra high vacuum (UHV) is a requirement for experiments with ultra cold atoms. The UHV chamber is represented in Figure 3.3. An ion-getter pump (IP1) and a titanium-

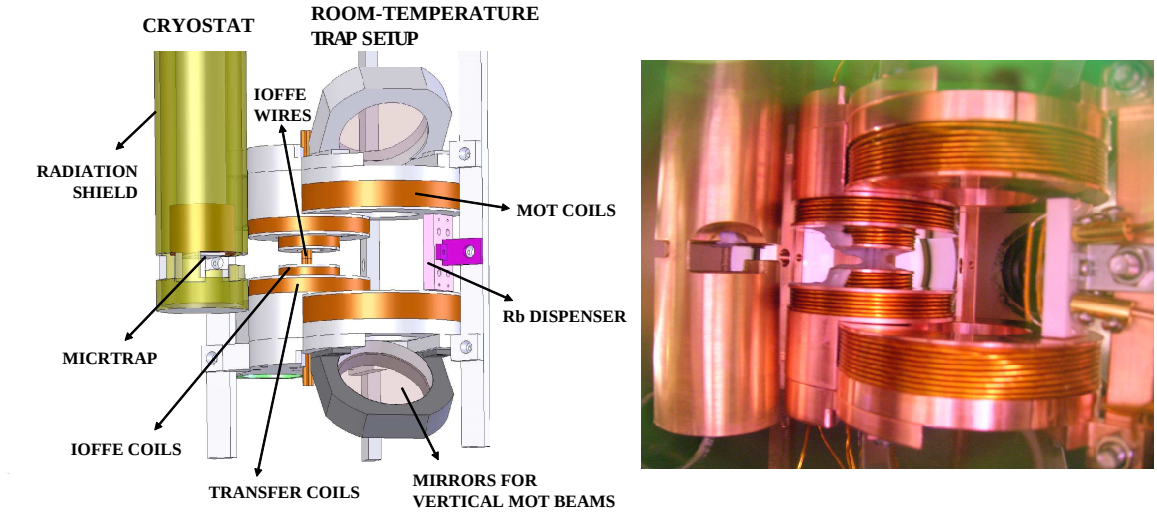

Figure 3.1: Drawing and photograph of the interior of the vacuum chamber, which contains a room-temperature trap setup and a superconducting microtrap. The pressure is below 10^{-11} mbar. Rubidium atoms are supplied by two dispensers in the room-temperature trap setup. A magneto-optical trap (MOT) is produced between the MOT coils. An Ioffe magnetic trap is generated by two Ioffe coils in combination with two Ioffe wires. Transport of the atoms from the room-temperature trap setup to the superconducting microtrap is accomplished by means of optical tweezers. The microstructure generating the microtrap is cooled with a Helium flow cryostat.

sublimation pump (TiP) keep the pressure below 10^{-11} mbar. The ion-getter pump has a nominal pumping speed of 75 l/s. During the experiments, the titanium-sublimation pump is cooled with liquid nitrogen to enhance its efficiency. The pressure gauge (P) is placed near the place where the experiments are carried out. The top flange of the vacuum chamber has a long vertical extension (C) that encloses the cryostat. This vertical extension has a translator (T) that allows changing the vertical position of the cryostat as desired. A reservoir (R) on the top flange contains a coolant that absorbs the heat dissipated by the currents applied to the room-temperature trap setup. The room-temperature trap setup is thermally connected to the reservoir through a thick metallic bar. The top flange also includes some electrical feedthroughs that transfer electric current through the chamber wall to the room-temperature trap setup.

The main vacuum chamber is communicated with a small vacuum chamber that hosts a two-dimensional optical dipole trap (2D-MOT). This small chamber is evacuated by an ion-getter pump (IP2) with a nominal pumping speed of 20 l/s. The 2D-MOT serves as efficient source of ultracold atoms, and it was designed and build by Philipp Wicke [Wic05]. The 2D-MOT has not been operated during the experiments presented in this thesis, and for that reason, it will not be described. Instead of the 2D-MOT, the two rubidium dispensers of the room-temperature trap setup are used as source of atoms.

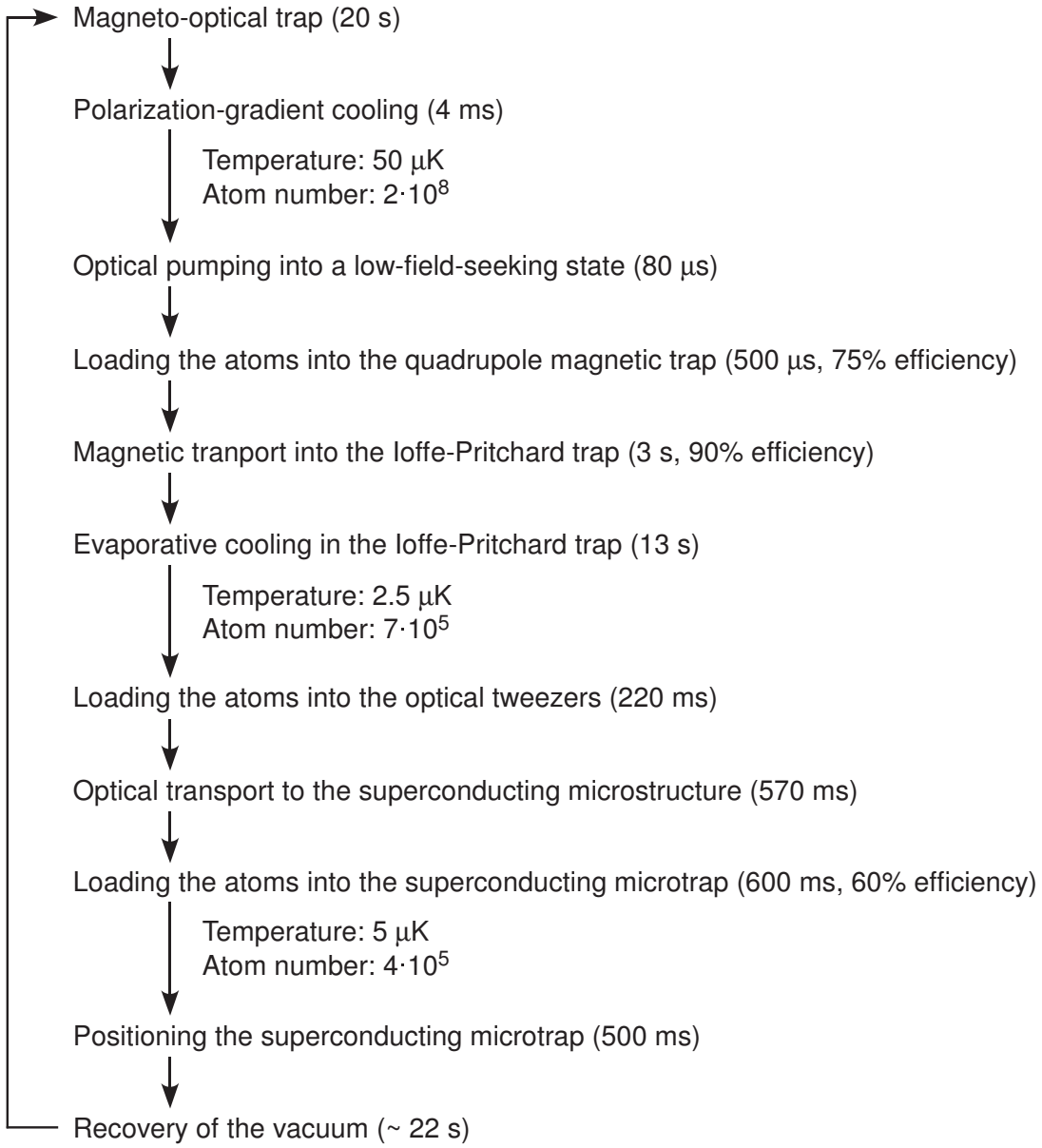

Figure 3.2: Experimental cycle. The durations of phases are written in brackets. The total duration is 60 s.

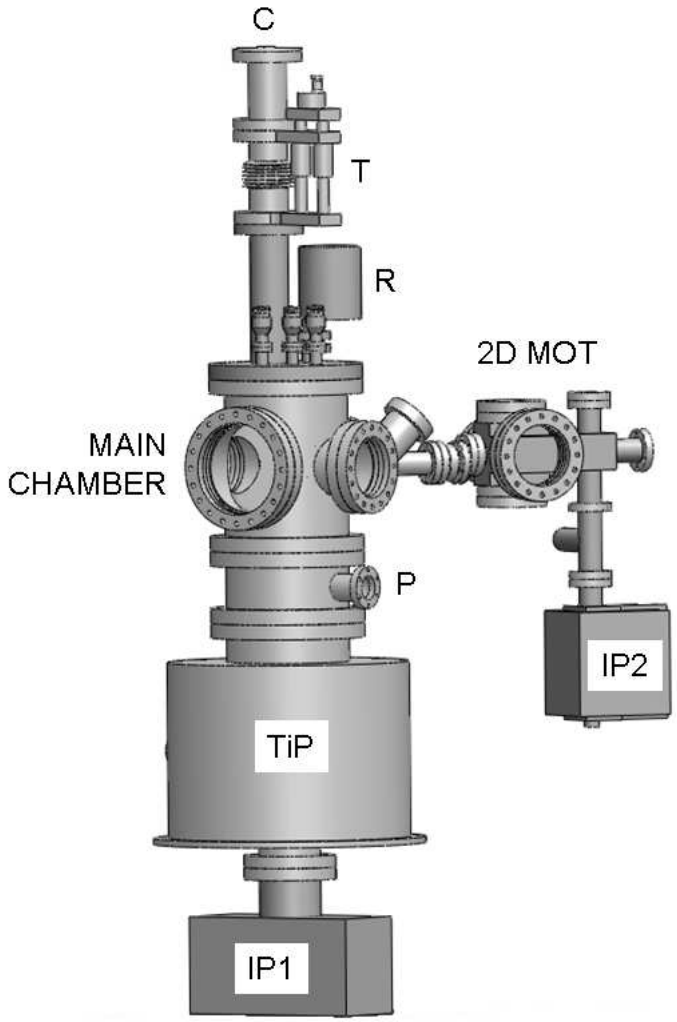

Figure 3.3: External parts of the vacuum chamber, which consists of a main chamber and a 2D-MOT. It includes a pressure gauge (P), two ion-getter pumps (IP1 and IP2), a titanium-sublimation pump (TiP), a coolant reservoir (R), an extension (C) to enclose the cryostat and a translator (T) to position the cryostat.

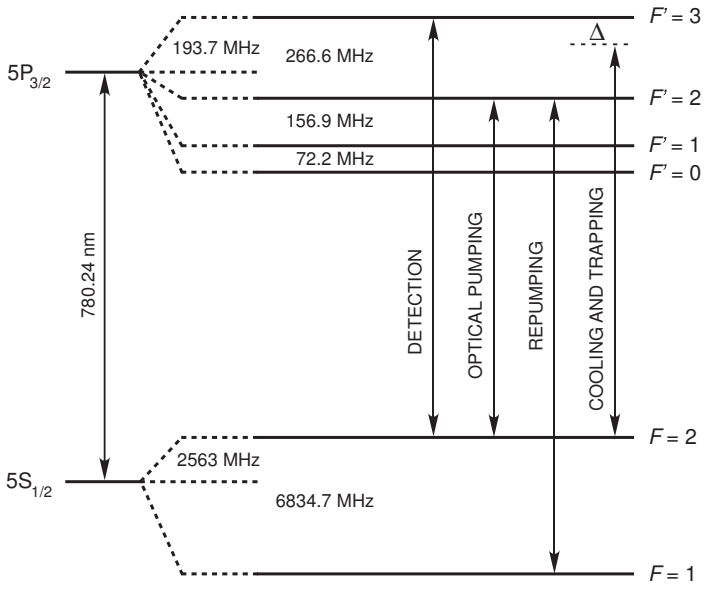

Figure 3.4: Diagram of the hyperfine structure of ^{87}Rb and the laser frequencies used for the experiment.

The main vacuum chamber has four big viewports that give optical access to the interior. The interior of the chamber is build with low-outgassing materials in order to preserve the ultra-high vacuum. They include kapton-insulated wires, stainless-steal screws, thermal-conductive ceramic glue[1], and metallic structures made of oxygen-free-high-conductivity copper (OFHC copper). The ceramic glue is used to attach and to thermally contact the Ioffe wires to the room-temperature structure. Every component has been cleaned in ultra-sonic bath in three different steps: first with a degreaser[2], afterwards with acetone, and finally with ethanol. Powder-free latex gloves were used when handling any vacuum part because organic substances like oils from human skin have large outgassing rates. After assembly, the vacuum chamber was baked out at 200°C for ten days. During baking, the chamber was evacuated by a turbo-molecular pump. This procedure removes the substances -mostly water- that are in the pores of the metallic chamber walls. After baking, the chamber was closed with UHV valves.

3.2 The laser system

Figure 3.4 shows the hyperfine structure of ^{87}Rb and the laser frequencies used in the experiment. The cooling beams are red detuned by Δ from the $|5\ ^2S_{1/2}, F = 2\rangle \rightarrow |5\ ^2P_{3/2}, F = 3\rangle$ transition. During the MOT phase, a repump laser at the $|5\ ^2S_{1/2}, F = 1\rangle \rightarrow |5\ ^2P_{3/2}, F = 2\rangle$ transition is overlapped with the cooling beams in order to prevent the atoms from accumulating in the $|5\ ^2S_{1/2}, F = 1\rangle$ state. Before loading the atoms into

[1]Ceramic adhesive 920, Cotronics Corp. 131 47th Street, Brooklyn, NY 11232.
[2]Aqueous solution with Tickopur RW 77.

the magnetic trap, they are optically pumped to the $|5\ ^2S_{1/2}, F = 2, m_F = +2\rangle$ state by means of a σ^+-polarized beam at the $|5\ ^2S_{1/2}, F = 2\rangle \rightarrow |5\ ^2P_{3/2}, F = 2\rangle$ transition. The detection beam is in resonance with the the $|5\ ^2S_{1/2}, F = 2\rangle \rightarrow |5\ ^2P_{3/2}, F = 3\rangle$ transition.

The laser system is mounted on an optical table nearby the vacuum chamber. It supplies laser radiation at the required frequencies. Figure 3.5 shows the main elements of the laser system. The laser light is generated by three grating-stabilized Hitachi-HL7851G diode lasers, an injected Sharp-GH0781JA2C diode laser, and a tapered amplifier from the company Eagleyard Photonics. In general, the Hitachi diode lasers are suitable for grating stabilization [Wie99], although their output power is not higher than 25 mW. On the contrary, the Sharp diode lasers, which are difficult to stabilize with gratings, have a high nominal output power ($P = 120$ mW). For these reasons, the Sharp diode lasers are typically locked by injection with laser beams emitted by grating-stabilized diode lasers. In all the cases, the linewidth (FWHM) of the emitted laser light is lower than 1 MHz.

The first grating-stabilized diode laser is locked to the cross-over signal between the hyperfine transitions $|5\ ^2S_{1/2}, F = 2\rangle \rightarrow |5\ ^2P_{3/2}, F = 2\rangle$ and $|5\ ^2S_{1/2}, F = 2\rangle \rightarrow |5\ ^2P_{3/2}, F = 3\rangle$ by using a Doppler-free polarization-spectroscopy method [Wie76]. The beam emitted by this diode laser is split in several beams by means of $\lambda/2$-plates and polarization cubes. One of these beams is frequency shifted into the transition $|5\ ^2S_{1/2}, F = 2\rangle \rightarrow |5\ ^2P_{3/2}, F = 2\rangle$ by an acousto-optical modulator (AOM). This is the beam for optical pumping. Another beam is frequency shifted to the transition $|5\ ^2S_{1/2}, F = 2\rangle \rightarrow |5\ ^2P_{3/2}, F = 3\rangle$, which is used for detection. The last beam is shifted into resonance with the transition $|5\ ^2S_{1/2}, F = 2\rangle \rightarrow |5\ ^2P_{3/2}, F = 2\rangle$ in order to provide a reference beam for the beat-signal locking scheme of the second grating-stabilized diode laser.

The second grating-stabilized diode laser is locked at the cooling frequency by using a beat-signal locking scheme. This method employs the beat signal arising from the interference of a beam from this diode laser and the reference beam from the first grating-stabilized diode laser. This requires to overlap the optical paths of both beams. The frequency of the beat signal, which is the difference between the frequencies of the two beams, is measured using an ultrafast photodiode. The frequency of the beat signal is adjusted to a constant value of 248 MHz ($\Delta = -18MHz$) during the MOT phase, and to a time-dependent linear ramp from 248 MHz to 212 MHz ($\Delta = -54MHz$) during polarization-gradient cooling. In order to generate enough laser power for cooling, the laser light from the second grating-stabilized diode laser is used to inject the tapered amplifier.

The third grating-stabilized diode laser is locked to the repump frequency by means of a Doppler-free polarization-spectroscopy method. This grating-stabilized diode laser is used to inject a Sharp diode laser that supplies enough laser power for the repump beam.

The laser beams for optical pumping, detection, cooling, and repump are guided with single-mode optical fibers[3] towards the optical setup located around the vacuum chamber.

[3]The optical fibers and the laser-beam couplers are made by the company Schäfter and Kirchhoff GmbH,

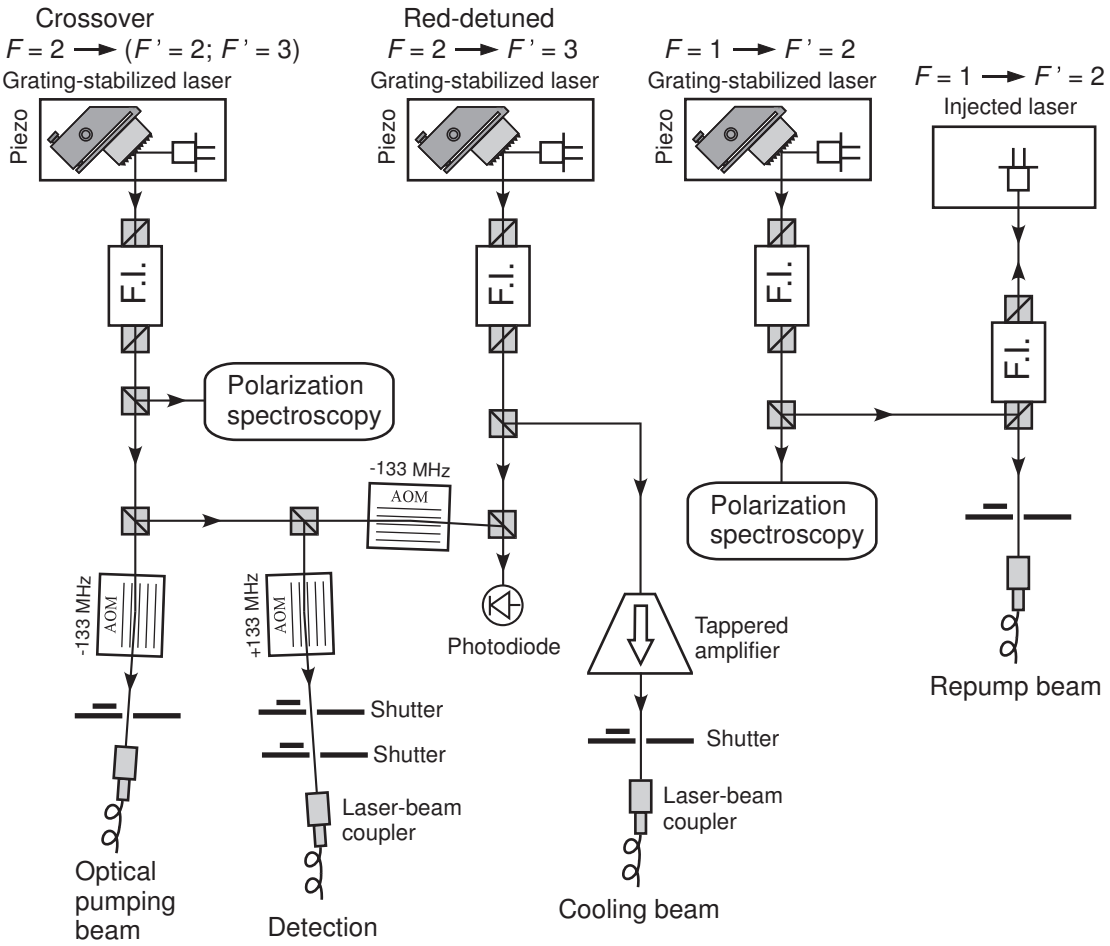

Figure 3.5: Diagram of the laser system. The laser power is generated by three grating-stabilized diode lasers, an injected diode laser, and a tapered amplifier. A Faraday isolator (F.I.) is placed in front of every diode laser to avoid retroreflected light. The diagram only shows the important elements. Optical elements like mirrors, retardation plates, polarization plates and lenses are not shown. The laser beams for optical pumping, detection, cooling, and repumping are coupled into single-mode optical fibers by means of laser-beam couplers.

Both detection and optical pumping are carried out with very short light pulses of 100 and 80 μs, respectively. The durations of these light pulses have to be the same in all the experiments in order to obtain reproducible results. Such light pulses are done by switching on and off the radiofrequency sources of the respective AOMs, the rise time of which is shorter than 500 ns. Because it is very difficult to completely cut the radiofrequency signal, it is convenient to use mechanical shutters in combination with the AOMs in order to completely extinguish the laser beams. Each mechanical shutter opens a few milliseconds before the respective AOM is switched on, and close a few milliseconds after the AOM is switched off. The length of time that the mechanical shutters need to open or close is approximately 1 ms. Both the cooling and the repump beams are shut only with mechanical shutters. In a typical experiment cycle, the duration of these two beams is 20 s.

3.3 The room-temperature trap setup

The first steps of the experimental cycle are realized between the coils of the room-temperature trap setup. They are the MOT, polarization-gradient cooling, loading the atoms into the magnetic quadrupole trap of the MOT coils, magnetic transfer into the Ioffe trap and radio-frequency evaporative cooling. The required magnetic fields are supplied by three pairs of coils and two Ioffe wires (see Fig. 3.1). For the magnetic design of the room-temperature trap setup I have used a magnetic-field-computation routine made by Christian Silber [Sil06].

3.3.1 The magneto-optical trap

The mangeto-optical trap (MOT) employs both optical and magnetic fields to capture, compress and cool the hot atomic gas ejected by the dispensers. Figure 3.6 shows the sketch of the MOT. The two MOT coils are driven with opposite electric currents in order to generate a magnetic quadrupole field,

$$\boldsymbol{B}_{QP} = \begin{pmatrix} -\alpha x \\ 2\alpha y \\ -\alpha z \end{pmatrix}, \tag{3.1}$$

where y is the vertical coordinate, and x and z are the horizontal coordinates with origin at the center of the MOT. The modulus of $\boldsymbol{B}_{QP}$ cancels at the center of the MOT, and increases linearly in all directions. The vertical magnetic gradient is twice the horizontal magnetic gradient α. Six cooling beams are organized to form three mutually perpendicular standing waves that intersect at the zero of the magnetic field. Counterpropagating cooling beams have opposite circular polarizations. The cooling beams for the MOT are red detuned by $\Delta = -18$ MHz from the $|5\,^2S_{1/2}, F = 2\rangle \rightarrow |5\,^2P_{3/2}, F = 3\rangle$ transition (see

Kieler Str. 212, D-22525 Hamburg.

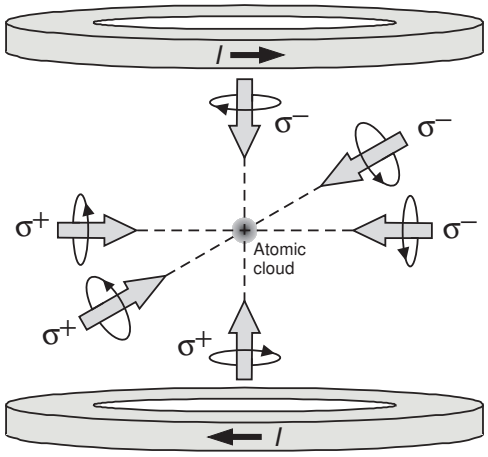

Figure 3.6: Sketch of the MOT. The atoms are trapped and cooled by six circularly-polarized laser beams in combination with the quadrupole magnetic field of two coils in anti-Helmholtz configuration. The laser frequency has to be red-detuned with respect to an atomic transition.

Figure 3.4). The detuning frequency Δ has been experimentally chosen to optimize the final atom number and temperature. The cooling beams have a 15-mm-diameter top-hat profile, and their total power is 120 mW.

The physical processes involved in the MOT are rather complex [Tow95]. For a simple description of these processes, let us consider the force of the laser beams on the moving atoms. This radiative force has two components: a velocity-dependent force that damps the atomic speed, thus reducing the temperature of the gas, and a position-dependent force that traps the atoms around the zero of the magnetic field. The origin of these forces is the imbalance in radiation pressures in each of the three pairs of laser beams. These imbalances arise from the Doppler and Zeeman shifts of slowly moving atoms in the linearly inhomogeneous magnetic field $\boldsymbol{B}_{QP}$.

The cooling beams have the undesired effect of pumping some of the atoms to the $|5\ ^2P_{3/2}, F = 2\rangle$ state, from where they decay to $|5\ ^2S_{1/2}, F = 1\rangle$ and $|5\ ^2S_{1/2}, F = 2\rangle$. To prevent the atoms from accumulating in $|5\ ^2S_{1/2}, F = 1\rangle$, a repump laser at the $|5\ ^2S_{1/2}, F = 1\rangle \rightarrow |5\ ^2P_{3/2}, F = 2\rangle$ transition is overlapped with the cooling beams. The total laser power of the repump beams is 15 mW.

The realized MOT has the typical dimensions for experiments with ^{87}Rb. The inner and outer radii of each coil are 17 and 32 mm, respectively. The coil thickness is 10 mm. The distance between the MOT coil centers is 42 mm. This geometry allows to generate the required magnetic gradients with a heat dissipation lower than 0.4 W per coil. The horizontal magnetic gradient is $\alpha = 0.07$ T/m. The MOT phase happens in the first 20 s of the experiment cycle. The rubidium atoms are supplied by two dispensers, that are heated by electric currents, producing an ejection of hot rubidium gas. The dispensers are driven with 6 A in the first 12.5 s of the MOT phase.

3.3.2 Polarization-gradient cooling

After the MOT phase, the temperature is reduced by polarization-gradient cooling. This is accomplished by ramping down the magnetic field of the MOT within 500 μs, and keeping the cooling beams at full power for another 3.5 ms. During polarization-gradient cooling, the detuning frequency Δ is linearly ramped from -18 MHz to -54 MHz. These values were chosen to minimize the final temperature. After polarization-gradient cooling the thermal cloud contains $2 \cdot 10^8$ atoms at 50 μK.

The principle of polarization-gradient cooling has been exhaustively described in Reference [Dal89]. Every pair of counter-propagating laser beams forms a linearly-polarized standing wave. The electric field of this standing wave has the same modulus everywhere, but its direction rotates through an angle 2π over one wavelength. The interaction of the moving atoms with the electric field originates a non-adiabatic mechanism that damps the atom velocity below the Doppler limit.

There is a fundamental reason why polarization-gradient cooling cannot produce a Bose-Einstein condensate. During polarization-gradient cooling, spontaneous emissions are always present, even in atoms with the lowest velocities. Since spontaneous emissions never cease, it is impossible to cool the atoms below the recoil temperature, which is about 0.3 μK. The recoil temperature corresponds to the kinetic energy of an atom absorbing or emitting a photon. But the main limitation of polarization-gradient cooling refers to both absorption of scattered light and light-induced collisions. If the density of the atom cloud becomes too large, light scattered by one atom is reabsorbed by others, causing a repulsion between them. Moreover, inelastic collisions between atoms with one in the excited state (S+P collisions) generally produce a heating effect, which is significant if the atom density is high. A final temperature of about ten times the recoil temperature is the practical limit.

The present setup has the disadvantage that the laser power during polarization-gradient cooling is the same than in the MOT phase. This does not allow to minimize the effects of reabsorbed photons and light-induced collisions. Generally, laser power for polarization-gradient cooling needs to be lower than in the MOT phase.

Limitations of laser cooling can be overcome with evaporative cooling in the Ioffe trap. In order to load the atoms into the Ioffe trap, they are first loaded into the magnetic quadrupole trap generated by the MOT coils. That is not a difficult task given that both the MOT and the magnetic quadrupole trap have a common center and share the same symmetry. From the quadrupole trap the atoms can be magnetically transferred into the Ioffe trap.

3.3.3 Magnetic quadrupole trap

After polarization-gradient cooling, the atoms are loaded into the magnetic quadrupole trap generated by the MOT coils. Just before the atoms are loaded into the quadrupole

trap, they are pumped into $|5\ ^2S_{1/2}, F = 2, m_F = 2\rangle$, which is a low-field-seeking state, by using a σ^+-polarized beam in resonance with the $|5\ ^2S_{1/2}, F = 2\rangle \rightarrow |5\ ^2P_{3/2}, F = 2\rangle$ transition. Optical pumping lasts 80 μs. The optical pumping beam has a power of 1 mW and a gaussian profile of 10.9 mm $1/e^2$-diameter. The optical pumping beam is aligned with the vertical axis of the MOT. During optical pumping, the two MOT coils are driven with electric currents in the same direction in order to generate a locally homogeneous magnetic field parallel to the vertical axis of the MOT. This field is required to avoid that the quantization axis of optical pumping is altered by the Earth magnetic field, which is not compensated in the vacuum chamber.

After optical pumping, the electric currents of the MOT coils are linearly ramped in 500 μs to generate a magnetic quadrupole trap with a vertical gradient of 0.6 T/m. This is more than enough to compensate gravity, which is equivalent to the magnetic force produced by 0.15 T/m. The trap depth is 5 mT, which corresponds to a temperature of $T = (\mu_B/\mathrm{K_B})$ (5 mT) $\simeq$ 3 mK, which is more than one order of magnitude higher than the atom cloud temperature.

Evaporative cooling cannot be carried out in the quadrupole trap generated by the MOT coils for two reasons. First, the MOT coils cannot supply sufficiently strong confinement to reach the collision rate required for a quick thermalization. Second, the low-field-seeking state of the atoms is not conserved near the center of the quadrupole trap, where the adiabatic approximation (see Section 2.3) cannot be applied and where the atoms are lost by spin-flip transitions. Evaporative cooling requires to compress the atom cloud and to transfer it into the Ioffe trap, in which the magnetic field does not cancel at any point.

3.3.4 Magnetic transfer into the Ioffe trap

The magnetic transfer starts just after the atoms are loaded into the quadrupole trap. Figure 3.7 and Table 3.1 show the features of the coils and wires that provide the trapping fields. The wires of each pair of coils are arranged so that the two coils transport opposite currents, thus generating a magnetic quadrupole field. By changing the electric currents applied to the pairs of coils, the magnetic quadrupole trap is moved from the position of the MOT to the position of the Ioffe trap. The evolution of the currents is a succession of linear ramps, as shown in Figure 3.8. The Ioffe wires are driven with opposite currents of 14.5 A during the magnetic transfer and during evaporative cooling in the Ioffe trap. The Ioffe trap forms at the end of the transfer.

Figure 3.9 shows the isopotential lines of the magnetic-field modulus at six different times of the magnetic transfer, which correspond to the six marks (a), (b), (c), (d), (e) y (f) in Figure 3.8. Figure 3.9(a) shows the magnetic quadrupole trap at the initial time of the magnetic transfer, when only the MOT coils carry an electric current. Subsequently, the magnetic zero of the quadrupole trap is shifted towards the Ioffe wires by increasing the current in the transfer coils, as shown in Figure 3.9(b). Figure 3.9(c) represents the time at which the trap becomes more dominated by the transfer coils than by the MOT coils. At

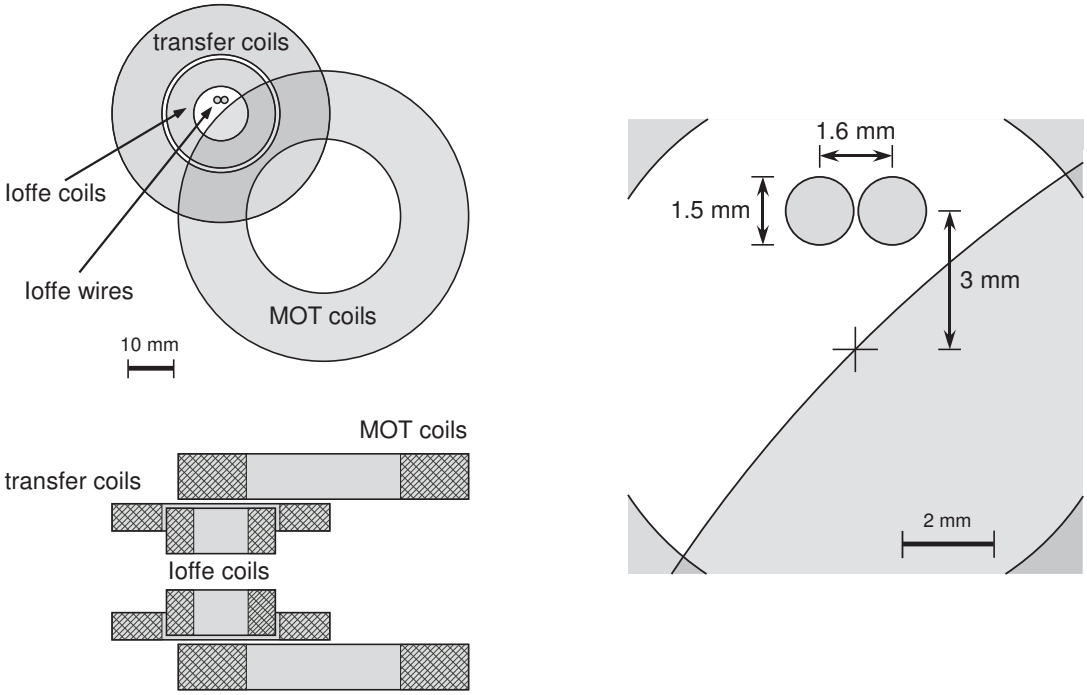

Figure 3.7: Top view (above) and cross section (below) of the coils and wires that form the room-temperature trap setup. The right side shows a magnified part of the top view with the Ioffe wires. These drawings have been done to scale.

this time a relative minimum of the magnetic potential is formed near the quadrupole trap. This relative minimum can trap some atoms that do not return to the quadrupole trap. Two recipes have been followed to increase the distance between this relative minimum and the center of the quadrupole trap, and in this way, to avoid the loss of atoms. The first one is to not ramp down the current of the MOT coils until the current of the transfer coils has reached its maximum value. The second recipe is that the distance between the axis of the MOT coils and that of the transfer coils should be equal or shorter than the outer radius of the MOT coils.

Figure 3.9(e) shows the transformation of the quadrupole trap into the Ioffe trap. Before the Ioffe configuration is reached, a second quadrupole trap comes up near the Ioffe wires, and the magnetic potential takes the form of a double well. As the current in the MOT coils is reduced, the two quadrupole traps, which have perpendicular axes, merge and the Ioffe trap forms. If the currents in the Ioffe wires were ramped up at the end of the transfer instead of at the beginning, the second quadrupole trap would be so close to the wire surface that the trap depth would be reduced during the transformation of the two quadrupole traps into the Ioffe trap. This would not have to be a problem since only the hottest atoms would be removed, but it is convenient to take this effect

	MOT coils	Transfer coils	Ioffe coils
Inner radius (mm)	17	13	6
Outer radius (mm)	32	24	12
Thickness (mm)	10	6	10
Distance between coils (mm)	42	24	18
Number of wire windings	151	50	46
Horizontal gradient α (T/m/A)	0.10	0.07	0.20

Table 3.1: Main features of the coils of the room-temperature trap setup. The distance between coils is measured between the central points of the two coils. The two coils of every pair of coils are driven with opposite currents to generate a quadrupole field. The magnetic gradient of the quadrupole field in the horizontal directions is denoted by α. The magnetic gradient in the vertical direction is 2α.

into account if the Ioffe wires are thick or if they are very close to each other. The trap depth is 1.1 mT during the whole magnetic transfer, which corresponds to a temperature of $T = (\mu_B/K_B)$ (1.1 mT) $\simeq 750$ μK

The Ioffe trap forms by superposition of the magnetic quadrupole field generated by the coils and the magnetic field generated by the Ioffe wires. The longitudinal oscillation frequency of the Ioffe trap is mainly determined by the magnetic-field curvature generated by the Ioffe wires. The shorter the distance between the Ioffe wires, the stronger the magnetic confinement along the long axis of the Ioffe trap. In this setup, a short distance between the two Ioffe wires has been chosen so that even a low current in the Ioffe wires can provide a tight longitudinal confinement.

Once the magnetic transfer has been accomplished, the currents in the Ioffe coils and in the transfer coils are 3.5 A and 2.5 A, respectively. The Ioffe wires carry a constant current of 14.5 A during the transfer. The Ioffe trap is very suitable for evaporative cooling. Since the magnetic field does not cancel at any point of the Ioffe trap, the atoms do not suffer from spin-flip looses. The magnetic field at the trap center is 10^{-4} T. The strong confinement of the trap, which is harmonic near its center, allows efficient evaporative cooling. The radial and longitudinal oscillation frequencies are $\omega_r = 2\pi \cdot 220$ s^{-1} and $\omega_l = 2\pi \cdot 40$ s^{-1}, respectively.

3.4 Detection system

Physical properties of the atom cloud, such as the temperature or the density profile, are measured by taking absorption images. The optical setup for absorption imaging is represented in Figure 3.10. There are two detection beams; each of them has a gaussian intensity profile of 10.9 mm 1/e^2-diameter. The detection beam 1 is aligned with the Ioffe trap of the room-temperature trap setup. The lens L1 creates an image of the shadow of

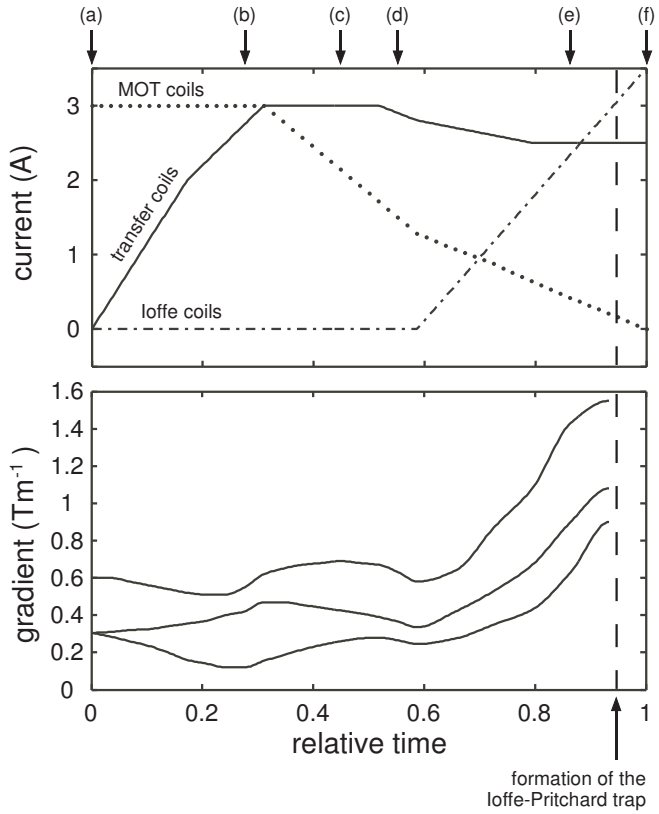

Figure 3.8: Upper graph: evolution of the electric currents in the MOT coils, the transfer coils and the Ioffe coils during the magnetic transfer. Lower graph: magnetic gradients in the three main perpendicular axes of the magnetic quadrupole trap. The Ioffe trap forms at the end of the magnetic transfer. The Ioffe wires carry a constant current of 14.5 A during the transfer. The six marks, from (a) to (f), indicate the times of the plots shown in Figure 3.9.

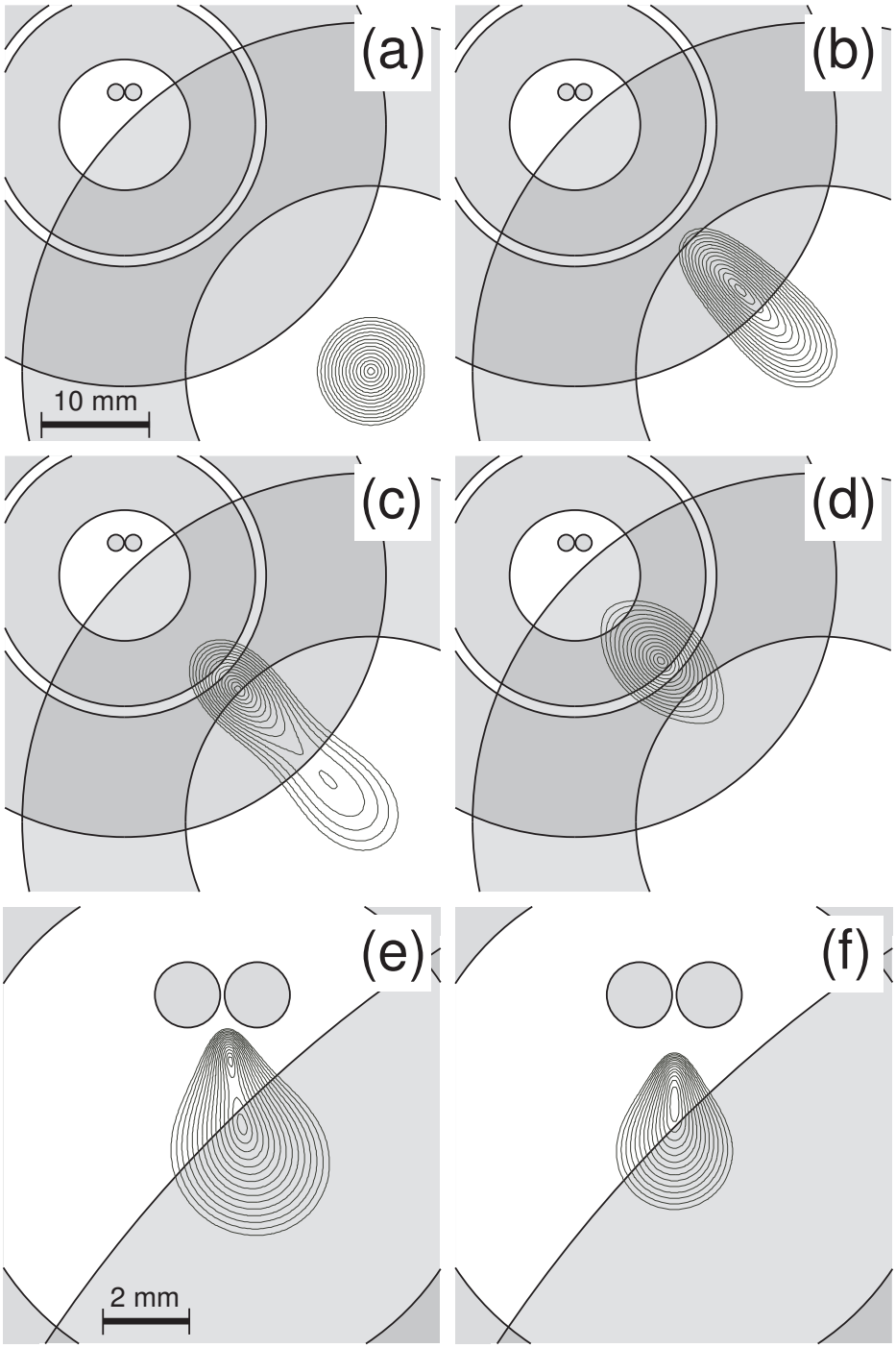

Figure 3.9: Isopotential lines of the magnetic-field modulus at six different times of the magnetic transfer, which correspond to the six marks in Figure 3.8. Graph (a) is the initial time, when only the pair of MOT coils are driven with electric current. Graph (f) is the Ioffe trap in which evaporative cooling is carried out. The magnetic field changes by 0.1 mT per contour. The drawings are done to scale.

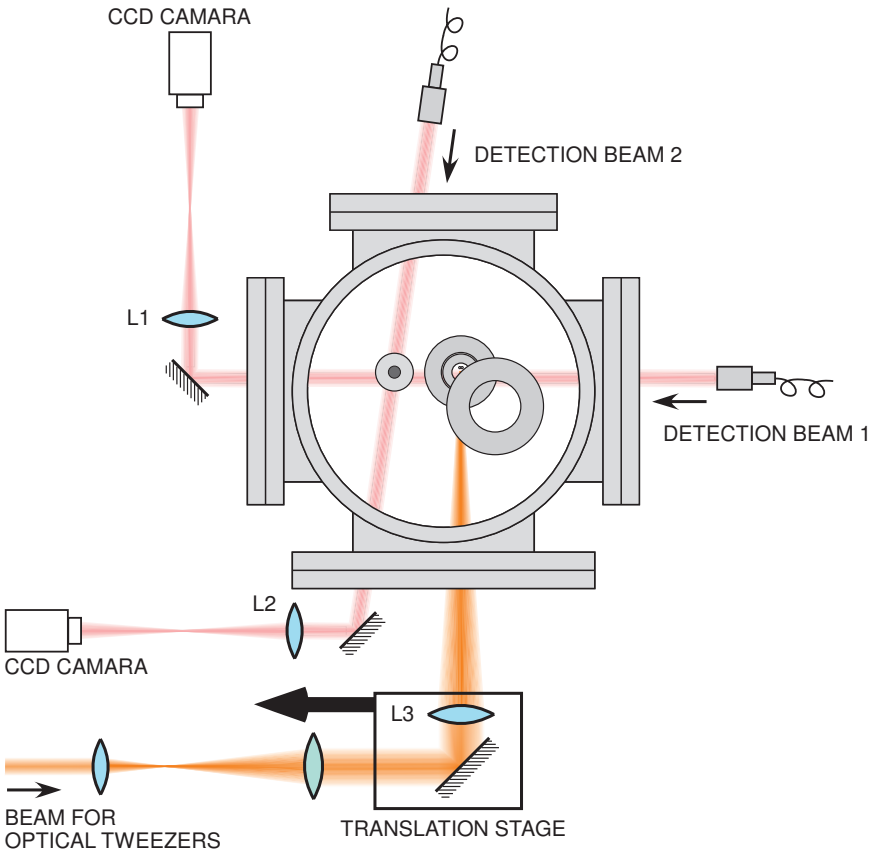

Figure 3.10: Detection system. Beams 1 and 2, which are in resonance with the $|5\ ^2S_{1/2}, F = 2\rangle \rightarrow |5\ ^2P_{3/2}, F = 3\rangle$ transition, are used to image the atoms in the Ioffe trap and in the superconducting microtrap, respectively. Also depicted are the optical tweezers that are used to transport the atoms from the room-temperature trap setup to the superconducting microtrap. The optical tweezers will be thoroughly described in Section 3.6.

the atom cloud onto the CCD camera[4]. The focal length of L1 is 200 mm. The diffraction limit of the image resolution is given by 1.22 $\lambda/NA \simeq 7.5$ μm, where $\lambda \simeq 780$ nm is the wavelength of the light and NA is the numerical aperture. This resolution is enough for the purposes of this beam, which are to align the optical tweezers with the Ioffe trap, and to estimate the atom number during evaporative cooling in order to improve the radio-frequency curve. The magnification $M \simeq 2.2$ was measured by time-of-flight images of the atom cloud as explained in Section 3.5.2 below. The 6.45-μm side of the square pixels on the CCD camera corresponds to 2.9 μm in the object plane.

The detection beam 2 images the atom cloud at the superconducting microtrap. The achromatic lens L2 is placed as close as possible from the vacuum chamber in order to enhance the optical resolution. The diffraction limit is 3 μm. L2 has a diameter of 51 mm and a focal length of 150 mm. The 6.45-μm size of the pixels on the CCD camera corresponds to 4.8 μm ($M \simeq 1.3$) in the object plane.

The intensity distribution $I(y,z)$ of the detection beam after passing through the atom cloud is

$$I(y,z) = I_0(y,z)\ \mathtt{e}^{-D(y,z)}, \tag{3.2}$$

where $I_0(y,x)$ is the intensity distribution before absorption. The optical density is

$$D(y,z) = \sigma \int n(x,y,z)\ \mathtt{d}x, \tag{3.3}$$

where σ is the scattering cross section and $n(x,y,z)$ is the atomic density. The atomic density profile can be then calculated as

$$N(y,z) = \int n(x,y,z)\ \mathtt{d}x = \frac{1}{\sigma}\ \mathtt{Log}\left(\frac{I(x,y)}{I_0(x,y)}\right). \tag{3.4}$$

During detection, every atom scatters approximately 100 photons until the atom velocity is so high that the Doppler shift prevents the atom from absorbing more photons. The probability that an atom absorbs a photon depends on the frequency shift of the detection laser and therefore on the atom velocity. It also depends on the laser polarization and the atomic spin orientation. The physical information of the detection process is given by the scattering cross section $\sigma \simeq 0.135$ pm [Ste].

The atom density profile $N(y,z)$ is calculated from the relative intensity $I(y,z)/I_0(y,z)$. To obtain the relative intensity, three different images are taken in the following order: an image $I_{atom}(y,z)$ of the detection beam in the presence of atoms, a reference image $I_{ref}(y,z)$ of the detection beam without atoms, and finally, a background image $I_{back}(y,z)$ without detection beam. The relative intensity is

$$\frac{I(y,z)}{I_0(y,z)} = \frac{I_{atom}(y,z) - I_{back}(y,z)}{I_{ref}(y,z) - I_{back}(y,z)}. \tag{3.5}$$

The detection-laser pulse used for each of the three images lasts 100 μm. The three images are taken within 800 ms.

[4]Theta system SIS1-s285 from Elektronnik GmbH. http://www.theta-system.com/.

3.5 Production of a BEC in the Ioffe trap

3.5.1 Bose-Einstein statistics

The collective quantum properties of ultracold gases become macroscopically observable when the de Broglie wavelength λ_{dB} is larger than the spacing between particles. The de Broglie wavelength λ_{dB} describes the position uncertainty associated with the thermal momentum distribution of the particles. It can be calculated as $\lambda_{dB} = \sqrt{(2\pi\hbar^2)/(mK_BT)}$, where m is the mass of the particle and K_B is the Boltzmann constant. The relation between λ_{dB} and the spacing between particles is given by the phase-space density $D = n\lambda_{dB}^3$, where n is the density of particles.

When the phase-space density is low, the gas behaves as a system of classical particles governed by the Maxwell-Boltzmann statistics. As the phase-space density is increased, the quantum properties of matter emerge. Then, bosons like ^{87}Rb become indistinguishable particles obeying Bose-Einstein statistics. This states that several bosons can occupy the same quantum state. As a gas of bosons is cooled and compressed, it undergoes a transition to a phase in which a huge number of particles occupy the quantum state of the lowest energy. This transition occurs when the phase-space density reaches a value of $D \simeq 2.612$. In this phase, which is called Bose-Einstein condensate (BEC), the single-particle ground-state wavefunctions overlap and form a macroscopic wavefunction. Particles forming the BEC behave as a coherent ensemble without individuality. Such a phase would not be possible with fermions, which obey the Fermi-Dirac statistics. Each quantum-mechanical state cannot be occupied by more than one fermion. At very low temperature, fermions tend to fill energy states from the lowest up, with one particle per quantum-mechanical state. This is called a Fermi sea or a degenerate Fermi gas.

3.5.2 Radiofrequency evaporative cooling

The high phase-space density required to produce a BEC is obtained by means of evaporative cooling in the Ioffe trap [Ket96]. To date, evaporative cooling is the only method leading to BEC. It is based on the preferential removal of the hottest atoms of the thermal cloud, followed by thermalization of the remaining gas by elastic collisions. In the present setup, the hottest atoms are removed by inducing transitions to quantum states in which the atoms are not trapped any more, as represented in Figure 3.11. This is accomplished with an oscillating magnetic field at the frequency ω_{rf}, which lies in the radiofrequency range. The oscillating magnetic field is applied through the Ioffe wires. Atomic transitions occur at the positions $\boldsymbol{r}$ where the resonance condition

$$\hbar\omega_{\mathrm{rf}} = g_F\mu_B B(\boldsymbol{r}) \tag{3.6}$$

is satisfied. The higher the frequency of the signal, the higher the distance from the trap center. The radiofrequency signal starts removing atoms of the outer positions of the

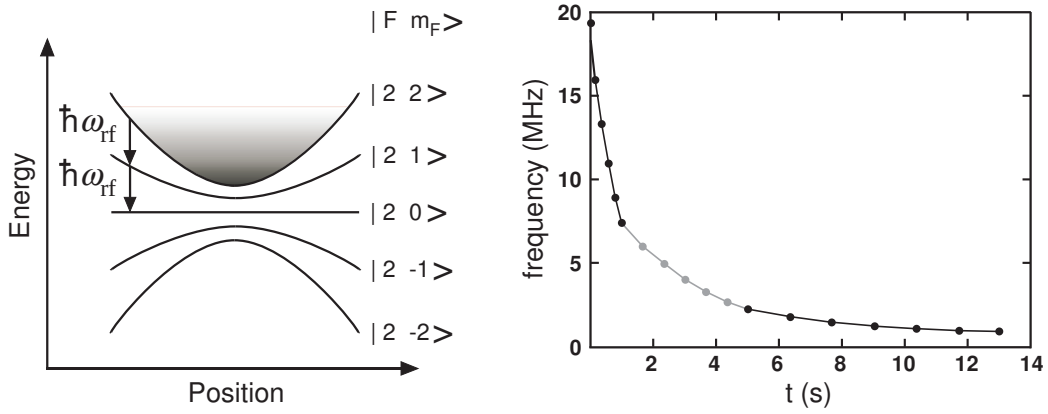

Figure 3.11: The graph on the left side illustrates the principle of evaporative cooling by induced radiofrequency transitions. The potential energy is represented as a function of the position for the different Zeeman states. The atoms can be trapped only in the $m_F = 2$ and $m_F = 1$ states. Atoms with the highest energies are removed from the trap by inducing transitions to states in which the atoms are not trapped any longer. The graph on the right side shows the frequency ramp used to cool the atom cloud. It consists of three exponential curves.

cloud, where only the hottest atoms can be. Evaporative cooling is carried out with a frequency sweep from the outer positions to the inner positions of the Ioffe trap. The frequency sweep is represented in Figure 3.11 and consists of three logarithmic curves that have been optimized independently by means of measuring both temperature and atom number at the end of every logarithmic curve. After 13 s of radiofrequency evaporative cooling a BEC of $2 \cdot 10^5$ atoms is formed.

3.5.3 Characterization of the Ioffe trap

The magnetic field at the center of the Ioffe trap, $B_0 = 0.1$ T, is measured by finding the radiofrequency that removes all the atoms, $\omega_{\mathrm{rf},0} = g_F \mu_B B(\vec{0})/\hbar$. It agrees with the value calculated in Section 3.3.4. The oscillation frequencies of the Ioffe trap are measured by making the condensate oscillate. This is done with sudden changes in the electric current of either one of the Ioffe coils (radial oscillations) or the Ioffe wires (longitudinal oscillations). The measured oscillation frequencies, $\omega_r = 2\pi \cdot 272$ s^{-1} and $\omega_l = 2\pi \cdot 45$ s^{-1}, are slightly different from those calculated in Section 3.3.4. These differences can be caused by external magnetic fields or by small deviations of the geometry of wires. The strong confinement of the Ioffe trap favors atomic collisions, enhancing the efficiency of evaporative cooling.

3.5.4 Free expansion of the condensate

Figure 3.12 shows time-of-flight pictures of the expanding atom cloud after switching off the Ioffe trap. The atom cloud falls freely, depicting a parabolic curve that is used to cal-

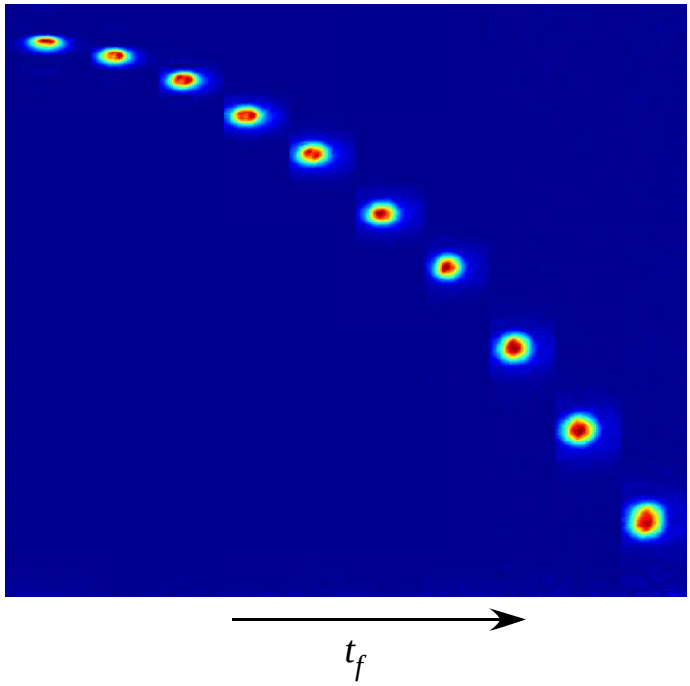

Figure 3.12: Images of the Bose-Einstein condensate for ten different times of flight t_f, from 2 ms to 20 ms in steps of 2 ms. The typical parabolic trajectory of a free fall is manifest.

ibrate the size of the image (see Section 3.4). The condensed atoms form a density peak at the center of the atom cloud. This dense core is surrounded by a diffuse cloud of thermal atoms. In general, a freely expanding condensate is characterized by an anisotropic velocity distribution [Dal99, Ket99]. While the velocity distribution in an expanding thermal cloud is isotropic according to the equipartition principle, the width of the velocity distribution of a expanding condensate is inversely proportional to the spatial extension of its wavefunction, which is related to the oscillation frequencies of the Ioffe trap. Therefore, the condensate expands more rapidly in the direction in which it was initially most confined, and the aspect ratio of the condensate inverts. The fundamental origin of this anisotropy is the Heisenberg uncertainty relation. Additionally, the internal energy of the interatomic interactions is converted into kinetic energy in an anisotropic way when the condensate is released from the Ioffe trap [Cas96].

3.5.5 Measurement of the critical temperature

The critical temperature T_C of the condensate is obtained by measuring the temperature of the thermal cloud at the phase transition. In general, the temperature T of an ideal thermal gas can be calculated from the density distribution after a certain time t_f of free expansion. The density distribution of the expanded cloud is the convolution of the density distribution before expansion with the density distribution of an expanded cloud

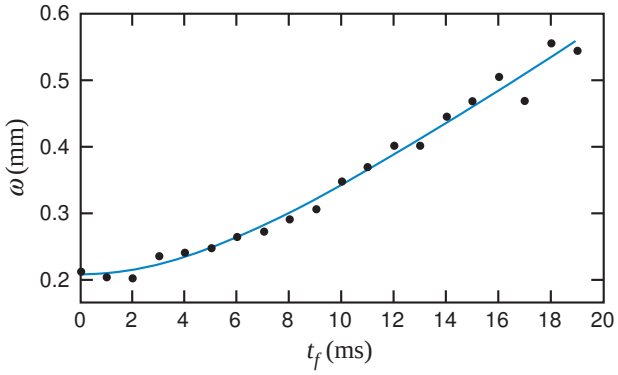

Figure 3.13: Time evolution of the freely expanding thermal cloud at the critical temperature. Both measured data and best-fit curve are plotted.

whose initial distribution is a point. The density of the cloud before expansion has a gaussian distribution because the Ioffe trap is harmonic. Its 1/e-radius is denoted by σ_0. The density distribution of an expanded cloud whose initial distribution is a point is also gaussian, and its 1/e-radius is $\sqrt{(2\,K_B\,T\,t_f^2)/m}$, where m is the atomic mass of ^{87}Rb, according to the Maxwell-Boltzmann law. The convolution of these two gaussian distributions is another gaussian distribution, the 1/e-radius of which is

$$\sigma(t_f) = \sqrt{\sigma_0^2 + 2\frac{K_B T}{m} t_f^2}. \tag{3.7}$$

The temperature T is obtained by fitting this formula to the measured 1/e-radius of the thermal cloud for different times of flight t_f. At the phase transition, the best-fit value is $T_C = (256 \pm 8)$ nK. The measured data and the best-fit curve are represented in Figure 3.13.

An equation for the critical temperature can be deduced with the noninteracting harmonic-oscillator model [Dal99],

$$T_C = 0.9\hbar\omega_{ho} N^{1/3}, \tag{3.8}$$

where $\omega_{ho} = (\omega_r^2\ \omega_l)^{1/3}$. Different experimental results [Ens96, Mew96] have proved this formula to be a very good approximation. From this formula and the measured critical temperature, the number of condensed atoms is calculated: $N \simeq 5.5 \cdot 10^4$. This is similar as the value obtained with the optical density.

3.6 Optical tweezers for ultracold atoms

3.6.1 Optical dipole potential

Optical dipole potentials rely on the dispersive interaction between the electric dipole moment of the atom and the electric field of a far-detuned light. In general, when a polarizable atom is illuminated with laser radiation, the electric field induces an atomic

electric dipole moment that oscillates at the same frequency ω as the laser. The in-phase component of the induced dipole oscillation originates the optical dipole force. The out-of-phase component of the induced dipole oscillation corresponds to scattering of photons and the associated radiation pressure.

The optical dipole force, which is conservative, dominates the radiation pressure when the laser frequency is far detuned from any atomic transition. Conversely, the radiation pressure is dominant when the laser frequency is near an atomic transition, as what happens in a MOT or during polarization-gradient cooling. The realization of an optical dipole trap requires large detunings and low radiation pressures. The following expressions are derived for the optical dipole potential and the scattering rate in the case of a two-level atom in a far-detuned radiation field [Gri00]:

$$U_{\mathtt{dip}}(\boldsymbol{r}) = -\frac{3\pi c^2}{2\omega_0^3}\left(\frac{\Gamma}{\omega_0-\omega}+\frac{\Gamma}{\omega_0+\omega}\right) I(\boldsymbol{r}), \tag{3.9}$$

$$\Gamma_{\mathtt{sc}}(\boldsymbol{r}) = \frac{3\pi c^2}{2\hbar\omega_0^3}\left(\frac{\omega}{\omega_0}\right)^3\left(\frac{\Gamma}{\omega_0-\omega}+\frac{\Gamma}{\omega_0+\omega}\right)^2 I(\boldsymbol{r}), \tag{3.10}$$

where ω_0 is the resonance frequency, $I(\boldsymbol{r})$ is the intensity of the radiation and Γ is the decay rate. These formulas also assume linear polarization. If $\Delta = \omega - \omega_0 < 0$ (red detuning), the dipole potential is negative and the atoms are attracted into the light field. Potential minima are then found at positions with maximum intensity. If $\Delta > 0$ (blue detuning), the dipole interaction repels atoms out of the field, and potential minima correspond to minima of the intensity.

The realized optical dipole trap employs an Ytterbium fiber laser[5] that emits light at $\lambda = 1064$ nm. Formulas 3.9 and 3.10, which are deduced for a two-level atom, can be also used for the multi-level structure of ^{87}Rb. The reasons can be explained as follows. The closest atomic transitions to the laser wavelength λ are those belonging to the D line doublet, which consists of the $^2S_{1/2} \rightarrow {}^2P_{1/2}$ spectral line at 795 nm and the $^2S_{1/2} \rightarrow {}^2P_{3/2}$ spectral line at 780 nm. The splitting of this doublet, which is associated to the energy of the spin-orbit coupling in the excited state, is much smaller than the detuning Δ of the laser light. For that reason, the detuning Δ is the leading term of the total energy, and the spin-orbit structure can be ignored. The ^{87}Rb atom can be then approximated by a two-level system with a simple $S \rightarrow P$ transition, the decay rate $\Gamma = 2\pi \cdot 5.9$ MHz of which is an average of the decay rates of the two components of the doublet.

In the present setup, the optical dipole trap is formed by focusing the 1064-nm gaussian beam with an achromatic lens, the focal length of which is 250 mm. The light intensity maximum is the center of the generated optical dipole trap. As shown in Figure 3.10, the collimated gaussian beam is first magnified with a telescope in order to get the desired beam waist at the 250-mm lens. The beam waist w is measured at several positions along the laser beam. The beam waist is obtained by finding the theoretical gaussian function

[5]Ytterbium Fiber Laser, Model YLD-10-1064-Lp, IPG Photonics, http://www.ipgphotonics.com

that best fits the measured beam profile. The beam profile is obtained with a blade that blocks a variable portion of the cross section of the beam, and with a powermeter that measures the power of the unblocked part of the beam. The measured $1/e^2$ beam waist radius at the focus is 18 μm. The $1/e^2$ beam waist radius at other positions obeys the following law:

$$w(z) = w_0\sqrt{1+\left(\frac{z}{z_R}\right)^2}, \tag{3.11}$$

where $z_R = \pi w_0^2/\lambda$ is the Rayleigh length. The oscillation frequencies of the dipole trap, $\omega_r = 2\pi \cdot 2100$ s^{-1} and $\omega_l = 2\pi \cdot 30$ s^{-1}, are calculated from the applied power $P = 500$ mW and the measured waist $w_0 = 18$ μm using Formulas 3.9 and 3.11. The applied power P has been chosen to produce a trap depth of 150 μK. The scattering rate is about 1 s^{-1}. The measured lifetime of the thermal atoms in the optical dipole trap is 0.7 s.

The optical elements are aligned in order to overlap the optical dipole trap and the Ioffe trap. A rough positioning of the optical elements is done with the help of a infrared viewer. Afterwards, a fine aligning procedure is performed by moving the 250-mm lens with a manual micropositioning stage that is placed on the air-bearing translation stage (see Figure 3.10). The fine aligning procedure is described as follows. First, a resonant laser beam is overlapped with the trapping 1064-nm beam. Then, an ultracold atom cloud is produced in the Ioffe trap using the cooling techniques described above. Subsequently, a short pulse of the resonant beam is sent, and the number of atoms remaining in the Ioffe trap is measured. This operation is repeated for different positions of the 250-mm lens. The shorter the distance of the resonant beam to the Ioffe trap, the lower the number of remaining atoms. As the resonant beam approaches the Ioffe trap, a higher number of atoms are removed from the Ioffe trap by photon absorbtion. The best alignment corresponds to the position of the 250-mm lens that minimizes the number of remaining atoms. Lastly, a final adjustment of the 250-mm lens is carried out by optimizing the number of atoms loaded into the optical dipole trap.

The transfer to the optical dipole trap is accomplished by ramping the laser light up to $P = 500$ mW in 200 ms and then ramping down the magnetic field in 20 ms. The ramping durations have been chosen to optimize the transfer. The longitudinal axis of the optical dipole trap is parallel to the longitudinal axis of the Ioffe trap, thus favoring a high efficiency in transferring the atoms between the two traps. The loading efficiency is almost 100 %.

3.6.2 Optical transport of ultracold atoms

After loading the optical dipole trap, the atom cloud is optically transported from the Ioffe trap over a distance of 44 mm to the cold surface of the cryostat. For this purpose, the 250-mm lens is moved with an air-bearing linear translation stage[6] which is placed next to

[6]Model ABL 1000, Aerotech, http://www.aerotech.com/

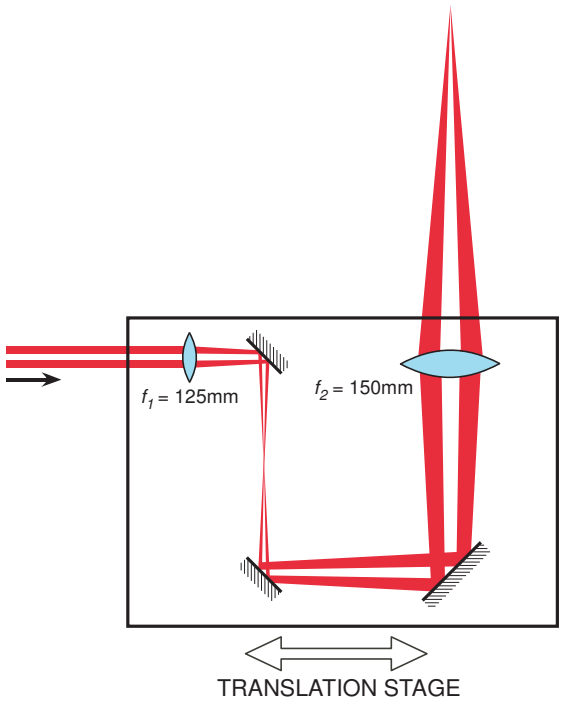

Figure 3.14: Sketch of the two-beam configuration for the optical tweezers.

the vacuum chamber (Figure 3.10). The air-bearing stage is levitated with pressurized air and is driven by a brushless servo motor that guarantees minimal vibration and that has an accuracy of 0.2 μm. Smooth transport is accomplished within 0.5 s using a sinusoidal acceleration profile with a maximum acceleration of 1 m/s^2. Both smooth transport and minimal vibration are requirements for adiabatic transport because fluctuations in the trap position heat the ultracold atom cloud [Sav97]. With this acceleration profile there are no oscillations of the atomic cloud at the end of the optical transport. As opposed to what happens in other experiments with optical tweezers [Gus02], in this setup the optical dipole trap moves in the direction of highest confinement, thus compensating inertia even during a very quick transport.

3.6.3 Two-beam optical tweezers

The two-beam configuration is depicted in Figure 3.14. Before realizing the single-beam optical tweezers, a two-beam configuration was built and tested, but in the end it was not used for the reasons that I explain in this section. Nevertheless, it is worth describing it because of the possible applications in other setups.

Two collimated beams are aligned parallel with the direction of motion of the optical tweezers. The two beams are focussed by two lenses that are placed on the translation stage. The length of the optical path between the two lenses is approximately the focal length of the first lens, $f_1 = 125$ mm, plus twice the focal length of the second lens, $f_2 = 150$

mm. This makes the two beams cross at about 300 mm behind the second lens. In the two-beam configuration the optical dipole trap forms by contribution of the two beams. The potential minimum forms at the crossing point. The two beams have perpendicular polarizations to avoid interference effects. The two-beam configuration guarantees that the two beams cross and form a trap for any position of the air-bearing translation stage.

In the single-beam configuration, the trap depth and the radial and longitudinal oscillation frequencies cannot be controlled independently because they three depend on only two variables, which are the laser power P and the beam waist w_0. The trap depth and the radial and longitudinal oscillation frequencies increase linearly with P/w_0^2, $\sqrt{P}/w_0^2$ and $\sqrt{P}/w_0^3$, respectively. Single-beam traps are always characterized by high radial oscillation frequencies and very week longitudinal confinements. This strong anisotropy can be a limitation when transferring atoms from or to another trap such as the Ioffe trap or the superconducting microtrap. In general, the transfer efficiency between two traps is better when their symmetries are similar. The two-beam configuration allows independent control over the longitudinal oscillation frequency by means of a third variable, which is the angle between the crossing beams. For example, if 4.2 W are focussed into a beam waist of $w_0 = 40$ μm, the radial and longitudinal oscillation frequencies will be $2\pi \cdot 1240$ Hz and $2\pi \cdot 7.5$ Hz, respectively. By splitting this single beam into two beams of 2.1 W with a cross angle of 3°, the longitudinal oscillation frequency becomes $2\pi \cdot 47$ Hz, and the radial oscillation frequencies remain the same.

The two-beam configuration requires to use areas of the lens surfaces that are far off the optical axis. Even if the lenses are achromatic, the beams are affected by some spherical aberration. As a consequence, each beam reaches its narrowest waist, $w_0 \simeq 40$ μm, at a different position from where the two beams cross. It has been observed that the focus of each beam is located at about 10 mm from the cross point. In principle, this deviation does not have to be a drawback to create the optical dipole trap, which forms at the positions where the two beams cross. Nevertheless, it is important to consider that the beam waist at the cross point, $w \simeq 100$ μm, is higher than w_0 in order to calculate correctly the trap depth and the oscillation frequencies.

The problems associated with the two-beam configuration can be explained using Figure 3.15. It shows the number of atoms in the two-beam trap as a function of time. The optical dipole trap was kept at rest at the loading position during these measurements. Three different values of the laser power have been used: 2.8, 4.2 and 5.6 W. The crossing angle is 3°. When the power is 2.8 W, the trap is not deep enough to trap all the atoms. When the power is 4.2 W, most of the atoms are loaded into the trap. After loading, the atom cloud gets a bit colder due to the loss of the hottest atoms. Unpredictably, when the power is further increased to 5.6 W, the atoms are quickly lost after loading. The origin of these losses can be explained with neither the higher scattering rate $\Gamma_{\mathtt{sc}}(\boldsymbol{r})$ nor inelastic collisions in the tighter trap. What is more, all the atoms are suddenly lost if the translation stage starts moving towards the superconducting microstructure.

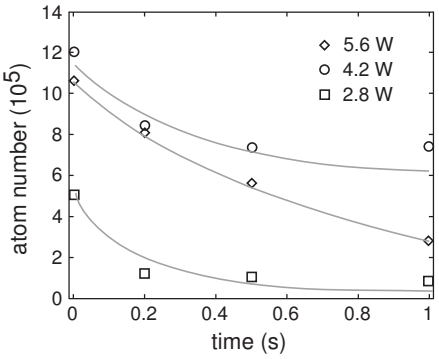

Figure 3.15: Temporal evolution of the number of atoms in the optical dipole trap with the two-beam configuration for three different laser powers.

My hypothesis is that the atom losses are related with the closeness of the Ioffe wires. The ceramic glue covering the Ioffe wires is illuminated with the laser light of the optical dipole trap. The high energy density of the laser light heats and evaporates part of the ceramic surface, producing an gas ejection that removes the trapped atoms. With the single-beam configuration the energy density on the ceramic surface is much smaller and the evaporation does not occur. This is because the beam waist w_0 with the single-beam configuration has to be smaller than with the two-beam configuration in order to have enough longitudinal confinement. If w_0 is smaller, less laser power produces the needed trap depth. Because of the shorter Rayleigh length with the single-beam configuration, the beam expands faster from the focal point and so the illuminated ceramic surface is larger and the energy density on it is reduced. There is another evidence that supports this hypothesis. The lifetime of the trapped atoms in the two-beam configuration is slightly increased if the optical dipole trap is moved immediately after loading the atoms to a position in which the ceramic glue is not illuminated.

The two-beam configuration does not allow to apply enough laser power to transport the atoms because part of the ceramic glue evaporates, thus removing the atoms from the optical dipole trap. The two-beam configuration might have been very useful in absence of the ceramic surface. For instance, the beams would not illuminate the ceramic surface if their direction of propagation were parallel to the direction of transport, which would require to place the translation stage beside the vacuum chamber instead of in front of it. The improvement of the two-beam configuration can be an interesting topic of study. However, the single-beam configuration has been proved efficient enough and for that reason it has been used for the work presented in this thesis.

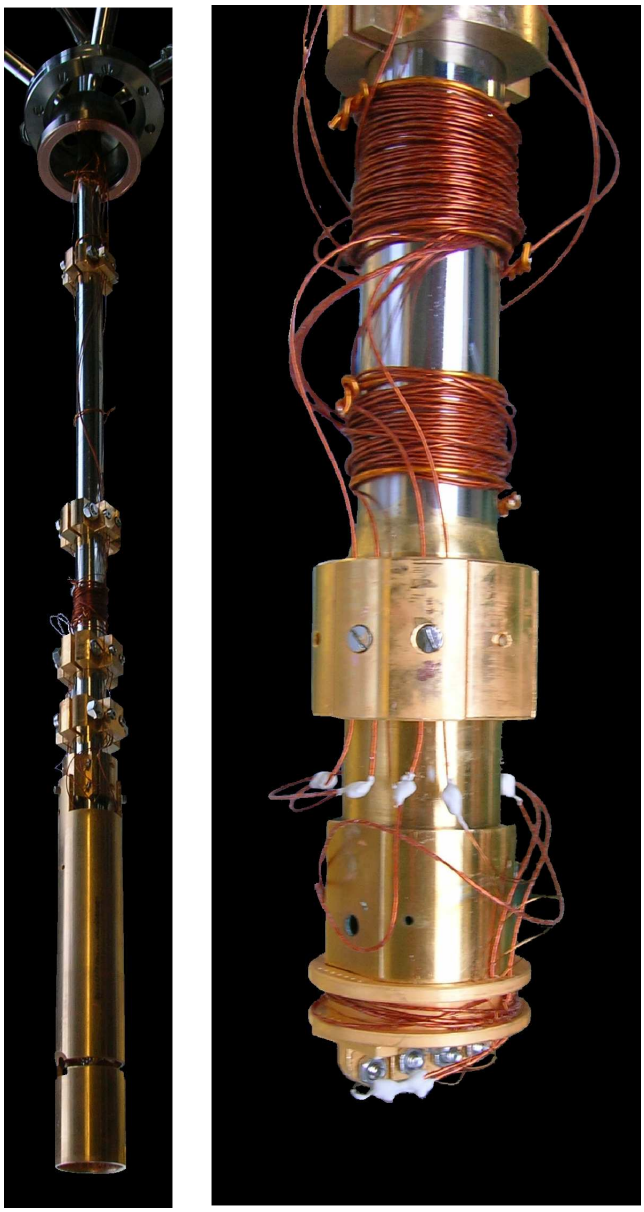

Figure 3.16: Flow cryostat. The superconducting microstructure is attached to the bottom surface. A radiation shield protects the microstructure from the room-temperature radiation. Electric currents are conducted to the microstrucutre by means of kapton-insulated wires. These kapton-insulated wires are cooled by means of wire holders that are firmly attached to the cryostat. The wire holders and the radiation shield are gold-platted in order to avoid oxide layers on the surface.

3.7 Helium flow cryostat

The superconducting microstructure is cryogenically cooled with the flow cryostat[7] shown in Figure 3.16. The cryostat is mounted in the UHV chamber with its cold end near the room-temperature trap setup, as shown in Figure 3.1. The superconducting microstructure is attached to the bottom surface of the cryostat. The employed coolant is liquid ^{4}He, the boiling point of which is 4.2 K. The liquid helium is stored in a 100-liter-volume dewar can from which it is continuously transferred to the cryostat by means of a vacuum-insulated transfer line. One end of the transfer line is inserted into the helium storage container, while the other end is inserted into the cryostat. Liquid helium flows from the storage container through the transfer line to the lower parts of the cryostat, where the liquid helium evaporates and cools the microstructure down to superconductivity temperatures. The helium gas escapes upwards, cooling the outer surface of the cryostat. The outer surface of the cryostat is a 1-meter long tube made of stainless steal, and its temperature varies gradually from 4.2 K in the lower parts to room temperature in the upper parts. Stable temperatures above 4.2 K can be also obtained with an electric resistor dissipating heat next to the microstructure. The dissipated heat is regulated with a temperature controller that measures the temperature of the microstructure and adjusts the applied power to maintain the desired temperature. The cryostat and all the used components are compatible with ultra high vacuum.

The electric currents applied to the microstructure are transferred through the walls of the vacuum chamber by means of some electrical feedthroughs located near the upper part of the cryostat. The currents are conducted through 0.25-mm-diameter kapton-insulated wires between the electrical feedthroughs and the microstructure. Unfortunately, the wires conduct not only electric current but also heat. There are two ways to reduce the transmitted heat. First, the wires are gradually cooled at different positions along the cryostat by means of wire holders that are firmly attached to the outer surface of the cryostat. Second, the thermal paths between the microstructure and the feedthroughs are increased by making the wires much longer than the cryostat. Hence the wires have to be wound around the cryostat as shown in Figure 3.16.

The lower parts of the cryostat are enclosed by a radiation shield that intercepts the room-temperature radiation, thus reducing the heat load on the sample. The radiation shield is a hollow cylinder made of OFHC copper. It is mounted to a thermal anchor on the cryostat surface, and reaches temperatures of about 20 K. The usage of optical tweezers to load the microtrap requires a small slit in the thermal radiation shield so that the focussed laser beam can transport the atomic cloud to the microtrap, while the radiation heat load is negligible. The radiation shield helps the sample to achieve lower temperatures.

Oxide has a very low thermal conductivity at cryogenic temperatures, and for that reason it has to be avoided from surfaces that need to be cryogenically cooled. For that

[7] Model ST-400, JANIS RESEARCH COMPANY

reason, all the copper pieces, such as the radiation shield and the wire holders, are gold-platted in order to prevent the copper surface from oxidation. This is accomplished by electro-chemical deposition in a gold cyanide bath at 60°C. Just before electro-chemical deposition, the oxide layers on the copper surface are removed with a special detergent[8].

The experimental system integrates the superconducting microtrap and the room-temperature trap setup in a single UHV chamber. In this way, ultracold atomic clouds can be easily transported from where they are produced into the superconducting microtrap by means of optical tweezers. Such an arrangement is simpler and more compact than the two experimental systems realized by other researchers [Nir06, Muk07], in which the atom cloud is transported between different chambers. Our apparatus is appropriate for trapping ultracold atoms in superconducting microstructures of arbitrary geometry.

[8] Aqueous solution with Tickopur RW 77.

Chapter 4

Realization and characterization of a superconducting microtrap

The experimental methods of loading atoms into superconducting microtraps and of measuring the Meissner effect have been developed using a superconducting microstructure with a simple design. This chapter presents the measurements realized with that superconducting microstructure as well as the theoretical analysis of the experimental results.

4.1 Superconducting microstructure to trap ultracold atoms

The central piece of the microstructure is a superconducting Nb wire with circular cross section of diameter 125 μm (Figure 4.1). The Nb wire is mechanically clamped between two copper plates by fastening four stainless-steal screws. The two copper plates are part of a larger piece that is firmly attached to the bottom surface of the cryostat. This ensures mechanical stability and good thermal contact. The whole copper piece was previously gold-plated in order to avoid oxide on its surface. The Nb wire is parallel to the z-axis. The realization of the microtrap requires to apply an electric current I_{Nb} to the Nb wire. Since the Nb wire is electrically not isolated from the copper piece, the applied current I_{Nb} will entirely flow along the Nb wire only if this has no electrical resistance. Therefore, no microtrap can form in the normal-conducting state. Transition to superconductivity is measured at $T_c = 9.2$ K with a four-point probe. In addition to the Nb wire, the microstructure has two offset wires parallel to the x-axis. The two offset wires are kapton insulated and 0.1-mm thick. The distance between them is 3 mm. They are located just above the Nb wire. The current applied to the offset wires is denoted by I_0.

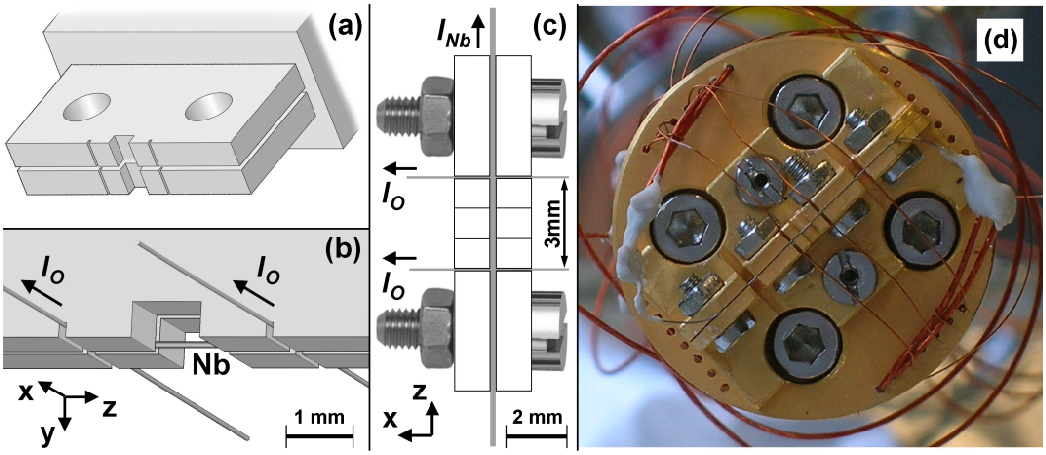

Figure 4.1: Superconducting microstructure. The Nb wire, with circular cross section of diameter 125 μm, is clamped in a slit of a gold-plated copper holder which is firmly attached to the bottom surface of the cryostat. Four screws and four nuts are used to clamp the Nb wire. It can be cooled to variable temperature down to 4.2 K. The trap is generated below the Nb wire by applying a current I_{Nb} and a bias field $\boldsymbol{B}_B$ in the x-direction. A small cut in the copper holder gives free access to the Nb wire at the central part of the superconducting microtrap. A pair of kapton-insulated offset wires along the x-direction, just above the Nb wire, are used for the axial confinement of the trap.

4.2 Superconducting Nb wire in a homogeneous magnetic field

In general, when a superconducting body is in the pure Meissner state, the intensities of induced or applied currents decay exponentially from the surface into the interior of the superconductor with a penetration depth λ, which is also the depth to which the magnetic field penetrates the superconductor. The pure Meissner state typically occurs well below the critical temperature, and describes the situation in which the superconductor is free of both vortices and normal-conducting domains. Well below the critical temperature the penetration depth of niobium is of the order of several tens of nanometers [Max65], depending on the degree of purity. This penetration depth is much shorter than the radius of the Nb wire, and therefore the Nb wire can be modeled as a perfectly diamagnetic cylinder, the radius R of which is the real radius of the Nb wire minus the penetration depth: $R = 62.5\ \mu\text{m} - \lambda \simeq 62.5\ \mu\text{m}$.

A case of special interest is the behavior of the superconducting wire when a homogeneous magnetic field is externally applied. The superconducting wire, which can be modeled as a very long diamagnetic cylinder, responds to the external magnetic field with a homogeneous magnetization $\boldsymbol{M}$ in the opposite direction. The external field remains homogeneous if it is parallel to the wire because the longitudinal demagnetizing factor of a cylinder quickly tends to zero as its length increases to infinity [Chi64]. On the other hand,

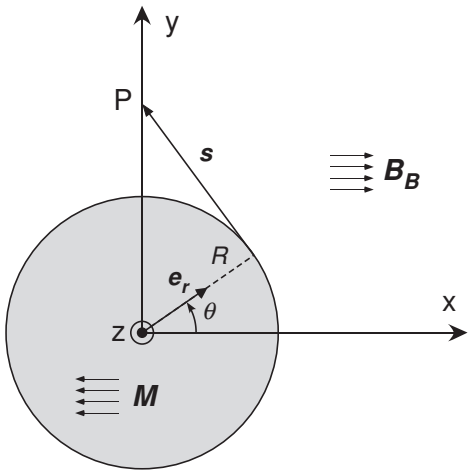

Figure 4.2: Cross section of the wire with the coordinate axes. When a homogeneous bias field $\boldsymbol{B}_B$ is applied, the superconducting wire responds with a homogeneous magnetization $\boldsymbol{M}$ in the opposite direction.

if the external field is perpendicular to the wire, the demagnetizing factor is $N = 1/2$, and the magnetization $\boldsymbol{M}$ distorts the magnetic field outside the wire.

The homogeneous magnetic field is called homogeneous bias field when it is perpendicular to the Nb wire. The bias field is denoted by $\boldsymbol{B}_B$. The coordinate axes are defined as represented in Figure 4.2. The Nb wire is parallel to the z-axis, and $\boldsymbol{B}_B$ is parallel to the x-axis. The magnetic field $\boldsymbol{B}_M$ generated by $\boldsymbol{M}$ is calculated as [Jac67]

$$\boldsymbol{B}_M = \mu_0(1 - N)\boldsymbol{M}. \tag{4.1}$$

The condition of perfect diamagnetism implies that $\boldsymbol{B}_B = -\boldsymbol{B}_M$ in the interior of the cylinder. From this equality relation, one can derive the following expression for the magnetization:

$$\boldsymbol{M} = -2\frac{\boldsymbol{B}_B}{\mu_0}. \tag{4.2}$$

This homogeneous magnetization generates a surface current density $\boldsymbol{K} = \boldsymbol{M} \times \boldsymbol{e}_r = -|\boldsymbol{M}| \sin\theta\ \boldsymbol{e}_z$, where $\boldsymbol{e}_r = (\cos\theta, \sin\theta, 0)$ is the unit vector in the radial direction, $\boldsymbol{e}_z$ is the unit vector in the z-direction, and θ is the angular coordinate (see Figure 4.2). Let us now consider the infinitesimal current element $\mathrm{d}I\ \boldsymbol{e}_z = \boldsymbol{K}\ R\ \mathrm{d}\theta$ at the angular coordinate θ. Let us also consider a point P on the y-axis outside the superconducting wire. The magnetic field generated at P by the current element is calculated as

$$\begin{aligned} \mathrm{d}\boldsymbol{B}_M &= \frac{\mu_0}{2\pi}\left(\frac{\boldsymbol{K}}{|\boldsymbol{s}|} \times \frac{\boldsymbol{s}}{|\boldsymbol{s}|}\right) R\ \mathrm{d}\theta = -\frac{\mu_0}{2\pi}\ \frac{|\boldsymbol{M}|\ \sin\theta}{|\boldsymbol{s}|^2}\ (\boldsymbol{e}_z \times \boldsymbol{s})\ R\ \mathrm{d}\theta \\ &= \frac{\mu_0}{2\pi}\ \frac{|\boldsymbol{M}|\ \sin\theta}{|\boldsymbol{s}|^2}\ [(y - R\sin\theta)\ \boldsymbol{e}_x + R\cos\theta\ \boldsymbol{e}_y]\ R\ \mathrm{d}\theta. \end{aligned} \tag{4.3}$$

The integral of this function as θ varies over the interval $[0, 2\pi]$ is the magnetic field generated by the whole surface current $\boldsymbol{K}$:

$$\boldsymbol{B}_M = |\boldsymbol{B}_B| \frac{R^2}{y^2}\, \boldsymbol{e}_x. \tag{4.4}$$

The total magnetic field, $\boldsymbol{B}_B + \boldsymbol{B}_M$, outside the superconductor on the y-axis is $|\boldsymbol{B}_B|(1 + R^2/y^2)\ \boldsymbol{e}_x$. Therefore, the distortion of the bias field is strong near the superconducting wire.

4.3 The trapping potential

A two-dimensional confining magnetic field $\boldsymbol{B}_{2D}$ (magnetic guide) is created by combination of the circular magnetic field of I_{Nb}, which is denoted by $\boldsymbol{B}_{Nb}$, and a homogeneous bias field $\boldsymbol{B}_B$ parallel to the x-axis. The directions of the axes are indicated in Figures 4.1 and 4.2. The origin of coordinates is located at the center of the Nb wire. The bias field is generated by two Helmholz coils outside the vacuum chamber. The atoms are radially confined around the positions where $\boldsymbol{B}_B$ cancels $\boldsymbol{B}_{Nb}$. The magnetic guide forms around a straight line that is parallel to the Nb wire and that is included in the plane $x = 0$. Following the same notation as in Chapter 2, the distance between the magnetic guide and the wire center is denoted by y_0, and the magnetic-field gradient near the guide center is denoted as a. In general, a and y_0 depend on both the geometry and the state of the wires. The symbols describing the trap parameters will have an additional subindex, SC or NC, when they are referred to the superconducting or the normal-conducting state, respectively.

Figure 4.3 shows the magnetic profiles in a theoretical example of microtrap calculated for both the superconducting and the normal-conducting cases. In the normal-conducting case, the applied current I_{Nb} is homogeneously distributed within the wire, and the modulus of $\boldsymbol{B}_{Nb}$ in the y-axis can be calculated as

$$|\boldsymbol{B}_{Nb}| = \frac{\mu_0}{2\pi} \frac{I_{Nb}}{y}, \tag{4.5}$$

where y is the distance to the wire center. The homogeneous bias field $\boldsymbol{B}_B$ penetrates the conductive wire. Then, the magnetic guide forms at the position

$$y_{0,NC} = \frac{\mu_0}{2\pi} \frac{I_{Nb}}{B_B}. \tag{4.6}$$

The magnetic-field gradient in the radial directions around $y_{0,NC}$ is

$$a_{NC} = \frac{B_B}{y_{0,NC}}. \tag{4.7}$$

The trap parameters for the superconducting case are calculated by approximating the Nb wire to a diamagnetic cylinder. In the superconducting wire, the applied current

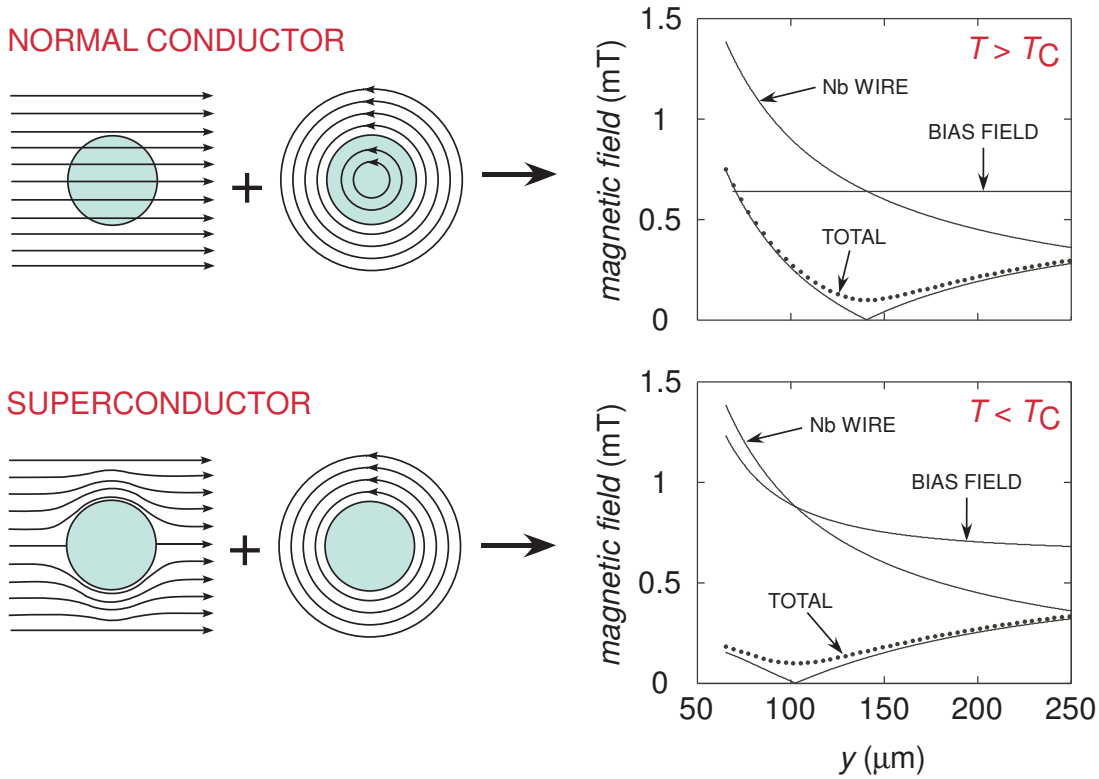

Figure 4.3: Impact of the Meissner effect on the magnetic microtrap generated near a superconducting Nb wire with circular cross section of radius 62.5 μm. The Nb wire is in the pure Meissner state. The microtrap is created by combination of the homogeneous bias field $\boldsymbol{B}_B = 0.64$ mT and the magnetic field $\boldsymbol{B}_{Nb}$ of the applied current $I_{Nb} = 0.45$ A. The realization of the microtrap requires that the bias field is opposite in direction to $\boldsymbol{B}_{Nb}$. An additional offset field of 10^{-4} T along the z-direction changes the magnetic profile from linear to parabolic (dotted curve).

I_{Nb} flows only in a thin layer near the surface. Because the wire is axially symmetric, the Stokes theorem can be easily used with any mathematical cylindrical surface that is concentric with the wire. The Stokes theorem implies that the magnetic field generated by I_{Nb} outside the superconductor is exactly the same as if the wire were normal conducting (Equation 4.5). However, the bias field is strongly affected by the Meissner effect near the superconducting wire. Below the critical temperature, the bias field calculated along the y-axis becomes $|\boldsymbol{B}_B|(1 + R^2/y^2)\ \boldsymbol{e}_x$, as deduced in the previous section. In the superconducting case, the magnetic guide forms at the position

$$y_{0,SC} = \frac{\mu_0}{4\pi}\frac{I_{Nb}}{B_B} + \sqrt{\left(\frac{\mu_0}{4\pi}\frac{I_{Nb}}{B_B}\right)^2 - R^2}, \tag{4.8}$$

and the magnetic-field gradient in the radial directions at $y_{0,SC}$ is

$$a_{SC} = \frac{B_B}{y_{0,SC}}\left(1 - \left(\frac{R}{y_{0,SC}}\right)^2\right). \tag{4.9}$$

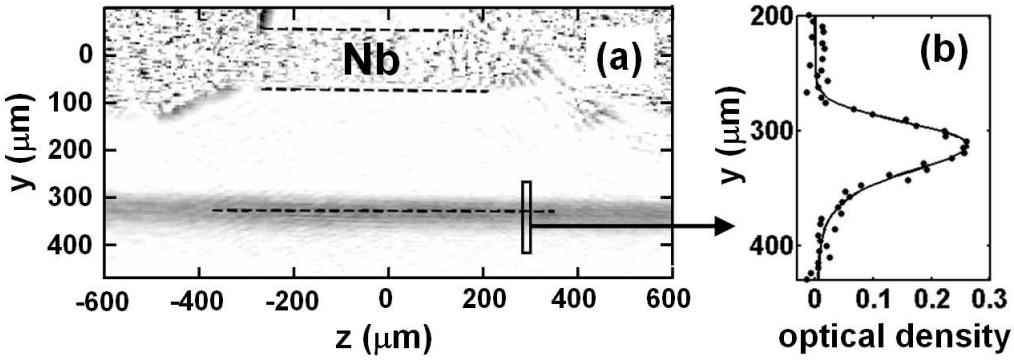

Figure 4.4: (a) Image of the atomic optical density at the central region of the magnetic trap. The dashed lines represent the longitudinal axis of the trap, and the Nb wire surface. (b) Optical density of one of the transverse sections of the atomic cloud. The best-fit curve $\rho(y)$ is also plotted.

This model demonstrates that the Meissner effect shortens the distance between the trap and the wire, reduces the radial magnetic-field gradients and lowers the trap depth.

Longitudinal confinement in the z-direction is achieved by means of the two offset currents I_0. The value of I_0 is 0.01 A during all the experiments. Because of the low value of I_0 and because of the long distance between the two offset wires, the longitudinal confinement at the trap center is very weak and does not alter the values of the trap parameters, y_0 and a, described in the previous paragraphs. This weak longitudinal confinement can still trap enough atoms for the experiment. A complete theoretical description of the longitudinal confining potential generated by two offset wires was given in Chapter 2, although such a detailed analysis is not necessary here.

4.4 Loading the atoms into the superconducting microtrap

The atoms are loaded from the optical tweezers into the superconducting microtrap at a distance of 500 μm from the Nb wire. This is accomplished by ramping up the magnetic fields of the microtrap within 100 ms, and subsequently ramping down the laser power to zero in 0.5 s. Typical values for loading the atoms are $|\boldsymbol{B}_B| = 0.64$ mT, $I_{Nb} = 1.6$ A, $I_0 = 0.01$ A and $|\boldsymbol{B}_0| = 0.1$ mT, which produce trap frequencies of $\omega_r = 2\pi \cdot 160$ s^{-1} and $\omega_l = 2\pi \cdot 2$ s^{-1}. The microtrap is loaded with $4 \cdot 10^5$ atoms at 5 μK. After loading, the atoms are brought close to the Nb wire by reducing I_{Nb}. The positioning of the cloud is accomplished within 0.5 s, which is adiabatic with respect to the motion of atoms inside the trap. Finally, the atom cloud is imaged.

4.5 Determining the trap position from the atom density

The atomic optical density in the central region of the magnetic trap is shown in Figure 4.4(a). The magnetic trap is very elongated due to the week longitudinal confinement near its center. For every image, y_0 is calculated as the distance between the longitudinal axis of the trap and the longitudinal axis of the Nb wire. In order to compute the longitudinal axis of the trap accurately, the atom cloud is divided in transverse sections. For every transverse section, the measured atom density is fitted to the theoretical density profile $\rho(y)$, as illustrated in Figure 4.4(b). The maxima of $\rho(y)$ of all transverse sections of the same atomic cloud are fitted to a straight line, which is the longitudinal axis of the trap.

The function $\rho(y)$ is defined so that its value at the center of a given pixel is the convolution of the theoretical density of atoms and the point-spread function (PSF) of the detection system, integrated across the pixel area, and integrated along the direction of the detection beam. The PSF of the detection system is computed as a gaussian approximation of the two-dimensional Airy function, the width of which is determined by the diffraction-limited resolution (see Section 3.4).

The theoretical density of atoms is $A \exp\left(U(y,x)/(K_B T)\right.$, where K_B is the Bolztmann constant, T is the cloud temperature and $U(y,x)$ is the potential energy. The potential energy $U(y,x)$ includes both the magnetic term (Equation 2.18) and the gravitational term:

$$U(y,x) = g_F \mu_B m_F |\boldsymbol{B}_{2D}| - mgy, \tag{4.10}$$

The asymmetry of the atom density profile observed in Figure 4.4(b) is due to the decrease in magnetic gradient with increasing y and, to a lesser extent, to gravity. The decrease in magnetic field gradient with increasing y is not represented in the linear approximation of Equation 2.20, which is valid only in the vicinity of the trap center. To include this asymmetry in the potential $U(y,x)$, a second-order term, $b(y-y_0)^2/2$, is added to the x-coordinate of the magnetic field $\boldsymbol{B}_{2D}$ in Equation 2.20. Then, the variables of the fitting procedure are T, a, b, y_0 and A. The fitting procedure is very accurate to obtain the maximum of the atom density for every transversal section. However, the best-fit values of T, a and b cannot be consider as good measurements of the corresponding quantities. The purpose of this fitting procedure is only to determine accurately the position y_0 of the atom cloud.

A similar numerical technique is used to obtain the positions of the wire surface, and thus the longitudinal axis of the wire. In this case, every transverse section of the Nb wire in the absorption image is fitted to the following function: $1 \pm A_1 \ \mathrm{Erf}((y-A_2)/A_3)$, where A_1, A_2 and A_3 are the variables of the fit. By definition, the error function Erf is twice the integral of a Gaussian distribution. Because the PSF of the detection system can be approximated to a two-dimensional gaussian distribution, the mentioned function can be used to represent the diffraction-limited image of a sharp profile like the edge of the wire. The sign used in this formula depends on whether the upper or lower edge of the Nb wire

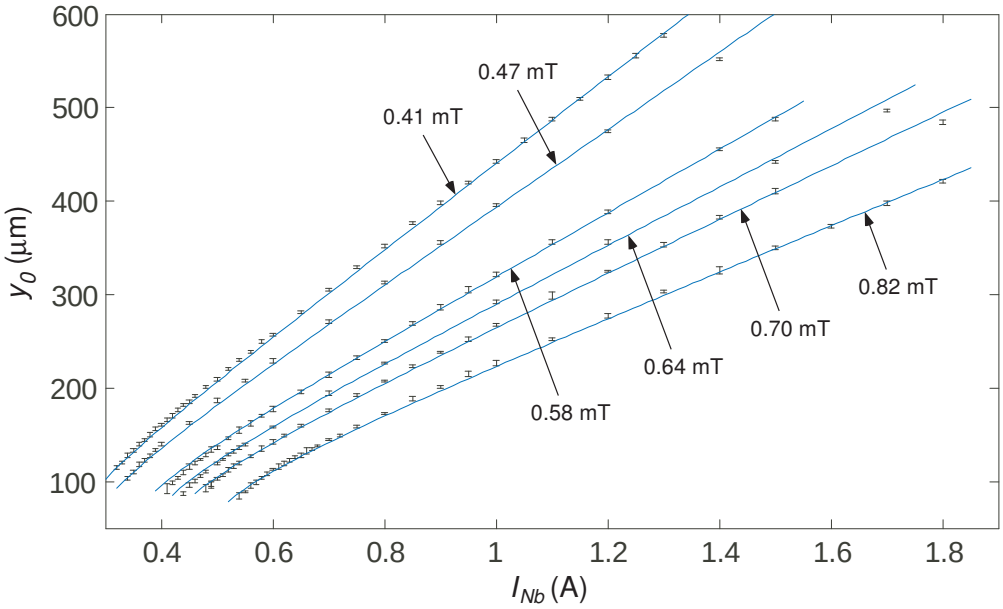

Figure 4.5: Distance between the magnetic trap and the wire center as a function of the applied current I_{Nb} for six different values of the bias field: 0.41, 0.47, 0.58, 0.64, 0.70 and 0.82 mT. The measured points and the best-fit curves are plotted together. The slope of the curves increases near the wire as a consequence of the Meissner effect. The error bars of the measured points, which are almost indistinguishable, represent the error of the fitting procedure described in Figure 4.4.

is considered.

4.6 Observation of the Meissner effect in the superconducting microtrap

By monitoring the position of the atomic cloud, we observe how the Meissner effect influences the magnetic microtrap. Figure 4.5 shows the measured positions as a function of I_{Nb} for six different bias fields. Experimental data are fitted by six curves -each curve corresponds to a bias field- that are calculated using the theoretical model explained in Section 4.3. Far from the superconducting wire, the represented curves are very similar to those expected for a normal-conducting wire. A normal-conducting wire would produce straight lines, slightly altered by gravity, that intersect the wire center. The impact of the Meissner effect is visible at short distances from the wire, where the slope of the curves increases as I_{Nb} decreases. As predicted by the theoretical model, the Meissner effect shortens the distance between the microtrap and the wire in the vicinity of the superconducting surface.

Both gravity and misalignments of the applied bias field produce a small shift in the

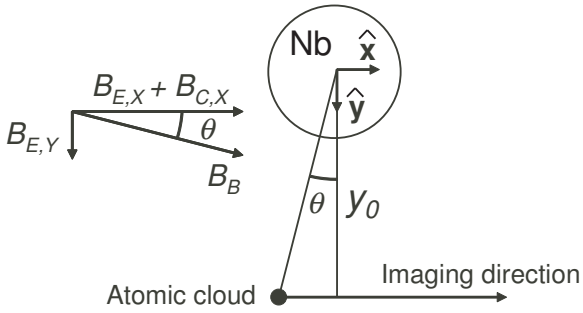

Figure 4.6: Representation of the effect of stray homogeneous fields on the trap position. The observed distance y_0 between the trap and the wire center is the projection of the real distance onto the y-axis.

position of the atomic cloud. These effects have been taken into account in the numerical procedure used to find the best-fit curves of Figure 4.5. The way to include these effects in the numerical procedure is explained below.

The homogeneous bias field is generated by two Helmholz coils installed outside the chamber. The current applied to these coils is denoted by I_C. The geometry of the apparatus makes it difficult to distinguish between the x- and the z-axes of the microtrap when looking from outside the chamber. Aligning the axis of the external coils to the x-axis of the microtrap is therefore not an easy task. That is the reason why the external coils produce a field component also along the z-direction. The field generated by the two external coils is denoted by $\boldsymbol{B}_C = (\eta_X I_C, 0, \eta_Z I_C)$, where η_X and η_Z are constants that need to be measured. Additionally, the magnetic field of the Earth as well as some near electronic systems can contribute to the homogeneous field at the microtrap. These spurious external fields are denoted by $\boldsymbol{B}_E = (B_{E,X}, B_{E,Y}, B_{E,Z})$.

The total bias field $\boldsymbol{B}_B = (\eta_X I_C + B_{E,X}, B_{E,Y}, 0)$ forms an angle θ with the imaging direction (see Figure 4.6). The cosine of this angle is

$$\cos\theta = \frac{B_{E,X} + \eta_X I_C}{\sqrt{(B_{E,X} + \eta_X I_C)^2 + (B_{E,Y})^2}}. \tag{4.11}$$

As a consequence, the observed distance between the atom cloud and the wire is slightly different from the function $y_{0,SC}$ (Equation 4.8). Instead, the observed position is described by the function $y_{0,SC}\ \cos\theta + \Delta_{SC}$, which takes account of misalignments of the external coils, spurious magnetic fields and gravity. The explicit expression of this function is obtained from Equations 2.23, 4.8 and 4.11. This is the function used to fit the 160 experimental points of Figure 4.5.

The offset field in the z-direction is $B_0[\mathrm{T}] = B_{E,Z} + \eta_Z I_C = 11.6{\cdot}10^{-6} I_C[\mathrm{A}] + 20.1{\cdot}10^{-6}$. It has been obtained experimentally from the radiofrequencies that remove the trapped atoms. This longitudinal field changes the radial confinement from linear to harmonic, making the trap position sensitive to gravity.

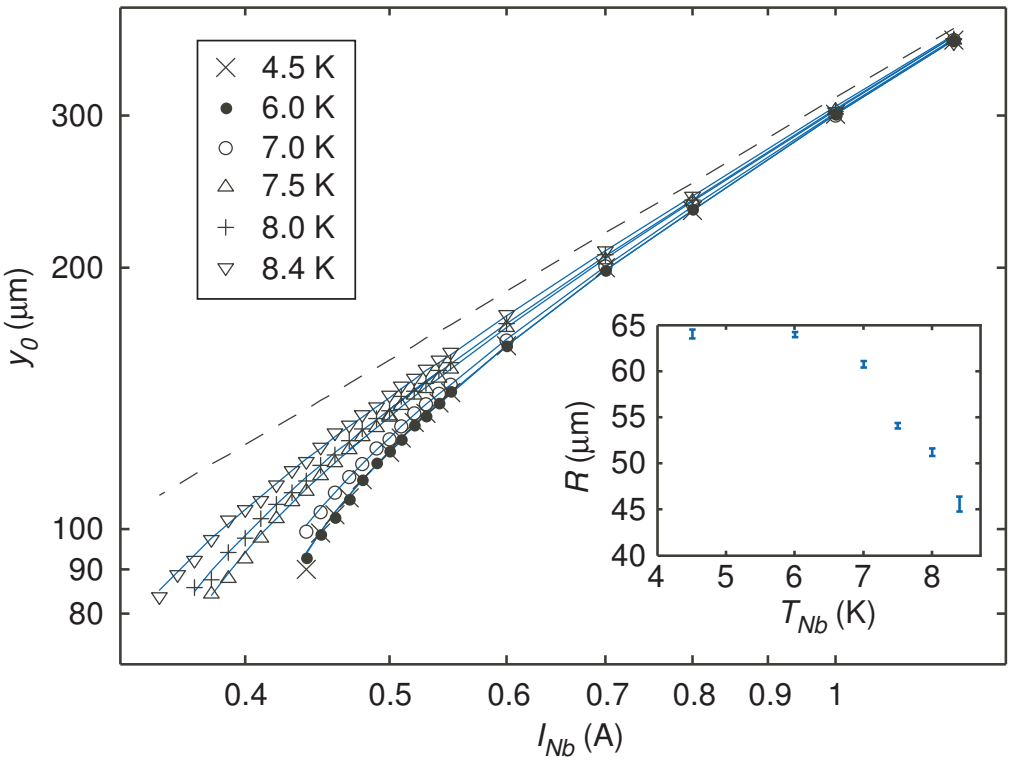

Figure 4.7: Distance between the trap center and the wire center as a function of the applied current I_{Nb} for six different temperatures of the Nb wire. $|\boldsymbol{B}_B| = 0.64$ mT and $B_0 = 10^{-4}$ T. The normal-conducting case is represented as a dashed curve. The error bars, which result from the fitting procedure illustrated in Figure 4.4, are smaller than the symbols and therefore not represented. The inset shows the best-fit radius as a function of T_{Nb}. The error bars represent the 95%-confidence interval.

The total bias field $\boldsymbol{B}_B = (\eta_X I_C + B_{E,X}, B_{E,Y}, 0)$ is obtained from the best-fit variables. The best-fit variables are: $R = 61.5 \pm 1.1\mu$m, $\eta_X = (1.23 \pm 0.03) \cdot 10^{-4}$ T, $B_{E,X} = (-1.8 \pm 0.3) \cdot 10^{-4}$ T and $B_{E,Y} = (1.8 \pm 0.1) \cdot 10^{-4}$ T. The good agreement of the best-fit radius R with the real radius of the wire validate the model described above.

The gravitational sag Δ_{SC} and the misalignment of the bias field are relatively small and hardly affect the best-fit radius R. Even so, they have been considered in the fitting procedure with the aim of reducing the error of the obtained best-fit variables.

4.7 Dependence of the microtrap parameters on the Nb wire temperature

A clearer evidence of the impact of the Meissner effect is given by Figure 4.7, which shows the dependence of the microtrap position on the wire temperature during the transition phases between the pure Meissner state and the normal state. These transition phases

usually consist of continuous processes involving increase of λ, normal-conducting domains and vortices that let the magnetic flux penetrate partially the superconductor [Ket99, Tin75]. The partial penetration of the magnetic field into the Nb wire is manifested in a shift of the microtrap towards the positions calculated for a the normal-conducting state.

The theoretical model based on a perfectly diamagnetic cylinder can be used not only for the pure Meissner state, but also for the transition phases from the pure Meissner state to the normal state. The partial penetration of the magnetic field can be modeled as a reduction of the effective radius R of the diamagnetic cylinder. Then, the effective radius R of the Nb wire becomes a temperature-dependent variable.

Figure 4.7 shows the measured positions of the atomic cloud as a function of I_{Nb} for six different wire temperatures T_{Nb}, keeping the bias field at a constant value of 0.64 mT. Experimental data are represented in logarithmic scale to give more visibility to the points that are closer to the wire. For comparison, the microtrap positions calculated for the normal-conducting state are represented as a dashed curve, which is a straight line slightly distorted by gravity. The dependence of y_0 on T_{Nb} is noticeable only at the lowest values of y_0, where the impact of the Meissner effect is stronger. For every temperature, the measured points are fitted by the function $y_{0,SC}\ \cos\theta + \Delta_{SC}$. Because the bias field and the offset field have been already determined in the previous section, the effective radius R is the only variable of the fitting procedure. For every temperature, the best-fit curve is obtained by varying the effective radius R. The inset of figure 4.7 plots the best-fit radius R versus T_{Nb}.

For temperatures lower than 6K, the best-fit radius R is very similar to the real radius of the wire. This is the expected value at such low temperatures, when the wire is in the pure Meissner state [Lon50]. As T_{Nb} increases, the microtrap positions are shifted towards the positions expected for a normal-conducting wire. This is caused by an increase in the amount of magnetic flux penetrating the wire, which is manifested as a decrease of the effective radius R. The fact that the increase in temperature does not affect the points that are far from the wire demonstrates that the electric resistance remains zero, and so the applied current I_{Nb} flows entirely through the Nb wire. The experimental data reveal a smooth transition from the pure Meissner state to the normal state. For temperatures above 8.4 K, the atoms cannot be loaded into the microtrap because the critical current of the Nb wire drops below 1.6 A, which is the current I_{Nb} required to load the microtrap.

For every temperature, the root-mean-square of the difference between the measured points and the best-fit curve is lower than 2 μm, which demonstrates that the magnetic field outside the Nb wire can be well described by formulas relying on a diamagnetic cylinder. Even though transition from Meissner state to normal state usually consists of complex processes involving vortex formation, penetration-depth increase and normal-conducting domains, the magnetic field outside the wire can be well described with a simple model based on a diamagnetic cylinder of temperature-dependent, effective radius R.

The superconducting microstructure used in this experiment has enabled us to inves-

tigate the Meissner effect in the Nb wire as well as its impact on the superconducting microtrap. The observation of this fundamental property of superconductors is a groundbreaking achievement in the field of superconducting microtrap.

Chapter 5

Conclusions

This thesis has evaluated the impact of the Meissner effect on magnetic potentials for ultracold quantum gases near superconducting microstructures. Both computer simulations and experimental measurements demonstrate that the Meissner effect induces important changes in magnetic microtraps. The Meissner effect shortens the distance between the trapped atoms and the superconducting surface, reduces the magnetic-field gradients and lowers the trap depth. The fact that this tendency is followed by both thin films with rectangular cross section and wires with circular cross section suggests that it does not depend on the particular geometry of the superconductor.

The results of this study will have important implications for experiments with quantum gases near superconducting surfaces. Atom chips with superconducting microstructures are expected to provide intriguing physical scenarios in which atomic physics and superconductor science converge. However, the success of such devices will rely on the proper considerations of the electromagnetic properties of superconductors. The impact of the Meissner effect on the magnetic potentials has to be taken into account when designing experiments with ultracold quantum gases near superconducting surfaces.

The research techniques developed in this thesis provide appropriate conditions for investigating fundamental interactions between cold atoms and superconducting surfaces. Magnetic potentials on superconducting atom chips can be accurately designed with the numerical routine explained in Chapter 2, and the realized atom chips can be loaded with ultracold atoms in the experimental system shown in Chapters 3 and 4. Future research topics of particular interest include the change in the spin-coherence time during the transition from the normal to the superconducting state, Casimir-Polder forces between atoms and the cold surface, and the interaction between atoms and superconducting-vortex lattices. Furthermore, applications of this field of research will probably include hybrid quantum systems such as ultracold atoms coupled to Josephson junctions or SQUIDs.

Bibliography

[Abo01] J. R. Abo-Shaeer, C. Raman, J. M. Vogels, W. Ketterle, *Observation of Vortex Lattices in Bose-Einstein Condensates*, Science **292**, 476 (2001)

[And95] M. H. Anderson, J. R. Ensher, M. R. Matthews, C. E. Wieman, and E. A. Cornell, *Observation of Bose-Einstein Condensation in a Dilute Atomic Vapor*, Science **269**, 198 (1995).

[And957] M. R. Andrews, C. G. Townsend, H.-J. Miesner, D. S. Durfee, D. M. Kurn, and W. Ketterle, *Observation of Interference Between Two Bose Condensates*, Science **275**, 637 (1997).

[Arf95] G. B. Arfken and H. J. Weber, *Mathematical methods for physicists*, (Academic Press, Inc., 1995).

[Asp88] A. Aspect, E. Arimondo, R. Kaiser, N. Vansteenkiste, and C. Cohen-Tannoudji, *Laser Cooling below the One-Photon Recoil Energy by Velocity-Selective Coherent Population Trapping*, Physical Review Letters **61**, 826 (1988).

[Bar04] M. Bartenstein, A. Altmeyer, S. Riedl, S. Jochim, C. Chin, J. Hecker Denschlag, and R. Grimm, *Crossover from a Molecular Bose-Einstein Condensate to a Degenerate Fermi Gas*, Physical Review Letters **92**, 120401 (2004)

[Bou04] T. Bourdel, L. Khaykovich, J. Cubizolles, J. Zhang, F. Chevy, M. Teichmann, L. Tarruell, S. J. J. M. F. Kokkelmans, and C. Salomon, *Experimental Study of the BEC-BCS Crossover Region in Lithium 6*, Physical Review Letters **93**, 050401 (2004).

[Bra95] C. C. Bradley, C. A. Sackett, J. J. Tollett, and R. G. Hulet, *Evidence of Bose-Einstein Condensation in an Atomic Gas with Attractive Interactions*, Physical Review Letters **75**, 1687 (1995). Erratum: Physical Review Letters **79**, 1170 (1997).

[Bra00] E. H. Brandt, and G. P. Mikitik, *Meissner-London Currents in Superconductors with Rectangular Cross Section*, Physical Review Letters **85**, 4164 (2000).

[Bur99] S. Burger, K. Bongs, S. Dettmer, W. Ertmer, K. Sengstock, A. Sanpera, G. V. Shlyapnikov, and M. Lewenstein, *Dark Solitons in Bose-Einstein Condensates*, Physical Review Letters **83**, 5198 (1999).

[Can08a] D. Cano, B. Kasch, H. Hattermann, D. Koelle, R. Kleiner, C. Zimmermann, and J. Fortágh, *Impact of the Meissner effect on magnetic microtraps for neutral atoms near superconducting thin films*, Physical Review A **77**, 063408 (2008).

[Can08b] D. Cano, B. Kasch, H. Hattermann, R. Kleiner, C. Zimmermann, D. Koelle, and J. Fortágh, *Meissner effect in superconducting microtraps*, Physical Review Letters **101**, 183006 (2008).

[Cas00] D. Cassettari, B. Hessmo, R. Folman, T. Maier, and J. Schmiedmayer, *Beam Splitter for Guided Atoms*, Physical Review Letters **85**, 5483 (2000).

[Cas96] Y. Castin and R. Dum, *Bose-Einstein Condensates in Time Dependent Traps*, Physical Review Letters **77**, 5315 (1996).

[Chi64] S. Chikazumi, *Physics of Magnetism*, (John Wiley & Sons, Inc., 1964).

[Chi04] C. Chin, M. Bartenstein, A. Altmeyer, S. Riedl, S. Jochim, J. Hecker Denschlag, and R. Grimm, *Observation of the Pairing Gap in a Strongly Interacting Fermi Gas*, Science **305**, 1128 (2004).

[Cor02] R. A. Cornelussen, A. H. van Amerongen, B. T. Wolschrijn, R. J. C. Spreeuw, and H. B. van Linden van den Heuvell, *Cold trapped atoms detected with evanescent waves*, European Physical Journal D: Molecular, Optical and Plasma Physics **21**, 347 (2002).

[Dal99] F. Dalfovo and S. Giorgini, *Theory of Bose-Einstein condensation in trapped gases*, Reviews of Modern Physics **71**, 463 (1999).

[Dal89] J. Dalibard and C. Cohen-Tannoudji, *Laser cooling below the Doppler limit by polarization gradients: simple theoretical models*, Journal of the Optical Society of America **6** 2023 (1989).

[Dav95] K. B. Davis, M.-O. Mewes, M. R. Andrews, N. J. van Druten, D. S. Durfee, D. M. Kurn, and W. Ketterle, *Bose-Einstein Condensation in a Gas of Sodium Atoms*, Physical Review Letters **75**, 3969 (1995).

[DeM99] B. DeMarco and D. S. Jin, *Onset of Fermi Degeneracy in a Trapped Atomic Gas*, Science **285**, 1703 (1999).

[Den98] J. Denschlag, G. Umshaus, and J. Schmiedmayer, *Probing a Singular Potential with Cold Atoms: A Neutral Atom and a Charged Wire*, Physical Review Letters **81**, 737 (1998).

[Den99] J. Denschlag, D. Cassettari, and J. Schmiedmayer, *Guiding Neutral Atoms with a Wire*, Physical Review Letters **82**, 2014 (1999).

[Den00] J. Denschlag, J. E. Simsarian, D. L. Feder, Charles W. Clark, L. A. Collins, J. Cubizolles, L. Deng, E. W. Hagley, K. Helmerson, W. P. Reinhardt, S. L. Rolston, B. I. Schneider, and W. D. Phillips, *Generating Solitons by Phase Engineering of a Bose-Einstein Condensate*, Science **287**, 97 (2000).

[Drn99] M. Drndiċ, G. Zabow, C. S. Lee, J. H. Thywissen, K. S. Johnson, M. Prentiss, R. M. Westervelt, P. D. Featonby, V. Savalli, L. Cognet, K. Helmerson, N. Westbrook, C. I. Westbrook, W. D. Phillips, and A. Aspect, *Properties of microelectromagnet mirrors as reflectors of cold Rb atoms*, Physical Review A **60**, 4012 (1999).

[Dum02] R. Dumke, M. Volk, T. Müther, F. B. J. Buchkremer, G. Birkl, and W. Ertmer, *Micro-optical realization of arrays of selectively addressable dipole traps: A scalable configuration for quantum computation with atomic qubits*, Physical Review Letters **89**, 097903 (2002).

[Ens96] J. R. Ensher, D. S. Jin, M. R. Matthews, C. E. Wieman, and E. A. Cornell, *Bose-Einstein Condensation in a Dilute Gas: Measurement of Energy and Ground-State Occupation*, Physical Review Letters **77**, 4984 (1996).

[Est05] J. Estève, T. Schumm, J.-B. Trebbia, I. Bouchoule, and A. Aspect, *Realizing a stable double-well potential on an atom chip*, The European Physical Journal D: Atomic, Molecular, Optical and Plasma Physics **35**, 141 (2005).

[Fol02] R. Folman, P. Krüger, J. Denschlag, C. Henkel, and J. Schmiedmayer, *Microscopic atom optics: From wires to an atom chip*, Advances in Atomic, Molecular, and Optical Physics **48**, 263 (2002).

[For07] J. Fortágh and C. Zimmermann, *Magnetic microtraps for ultracold atoms*, Reviews of Modern Physics **79**, 235 (2007).

[For98] J. Fortágh, A. Grossmann, and C. Zimmermann, *Miniaturized Wire Trap for Neutral Atoms*, Physical Review Letters **81**, 5310 (1998).

[Gre02] M. Greiner, O. Mandel, T. Esslinger, T. W. Hänsch and I. Bloch, *Quantum phase transition from a superfluid to a Mott insulator in a gas of ultracold atoms*, Nature **415**, 44 (2002).

[Gri00] R. Grimm, M. Weidemüller, and Yu.B. Ovchinnikov, *Optical dipole traps for neutral atoms*, Advances in Atomic, Molecular, and Optical Physics **42**, 95 (2000).

[Gro46] F. W. Grover, *Inductance Calculations*, (D. Van Nostrand Company, Inc., New York, 1946), Chap. 2&5.

[Gun05] A. Günther, M. Kemmler, S. Kraft, C. J. Vale, C. Zimmermann, and J. Fortágh, *Combined chips for atom-optics*, Physical Review A **71**, 063619 (2005).

[Gun07] A. Günther, S. Kraft, C. Zimmermann, and J. Fortágh, *Atom Interferometer Based on Phase Coherent Splitting of Bose-Einstein Condensates with an Integrated Magnetic Grating*, Physical Review Letters **98**, 140403 (2007).

[Gus02] T. L. Gustavson, A. P. Chikkatur, A. E. Leanhardt, A. Görlitz, S. Gupta, D. E. Pritchard, and W. Ketterle, *Transport of Bose-Einstein Condensates with Optical Tweezers*, Physical Review Letters **88**, 020401 (2002).

[Hal06] B. V. Hall, S. Whitlock, F. Scharnberg, P. Hannaford and A. Sidorov, *A permanent magnetic film atom chip for Bose-Einstein condensation*, Journal of Physics B: Atomic, Molecular and Optical Physics **39**, 27 (2006).

[Ham03] M. Hammes, D. Rychtarik, B. Engeser, H.-C. Nägerl, and R. Grimm, *Evanescent-Wave Trapping and Evaporative Cooling of an Atomic Gas at the Crossover to Two Dimensions*, Physical Review Letters **90**, 173001 (2003).

[Han01] W. Hänsel, J. Reichel, P. Hommelhoff, and T. W. Hänsch, *Magnetic conveyor belt for transporting and merging trapped atom clouds*, Physical Review Letters **86**, 608 (2001).

[Har03] D. M. Harber, J. M. McGuirk, J. M. Obrecht, and E. A. Cornell, *Thermally Induced Losses in Ultra-Cold Atoms Magnetically Trapped Near Room-Temperature Surfaces*, Journal of Low Temperature Physics **133**, 229 (2003).

[Har05] D. M. Harber, J. M. Obrecht, J. M. McGuirk, and E. A. Cornell, *Measurement of the Casimir-Polder force through center-of-mass oscillations of a Bose-Einstein condensate*, Physical Review A **72**, 033610 (2005).

[Hoh07] U. Hohenester, A. Eiguren, S. Scheel, and E. A. Hinds, *Spin-flip lifetimes in superconducting atom chips: Bardeen-Cooper-Schrieffer versus Eliashberg theory*, Physical Review A **76**, 033618 (2007).

[Ino98] S. Inouye, M. R. Andrews, J. Stenger, H.-J. Miesner, D. M. Stamper-Kurn, and W. Ketterle, *Observation of Feshbach resonances in a Bose-Einstein condensate*, Nature **392**, 151 (1998).

[Jac67] J. D. Jackson, *Classical Electrodynamics*, (John Wiley & Sons, Inc., 1967), Chap. 5.

[Jon03] M. P. A. Jones, C. J. Vale, D. Sahagun, B. V. Hall, and E. A. Hinds, *Spin Coupling between Cold Atoms and the Thermal Fluctuations of a Metal Surface*, Physical Review Letters **91**, 080401 (2003).

[Jos65] R. I. Joseph, and E. Schlömann, *Demagnetizing Field in Nonellipsoidal Bodies*, Journal of Applied Physics **36**, 1579 (1965).

[Kap06] M. M. Khapaev, *Extraction of inductances of a multi-superconductor transmission line*, Superconductor Science and Technology **9**, 729 (1996).

[Ket96] W. Ketterle and N. J. van Druten, *Evaporative cooling of atoms*, Advances in Atomic, Molecular, and Optical Physics **37**, 181 (1996).

[Ket99] W. Ketterle, D. S. Durfee, and D. M. Stamper-Kurn, *Making, probing and understanding Bose-Einstein condensates*, Proceedings of the International School of Physics "Enrico Fermi", Course CXL, edited by M. Inguscio, S. Stringari and C.E. Wieman (IOS Press, Amsterdam, 1999) pp. 67-176.

[Ket99] J. B. Ketterson, and S. N. Song, *Superconductivity*, (Cambridge University Press, 1999).

[Kha02] L. Khaykovich, F. Schreck, G. Ferrari, T. Bourdel, J. Cubizolles, L. D. Carr, Y. Castin, and C. Salomon, *Formation of a Matter-Wave Bright Soliton*, Science **296**, 1290 (2002).

[Kin04] J. Kinast, S. L. Hemmer, M. E. Gehm, A. Turlapov, and J. E. Thomas, *Evidence for Superfluidity in a Resonantly Interacting Fermi Gas*, Physical Review Letters **92**, 150402 (2004)

[Kin05] T. Kinoshita, T. Wenger, and D. S. Weiss, *Observation of a one-dimensional Tonks-Girardeau gas*, Science **305**, 1125 (2004).

[Kru03] P. Krüger, X. Luo, M. W. Klein, K. Brugger, A. Haase, S. Wildermuth, S. Groth, I. Bar-Joseph, R. Folman, and J. Schmiedmayer, *Trapping and Manipulating Neutral Atoms with Electrostatic Fields*, Physical Review Letters **91**, 233201 (2003)

[Lau99] D. C. Lau, A. I. Sidorov, G. I. Opat, R. J. McLean, W. J. Rowlands, and P. Hannaford, *Reflection of cold atoms from an array of current-carrying wires*, The European Physical Journal D: Atomic, Molecular, Optical and Plasma Physics **5**, 193 (1999).

[Law95] J. Lawall, S. Kulin, B. Saubamea, N. Bigelow, M. Leduc, and C. Cohen-Tannoudji, *Three-Dimensional Laser Cooling of Helium Beyond the Single-Photon Recoil Limit*, Physical Review Letters **75**, 4194 (1995).

[Lee96] H. J. Lee, C. S. Adams, M. Kasevich, and S. Chu, *Raman Cooling of Atoms in an Optical Dipole Trap*, Physical Review Letters **76**, 2658 (1996).

[Lin04] Y. J. Lin, I. Teper, C. Chin, and V. Vuletic, *Impact of the Casimir-Polder Potential and Johnson Noise on Bose-Einstein Condensate Stability Near Surfaces*, Physical Review Letters **92**, 050404 (2004).

[Lon50] F. London, *Superfluids*, (Wiley, New York, 1950), Vol. I.

[Mat99] M. R. Matthews, B. P. Anderson , P. C. Haljan, D. S. Hall , C. E. Wieman, and E. A. Cornell, *Vortices in a Bose-Einstein Condensate*, Physical Review Letters **83**, 2498 (1999).

[Max65] B. W. Maxfield and W. L. McLean, *Superconducting Penetration Depth of Niobium*, Physical Review **139**, A1515 (1965).

[Mer69] R. Meservey, and P. M. Tedrow, *Measurements of the Kinetic Inductance of Superconducting Linear Structures*, Journal of Applied Physics **40**, 2028 (1969).

[Mew96] M.-O. Mewes, M. R. Andrews, N. J. van Druten, D. M. Kurn, D. S. Durfee, and W. Ketterle, *Bose-Einstein Condensation in a Tightly Confining dc Magnetic Trap*, Physical Review Letters **77**, 416 (1996).

[Muk07] T. Mukai, C. Hufnagel, A. Kasper, T. Meno, A. Tsukada, K. Semba, and F. Shimizu, *Persistent Supercurrent Atom Chip*, Physical Review Letters **98**, 260407 (2007).

[Mul99] D. Müller, D. Z. Anderson, R. J. Grow, P. D. D. Schwindt, and E. A. Cornell, *Guiding Neutral Atoms Around Curves with Lithographically Patterned Current-Carrying Wires*, Physical Review Letters **83**, 5194 (1999).

[Nir06] T. Nirrengarten, A. Qarry, C. Roux, A. Emmert, G. Nogues, M. Brune, J.-M. Raimond, and S. Haroche, *Realization of a Superconducting Atom Chip*, Physical Review Letters **97**, 200405 (2006).

[Obr07] J. M. Obrecht, R. J. Wild, M. Antezza, L. P. Pitaevskii, S. Stringari, and E. A. Cornell, *Measurement of the Temperature Dependence of the Casimir-Polder Force*, Physical Review Letters **98**, 063201 (2007).

[Par03] E. Pardo, A. Sanchez, and C. Navau, *Magnetic properties of arrays of superconducting strips in a perpendicular field*, Physical Review B **67**, 104517 (2003).

[Par04] B. Paredes, A. Widera, V. Murg, O. Mandel, Simon Fölling, I. Cirac, G. V. Shlyapnikov, T. W. Hänsch and I. Bloch, *Tonks-Girardeau gas of ultracold atoms in an optical lattice*, Nature **429**, 277 (2004).

[Rab06] P. Rabl, D. DeMille, J. M. Doyle, M. D. Lukin, R. J. Schoelkopf, and P. Zoller, *Hybrid Quantum Processors: Molecular Ensembles as Quantum Memory for Solid State Circuits*, Physical Review Letters **97**, 033003 (2006).

[Rei99] J. Reichel, W. Hänsel, and T. W. Hänsch, *Atomic Micromanipulation with Magnetic Surface Traps*, Physical Review Letters **83**, 3398 (1999).

[Reg04] C. A. Regal, M. Greiner, and D. S. Jin, *Observation of Resonance Condensation of Fermionic Atom Pairs*, Physical Review Letters **92**, 040403 (2004).

[Rou08] C. Roux, A. Emmert, A. Lupascu, T. Nirrengarten, G. Nogues, M. Brune, J.-M. Raimond and S. Haroche, *Bose-Einstein condensation on a superconducting atom chip*, Europhysics Letters **81**, 56004 (2008).

[Sab99] C. V. Saba, P. A. Barton, M. G. Boshier, I. G. Hughes, P. Rosenbusch, B. E. Sauer, and E. A. Hinds, *Reconstruction of a Cold Atom Cloud by Magnetic Focusing*, Physical Review Letters **82**, 468 (1999).

[Sav97] T. A. Savard, K. M. O'Hara, and J. E. Thomas, *Laser-noise-induced heating in far-off resonance optical traps*, Physical Review A **56**, R1095 (1997).

[Sch05] S. Scheel, P. K. Rekdal, P. L. Knight, and E. A. Hinds, *Atomic spin decoherence near conducting and superconducting films*, Physical Review A **72**, 042901 (2005).

[Shi05] Y. Shin, C. Sanner, G.-B. Jo, T. A. Pasquini, M. Saba, W. Ketterle, and D. E. Pritchard, M. Vengalattore and M. Prentiss, *Interference of Bose-Einstein condensates split with an atom chip*, Physical Review A **72**, 021604(R) (2005).

[Sil06] Christian Silber, *Sympathetisches Kühlen von ^{6}Lithium mit ^{87}Rubidium*, PhD thesis, Eberhard-Karls-Universität Tübingen (2006).

[Ska06] Bo-Sture K. Skagerstam, U. Hohenester, A. Eiguren, and P. K. Rekdal, *Spin Decoherence in Superconducting Atom Chips*, Physical Review Letters **97**, 070401 (2006).

[Sor04] A. S. Sorensen, C. H. van der Wal, L. I. Childress, and M. D. Lukin, *Capacitive Coupling of Atomic Systems to Mesoscopic Conductors*, Physical Review Letters **92**, 063601 (2004).

[Ste] Daniel A. Steck, *Rubidium 87 D Line Data*, available online at http://steck.us/alkalidata (revision 2.1, 1 September 2008).

[Str02] K. E. Strecker, G. B. Partridge, A. G. Truscott, and R. G. Hulet, *Formation and propagation of matter-wave soliton trains*, Nature **417**, 150 (2002).

[Suk97] C. V. Sukumar, and D. M. Brink, *Spin-flip transitions in a magnetic trap*, Physical Review A **56**, 2451 (1997).

[Tin75] M. Tinkham, *Introduction to superconductivity*, (McGraw-Hill, Inc. 1975).

[Tow95] C. G. Townsend, N. H. Edwards, C. J. Cooper, K. P. Zetie, and C. J. Foot, *Phase-space density in the magneto-optical trap*, Physical Review A **52**, 1423 (1995).

[Wan05] Wang, Y.-J., D. Z. Anderson, V. M. Bright, E. A. Cornell, Q. Diot, T. Kishimoto, M. Prentiss, R. A. Saravanan, S. R. Segal, and W. Saijun, *Atom Michelson interferometer on a chip using a Bose-Einstein condensate*, Physical Review Letters **94**, 090405 (2005).

[Wic05] Philipp Wicke, *Optische Methoden zur Erzeugung und zum interferometrischen Nachweis atomarer Quantengase*, Diploma thesis, Eberhard-Karls-Universität Tübingen (2006).

[Wie76] C. Wieman, and T. W. Hänsch, *Doppler-Free Laser Polarization Spectroscopy*, Physical Review Letters **36**, 1170 (1976).

[Wie99] C. E. Wieman, and L. Hollberg, *Using Diode Lasers for Atomic Physics*, Review of Scientific Instruments **62**, 1 (1991).

[Zwi04] M. W. Zwierlein, C. A. Stan, C. H. Schunck, S. M. F. Raupach, A. J. Kerman, and W. Ketterle, *Condensation of Pairs of Fermionic Atoms near a Feshbach Resonance*, Physical Review Letters **92**, 120403 (2004).